NASA TECHNICAL MEMORANDUM

NASA TM X-1683

NASA TM X-1683

FACILITY FORM 602

N68-37941 (ACCESSION NUMBER)	(THRU)
83 (PAGES)	1 (CODE)
(NASA CR OR TMX OR AD NUMBER)	02 (CATEGORY)

GPO PRICE $ ________

CFSTI PRICE(S) $ ________

Hard copy (HC) ____ ____

Microfiche (MF) ____ ____

ff 653 July 65

WIND TUNNEL INVESTIGATION OF AIRFRAME INSTALLATION EFFECTS ON UNDERWING ENGINE NACELLES AT MACH NUMBERS FROM 0.56 TO 1.46

by Bernard J. Blaha and Daniel C. Mikkelson

Lewis Research Center
Cleveland, Ohio

NATIONAL AERONAUTICS AND SPACE ADMINISTRATION • WASHINGTON, D. C. • NOVEMBER 1968

NASA TM X-1683

WIND TUNNEL INVESTIGATION OF AIRFRAME INSTALLATION EFFECTS ON UNDERWING ENGINE NACELLES AT MACH NUMBERS FROM 0.56 TO 1.46

By Bernard J. Blaha and Daniel C. Mikkelson

Lewis Research Center
Cleveland, Ohio

NATIONAL AERONAUTICS AND SPACE ADMINISTRATION

For sale by the Clearinghouse for Federal Scientific and Technical Information
Springfield, Virginia 22151 – CFSTI price $3.00

ABSTRACT

A 1/20 scale model of the F-106B with simulated underwing engine nacelles was tested in the Lewis Research Center 8- by 6-foot supersonic wind tunnel. Pressures and boattail drag coefficients were obtained on cone-cylinder and bulged nacelles with 15° conical boattail afterbodies and jet boundary simulators. Data were obtained with and without inlet airflow through the nacelles at attack angles from 0° to 8°. Effects of nacelle strut geometry, local elevon geometry, and elevon deflection were also investigated. The installed boattail pressure drag coefficient was lower than isolated nacelle values at all Mach numbers, and transonic drag rise was delayed to Mach 0.975.

WIND TUNNEL INVESTIGATION OF AIRFRAME INSTALLATION EFFECTS ON UNDERWING ENGINE NACELLES AT MACH NUMBERS FROM 0.56 TO 1.46

by Bernard J. Blaha and Daniel C. Mikkelson

Lewis Research Center

SUMMARY

A test was conducted in the Lewis Research Center 8- by 6-foot supersonic wind tunnel utilizing a 1/20 scale model of the F-106B aircraft with simulated underwing engine nacelles. Pressures and boattail drag coefficients were obtained on cone-cylinder nacelles and on bulged nacelles, both with 15° conical boattail afterbodies and jet boundary simulators. Data were obtained with and without inlet airflow through the nacelles at angles of attack from 0° to 8°.

Airframe installation resulted in reduced pressure on the cylindrical portion of the nacelle aft of the forebody cone shoulder and increased pressure on the boattail when compared with isolated nacelle results. The resulting boattail drag coefficients were reduced at all Mach numbers, and the transonic drag rise was delayed until Mach 0.975. Closed nacelle inlets generally resulted in decreased boattail drag coefficients. Increased angle of attack resulted in increased pressure forward on the nacelle but had little effect on boattail pressure drag. The effects of nacelle strut geometry, local elevon geometry, and elevon deflection on boattail drag coefficient were generally small.

INTRODUCTION

As part of a broad program in airbreathing propulsion, the Lewis Research Center is investigating airframe installation effects on exhaust nozzle performance of nozzle systems appropriate for use at supersonic speeds. In this continuing program, airframe installation effects are being investigated both in wind tunnel and flight tests at subsonic and transonic speeds.

It has been demonstrated that performance of an exhaust system can be appreciably affected, especially at off-design conditions, when it is installed on an aircraft (refs. 1 to 4). This result generally arises from perturbations generated by the aircraft on the nozzle external flow field. With an engine nacelle installation typical for a supersonic cruise aircraft, the nacelle may be installed close to the lower surface of a large wing and the afterbody may extend downstream of the wing trailing edge. This aft location of the nacelle provides shielding of the inlet by the wing surfaces to minimize angle-of-attack effects. To investigate installation effects on the flow over a podded engine installation of this type, a test was conducted in the Lewis 8- by 6-foot supersonic wind tunnel utilizing a 1/20 scale model of the F-106B aircraft with simulated underwing engine nacelles. The F-106B model was selected because it has a wing planform which could be representative of present and future supersonic aircraft. In addition, the Lewis Research Center will use an F-106B aircraft in a flight test program to investigate installation effects on a variety of propulsion system concepts incorporated in underwing engine nacelles.

In the wind tunnel tests, nacelle pressures and boattail drag coefficients were obtained on cone-cylinder and bulged nacelles with 15° conical boattail afterbodies and jet boundary simulators. These afterbodies simulated the geometry of a variable flap ejector when the exit area is closed for operation at subsonic and transonic speeds. Data were obtained both with and without inlet airflow through the nacelles over a Mach number range of 0.56 to 1.46 at angles of attack from 0° to 8°. The influence of nacelle strut geometry, local elevon geometry, and elevon angle was investigated. Results of these investigations are presented herein, and comparisons are made with data from isolated-nacelle studies. Also, the results of a simulation of the effects of an adjacent outboard nacelle on an inboard nacelle achieved by using a reflection plate are presented.

SYMBOLS

A	cross-sectional area of cylindrical nacelle, 1.205 in.^2 (7.78 cm^2)
A_{β}	projected area of boattail, 0.664 in.^2 (4.28 cm^2)
BL	body line station measured from model centerline
b	wing span, 23.292 in. (59.1 cm)
$C_{D,\beta}$	axial boattail pressure drag coefficient in direction of nacelle ℄, (axial force)/q_0A
C_p	pressure coefficient, $(p - p_0)/q_0$
d	diameter of cylindrical nacelle, 1.239 in. (3.145 cm)
l	axial distance along wing chord line at body line station at 3.635 in. (9.26 cm)
M_0	free-stream Mach number

P_0	free-stream stagnation pressure
p	local static pressure
p_0	free-stream static pressure
q_0	free-stream dynamic pressure
r	radius of cylindrical nacelle, 0.620 in. (1.572 cm)
x	axial distance aft of nacelle cone shoulder
y	coordinate defining lower surface of wing near nacelle along body line station at 3.635 in. (9.26 cm)
z	coordinate defining width of narrow nacelle strut
α	model angle of attack, deg
δ	elevon deflection angle, +down and -up, deg
φ	nacelle angular coordinate, deg

APPARATUS AND PROCEDURE

Figure 1 is a schematic drawing of the model installation in the transonic test section of the Lewis 8- by 6-foot supersonic wind tunnel. The model, a 1/20 scale of the F-106B aircraft, was sting mounted from the tunnel floor strut. Shown in figure 2 are two views of the model installed in the tunnel with two different underwing engine nacelle configurations. Tests were conducted over a range of Mach numbers from 0.56 to 1.46 at angles of attack from 0° to 8°. Reynolds number varied from 3.6×10^{6} per foot (1.18×10^{5} per cm) at Mach number 0.56 to 4.96×10^{6} per foot (1.628×10^{5} per cm) at Mach number 1.46. Model blockage at 0° angle of attack was less than 0.3 percent. Although the model scale was relatively small, it was selected to avoid effects of tunnel wall interference at transonic Mach numbers.

A schematic drawing of the model details and the installation of the simulated engine nacelles is shown in figure 3. The aircraft model was 38.475 inches (97.60 cm) long and had a 60° sweptback delta wing with an 11.646-inch (29.57-cm) semispan. The F-106B fuselage inlets were open and thus allowed airflow to pass through the model fuselage. The simulated engine nacelles were strut mounted to the lower surface of the wing on each side of the fuselage at body line stations (BL) of 3.635 inches (9.26 cm) or 32.05 percent semispan. Hereinafter, the nacelles are called left and right, as viewed in the upstream direction. The nacelles were installed at a -4.5° incidence angle with respect to the wing chord and extended aft of the wing trailing edge. The nacelles also extended below the lower surface of the fuselage which was fairly flat in the region of the nacelles. However, because of area rule considerations, the fuselage sidewalls, which extended below the wing, had a slight contour in the vicinity of the nacelles (fig. 3(a)). Each nacelle had a 15° conical boattail with zero radius of curvature at its juncture with the cylindrical portion of the nacelle and was followed by a cylindrical jet boundary simulator. The purpose of the simulator was to approximate the local flow field that would exist in the presence of a jet with an exit- to local-static-pressure ratio of 1.0. The elevons could be tested in three positions, with deflection angles of 0°, $+5^{\circ}$ (downward), and -5° (upward). Fixed sections of the elevons were used above the nacelles, hereinafter called elevon cutouts.

Figure 4 is a schematic diagram of the two nacelle geometries investigated, a cone-cylinder configuration and a similar configuration with a bulged section added to the lower surface to simulate an engine accessory pod. The latter configuration was a scaled version of the nacelle to be used in a series of flight tests to be conducted at Lewis utilizing a J-85/13 engine. Both nacelle geometries had a cylindrical diameter of 1.239 inches (3.145 cm). To investigate the effects of nacelle inlet spillage, each nacelle configuration was tested with open and closed inlets. The open nacelles had normal shock inlets which allowed the stream flow to pass through the nacelle body and exit at the aft end of the jet boundary simulators. The inlet capture area was selected to approximate the engine airflow demand of a supersonic turbojet engine operated at subsonic and transonic speeds. The solid nacelles had 6.1° half-angle conic forebodies, and the open nacelles had 6.1° cowls. The length of all the nacelle configurations, as measured along the upper surface from the forebody shoulder to the end of the boattail afterbody, was 6.611 inches (16.78 cm). The afterbodies had a ratio of projected boattail area to cross-sectional area of the nacelle based on the cylindrical diameter (A_{β}/A) of 0.551. The base of each boattail was located 0.92 nacelle diameter aft of the wing trailing edge.

All the model instrumentation was located on the nacelles, as shown in figure 5. The solid nacelles (fig. 5(a)) were instrumented over their entire length with a total of 63 pressure orifices (64 for the bulged nacelles) located at six angular coordinate stations ϕ. Each boattail had a total of 16 pressure orifices located at four angular coordinate stations and at four longitudinal stations at the centroid of equal annular areas. Thus, an equal projected area was assigned to each orifice. These orifices were then used to obtain the integrated boattail axial pressure drag coefficient defined as follows:

$$C_{D,\beta} = \frac{-A_{\beta}}{A} \overline{C}_p$$

where $\overline{C}_p$ is the average boattail pressure coefficient. The instrumentation for the solid nacelles was brought out through the end of the jet boundary simulators (fig. 2(b)). The open nacelles (fig. 5(b)) were instrumented near the aft end only. Eight pressure orifices were located on the cylindrical portion of the open nacelles at four angular coordinate stations. The boattails had a total of 12 orifices located at only three angular coordinate stations ($\varphi = 0^{\circ}$, 180°, and 270°). The integrated boattail pressure drag was then obtained by combining the orifices on the three angular coordinate stations from the nacelle under one wing with the orifices on the $\varphi = 270^{\circ}$ angular coordinate station from the nacelle under the other wing. The bulged nacelles had one orifice located internally near the end of the boattail at $x/d = 5.3$. The open-nacelle instrumentation was brought out of the nacelles through the struts and through channels cut into the model wing.

Two types of struts were investigated and are shown in figure 6. The first type is referred to as the narrow strut and was used in conjunction with the rectangular elevon cutout (fig. 7(a)). The second type is referred to as the wide strut and was used in conjunction with the faired elevon cutout (fig. 7(b)). The wide strut was designed to fair into the base of this cutout. The faired elevon cutout was used to simulate a typical auxiliary inlet ejector nozzle installation and is shown installed on the model in figure 8. In such an installation, some of the auxiliary inlets would be exposed to the top wing flow field and the remainder to the underwing flow field. Because of the limitations of the model design, open auxiliary inlets were not used.

A reflection-plate simulation of an adjacent nacelle was made for an outboard nacelle located at BL 7.175 inches (18.21 cm) or 61.6 percent semispan. The reflection plate was located midway between the inboard and outboard nacelle locations at BL 5.405 inches (13.72 cm) or 46.4 percent semispan. Details of the reflection plate and installation of the reflection plate and outboard nacelle are shown in figure 9. First, a test was conducted to determine the influence of the reflection plate on the inboard nacelle. Then, another test was conducted to determine the influence of an identical outboard nacelle.

Boundary layer trips, as seen in figures 2 and 8, were used to ensure that transition would occur forward on the model and nacelles. A 0.25-inch-wide (0.634-cm-wide) strip of number-30 grit was attached 2 inches (5.08 cm) aft of the model and nacelle leading edges.

RESULTS AND DISCUSSION

Boattail Pressure Drag

Comparisons of the installed-nacelle boattail pressure coefficient distributions with data from a larger isolated nacelle tested in the same facility at Mach 0.9 are shown in figure 10. These results indicate a large installation effect that increased boattail pressures, but because of the limited instrumentation on the installed nacelle (16 orifices as compared with 70 on the larger model), the low pressure which occurred just aft of the boattail shoulder was not properly accounted for in the boattail pressure integration. A similar conclusion was also evident at other Mach numbers. Because of the significant change in the pressure distributions when these low pressures were included, it was decided to correct the installed-nacelle boattail drag data in an approximate manner, using the results from the isolated-nacelle tests. The isolated nacelle was a 4.0-inch-diameter (10.16-cm-diam) solid cone-cylinder configuration with a 10° half-angle forebody cone. It had the same boattail geometry as the installed nacelles. The isolated nacelle was tested with three lengths of cylindrical section (4.72, 6.53, and 11.53 model diameters) with the shortest having the same cylindrical-section length to diameter ratio as the installed nacelles. The appearance of these models was generally similar to that of the nacelles described in reference 5. Results from these isolated-nacelle tests indicated that the low pressure just aft of the boattail shoulder (0.012 model diameter) is a function of the local Mach number or local static to free-stream stagnation pressure ratio immediately upstream of the shoulder (fig. 11). Therefore, with the assumption of no alteration of the initial expansion by installation effects, a reasonable estimate of the minimum boattail pressure coefficient on the installed nacelles was obtained by first examining the local upstream pressure ratio p/P_0 (assuming no stagnation pressure loss). This was done for each angular coordinate station to account for circumferential variations in the flow around the installed nacelles. The pressure coefficients obtained in this manner were averaged around the nacelle and then compared with the average pressure coefficient measured at the first boattail orifice station (11) on the installed nacelles. The difference in average pressure coefficient between these two stations was then used to calculate an incremental drag coefficient. This was done, as demonstrated in figure 12, by assuming that the average pressure coefficient determined using figure 11 existed at the centroid of the projected annular area, $A_{\beta}/A = 0.04$. The incremental drag coefficient was then algebraically added to the original drag coefficient based on 16 orifices. In figures 10 to 20 the installed boattail drag coefficients have been corrected as described.

A comparison between boattail drag coefficients obtained with the installed nacelles and data from the isolated-nacelle model is shown in figure 13. At all Mach numbers, installed boattail drag coefficients measured on the cylindrical and bulged nacelles (both open and solid) are lower than isolated-nacelle results. The boattail drag coefficients are low at subsonic Mach numbers and do not increase with increasing Mach number until Mach numbers greater than 0.975 are achieved. These reductions in boattail drag coefficient at subsonic Mach numbers are similar in trend to the results observed in reference 6 where a 15° conical boattail was tested under a simulated wing (dashed curve, fig. 13). In figure 13 installed-nacelle data are presented for both the left and right nacelles and generally show favorable agreement. The drag coefficients measured on the right nacelle near Mach 1.0 are slightly lower than those on the left nacelle. This effect is attributable to a slight radius of curvature that was inadvertently generated on the boattail shoulder of the right nacelle when the instrumentation was installed.

The effect of nacelle inlet spillage, as determined from a comparison between solid and open nacelles (fig. 13), indicates that increased inlet spillage generally results in decreased boattail drag coefficient except for the bulged nacelles between Mach numbers 1.0 and 1.1 and the cylindrical nacelles at Mach 1.0. Also seen in figure 13 are differences in boattail drag coefficient between the cylindrical and bulged nacelles that vary with inlet spillage. With the open nacelles, the bulge resulted in lower drag coefficients except between Mach numbers 0.95 and 1.1. With the solid nacelles, the differences between the cylindrical and bulged nacelles are decreased at subsonic Mach numbers and increased between Mach numbers 0.95 and 1.1. This effect indicates that increased inlet spillage can both moderate and enhance the influence of the bulges on boattail drag coefficient.

The effect of angle of attack is shown in figure 14 for the configuration with cylindrical solid nacelles and rectangular elevon cutouts at 0° elevon angle. Over the Mach number range investigated, the effect of increasing angle of attack was small except subsonically at 8° angle of attack, where the boattail drag increased, and supersonically between Mach numbers 1.0 and 1.1, where boattail drag decreased with increasing angle of attack. Similar results were obtained for all other configurations.

In figures 15 and 16, the effect of elevon angle on boattail drag coefficient is shown for the two different elevon cutout geometries. In general, elevon angle slightly influences boattail drag coefficient, but a consistent trend is not apparent except near Mach 1.0 where both plus and minus 5° elevon angles result in increased boattail drag. The effect of nacelle strut and elevon cutout geometry on boattail drag coefficient is shown in figure 17 for the solid and open bulged nacelles at 0° angle of attack and 0° elevon angle. At subsonic Mach numbers, the effects of strut and elevon cutout geometry are small; however, at supersonic Mach numbers, the faired elevon cutout configuration resulted in a 2 to 7.5 percent increase in boattail drag coefficient as compared with values obtained with the rectangular elevon cutout configuration. Therefore, it is evident that the wing flow directed into the boattail region by the faired elevon cutouts can result in small increases in drag coefficient. However, it should be noted that this result might differ if open auxiliary inlets were present.

To evaluate the effects of F-106B fuselage inlet spillage on boattail drag coefficient, tests were conducted with the F-106B inlets internally blocked. These tests were conducted for both the rectangular and faired elevon cutout geometries. The results, as shown in figure 18, indicate that the drag coefficients were generally slightly higher with the F-106B inlets plugged, with the highest drag coefficients being observed for the faired-elevon-cutout configuration.

In figure 19 are presented the results of a test which was conducted to simulate the influence of an adjacent outboard nacelle on an inboard nacelle by the utilization of a reflection plate located midway between the nacelle stations. As seen in figure 19, at all Mach numbers the influence of the reflection plate on the inboard-nacelle boattail drag coefficient is negligible; however, the influence of the adjacent outboard nacelle is significant between Mach numbers 0.95 to 1.05 and 1.36 to 1.46. These results indicate that an adjacent nacelle can influence boattail drag coefficient and that these effects cannot be adequately simulated by a simple reflection plate.

To investigate the influence of the jet boundary simulators on boattail drag coefficient, a test was conducted with the jet boundary simulators removed from the open-bulged-nacelle configuration. The results of this test, as shown in figure 20, indicate that boattail drag coefficient is significantly increased at all Mach numbers without the jet boundary simulators, which agrees with results presented in reference 5.

Nacelle and Boattail Pressures

In figure 21, pressure distributions are presented for the cylindrical nacelles at 0° model angle of attack and 0° elevon angle for all Mach numbers investigated. Pressure coefficient data are presented for only the left nacelle since a favorable agreement was observed between the left and right nacelle pressures. This agreement was true for all the configurations investigated. The pressures on the forward portion of the nacelle demonstrate a similarity to those obtained on typical isolated cone-cylinder configurations. A typical flow overexpansion occurs at the cone-cylinder juncture and the flow recompresses downstream on the cylindrical portion of the nacelle. At subsonic Mach numbers, the flow over the boattail shows an expansion region at the boattail juncture followed by a recompression, with the aft boattail pressures being recompressed to levels greater than free-stream static. At Mach numbers 0.90 and 0.95, a pressure discontinuity region, or terminal shock, moves aft on the nacelle with increasing Mach number, which tends to increase the pressures over the aft portion of the nacelle. These high pressures on the boattail account for the low drag coefficients observed at subsonic Mach numbers in figure 13. Above Mach 0.95, the pressure discontinuity region moves aft of the boattail, and the decreasing pressure on the boattail results in the drag rise observed at Mach 0.975 (fig. 13). At supersonic Mach numbers, the flow expansion at the boattail juncture is stronger, and the pressure over the entire boattail remains less than free-stream static. Circumferential pressure variations exist over the entire nacelle length. On the forward portion of the nacelle, higher pressures occur on the bottom of the nacelle, and, on the aft portion, pressures are generally higher at the top.

In figure 22, pressure distributions for the cylindrical nacelle at a model angle of attack of 4° are compared with data from the isolated model at 0° angle of attack. Different angles of attack are used in this comparison to provide a similar alinement of the two nacelles with free-stream flow. On the cylindrical section of the installed nacelle, pressures are generally lower than isolated results; an opposite trend is seen on the boattail. The lower pressures on the installed-nacelle body probably result from a reflection of the cone-shoulder flow expansion from the lower surface of the wing, which amplifies the overexpansion of the nacelle pressures. Recompression to free-stream static pressure requires greater length along the nacelle, and at the high subsonic speeds the boattail is immersed in this recompression field. The higher boattail pressures on the installed nacelle at high subsonic speeds are strongly dependent on the location of the terminal shock within the recompression region. These pressure comparisons correspond to the boattail drag coefficient comparisons shown in figure 13 and demonstrate why the transonic drag rise was delayed until Mach 0.975.

The static pressure measured aft in the flow duct of the open nacelle is seen in figure 23. At supersonic Mach numbers the pressure in the duct is less than free-stream static both with and without jet boundary simulators which indicates that the open nacelle inlet was probably capturing a complete stream tube and that the resulting spillage was probably due only to the cowl projected area. This is in contrast to the complete spillage of the solid-nacelle configurations.

The effect of inlet spillage as determined from a comparison between open- and solid-nacelle pressures is shown in figure 24. Since the open nacelles were instrumented only over the aft portion, a comparison can be made in this region only. The data shown for the $\varphi = 90^{\circ}$ coordinate on the open-nacelle boattail were obtained from the identical nacelle under the right wing. The pressures immediately upstream of the boattail for most Mach numbers are lower for the solid nacelles except on top of the open nacelle at $x/d = 4.55$. In general, the pressures on the boattail were slightly higher for the solid nacelles except at Mach 1.0. These boattail pressure comparisons are again reflected in the boattail drag coefficient results shown in figure 13.

Pressure distributions on the bulged nacelles are shown in figure 25 at 0° angle of attack for two representative Mach numbers. As would be expected, the pressures over the bulged region of the nacelle differ from those observed for the cylindrical nacelle in figure 21. Pressures over the aft region of the nacelle and on the boattail were similar to the cylindrical-nacelle results. Circumferential pressure variations can again be seen over the entire length of the nacelle.

The effects of model angle of attack on the solid-bulged-nacelle pressure distributions are shown in figure 26 for two representative Mach numbers. In general, increasing angle of attack resulted in higher pressures over the forward portion of the nacelles; however, over the aft portion of the nacelle and on the boattail, the changes were small. The small influence of angle of attack on boattail pressures is reflected in the boattail drag results shown in figure 14.

The effect of elevon angle on nacelle pressure distribution is presented in figure 27 for the solid bulged nacelles at 0° angle of attack. In general, elevon angle significantly influenced the pressure on the aft end of the nacelles but had only a small influence on the boattail pressures. With the elevons deflected $+5^{\circ}$ (down), the pressures on the aft end of the nacelles increased; with the elevons at -5° (up), the same pressures decreased.

In figures 28 and 29, the combined effect of nacelle strut and elevon cutout geometry on nacelle pressure distribution is shown for the solid and open nacelles, respectively, at 0° angle of attack. The data presented for the open-nacelle boattails at $\varphi = 90^{\circ}$ were again obtained from the nacelle under the right wing. In general, a change in nacelle strut and elevon cutout geometry has little influence on the pressures over the forward portion of the nacelles. However, with wide struts and the faired elevon cutouts, the pressures over the aft portion of the nacelles are greater than those measured with the narrow struts and rectangular elevon cutouts at both subsonic and supersonic Mach numbers. This result is seen primarily on the upper region of the nacelle at angular coordinates $\varphi = 0^{\circ}$, 45°, and 315°. The low pressures on the upper quadrant of the boattail show that the faired elevon cutouts result in a stronger flow expansion at the boattail juncture. This stronger flow expansion corresponds to the slight increase in boattail drag coefficient measured with the faired cutouts, as shown in figure 17.

Figure 30 shows the effect of F-106B fuselage inlet spillage on nacelle pressure distributions at 0° angle of attack and 0° elevon angle. At both subsonic and supersonic Mach numbers, blocking the F-106B inlets resulted in small changes in the nacelle pressures. The pressures on the boattail are generally lower with the F-106B inlets closed, which results in the slight increase in boattail drag coefficient shown in figure 18.

The influence of a reflection plate and an adjacent outboard nacelle on the inboard nacelle pressure distribution is shown in figure 31 at 0° angle of attack for two representative Mach numbers. At subsonic Mach numbers, the influence of both the reflection plate and the outboard nacelle was negligible. This result was also generally true for the reflection plate at supersonic Mach numbers. However, the adjacent outboard nacelle resulted in significant changes in the inboard nacelle pressures. This result indicates that the reflection plate located midway between the two nacelle locations does not adequately simulate an outboard nacelle over the Mach number range tested.

A comparison of nacelle pressures with and without jet boundary simulators is shown in figure 32 for the open bulged nacelles at 0° angle of attack and 0° elevon angle. The effects of removing the jet boundary simulators are predominantly evident on the boattail where the pressures are decreased. This result corresponds to the increased boattail drag coefficients seen in figure 20 with the jet boundary simulators removed.

SUMMARY OF RESULTS

To investigate airframe installation effects on engine nacelles and afterbodies at subsonic and supersonic speeds, a test was conducted in the Lewis Research Center 8- by 6-foot supersonic wind tunnel using a 1/20 scale model of the F-106B aircraft with simulated underwing engine nacelles. Pressure data and boattail drag coefficients were obtained on cone-cylinder nacelles and on bulged nacelles, both with 15° conical boattail afterbodies and jet boundary simulators. Data were obtained both with and without airflow through the nacelles over a Mach number range of 0.56 to 1.46 at angles of attack from 0° to 8°. The following results were obtained:

1. Airframe installation resulted in reduced pressure on the nacelle body aft of the forebody cone shoulder and increased pressure on the boattail when compared with isolated-nacelle results. The corresponding boattail drag coefficients were reduced at all Mach numbers and the transonic drag rise was delayed to Mach 0.975.

2. Closed nacelle inlets generally decreased boattail drag coefficient except near Mach 1.0.

3. Increasing the angle of attack increased pressures over the forward portion of the nacelles and had little effect on the boattail pressures. The corresponding effect on boattail drag coefficient was small except subsonically at 8° angle of attack, where the drag increased, and near Mach 1.0, where increasing angle of attack resulted in reduced boattail drag.

4. At subsonic Mach numbers, combined strut and elevon cutout geometry and elevon angle had little effect on boattail drag coefficient. At supersonic Mach numbers, the wide struts and faired elevon cutouts resulted in 2 to 7.5 percent increases in boattail drag coefficient as compared with values observed with rectangular elevon cutouts. Nacelle pressures were influenced by the variations in geometry at all Mach numbers.

5. A reflection plate was not effective in simulating the effects of an adjacent outboard nacelle on boattail pressures. The effects of the outboard nacelle were significant at Mach numbers from 0.95 to 1.05 and 1.36 to 1.46.

Lewis Research Center,
National Aeronautics and Space Administration,
Cleveland, Ohio, July 3, 1968,
126-15-02-10-22.

REFERENCES

1. Corson, Blake W., Jr.; and Schmeer, James W.: Summary of Research on Jet-Exit Installations. NASA TM X-1273, 1966.

2. Runckel, Jack F.: Jet-Exit and Airframe Interference Studies on Twin-Engine-Fuselage Aircraft Installations. NASA TM X-1274, 1966.

3. Runckel, Jack F.; Lee, Edwin E., Jr.; and Simonson, Albert J.: Sting and Jet Interference Effects on the Afterbody Drag of a Twin-Engine Variable-Sweep Fighter Model at Transonic Speeds. NASA TM X-755, 1963.

4. Nichols, Mark R.: Aerodynamics of Airframe-Engine Integration of Supersonic Aircraft. NASA TN D-3390, 1966.

5. Shrewsbury, George D.: Effect of Boattail Juncture Shape on Pressure Drag Coefficients of Isolated Afterbodies. NASA TM X-1517, 1968.

6. Shrewsbury, George D.: Effect of Simulated Wing on the Pressure-Drag Coefficients of Various 15° Boattails at Mach Numbers From 0.56 to 1.00. NASA TM X-1662, 1968.

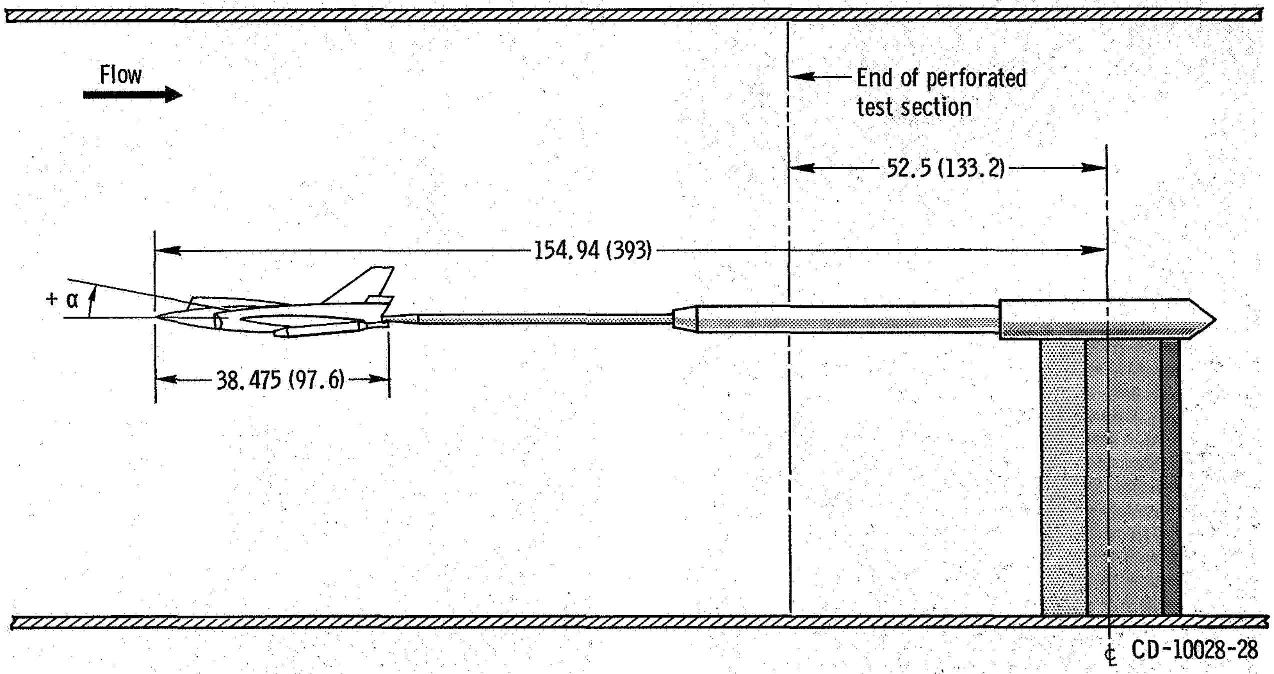

Figure 1. - Schematic drawing of model installation in transonic test section of 8- by 6-foot supersonic wind tunnel. (Dimensions are in inches (cm).)

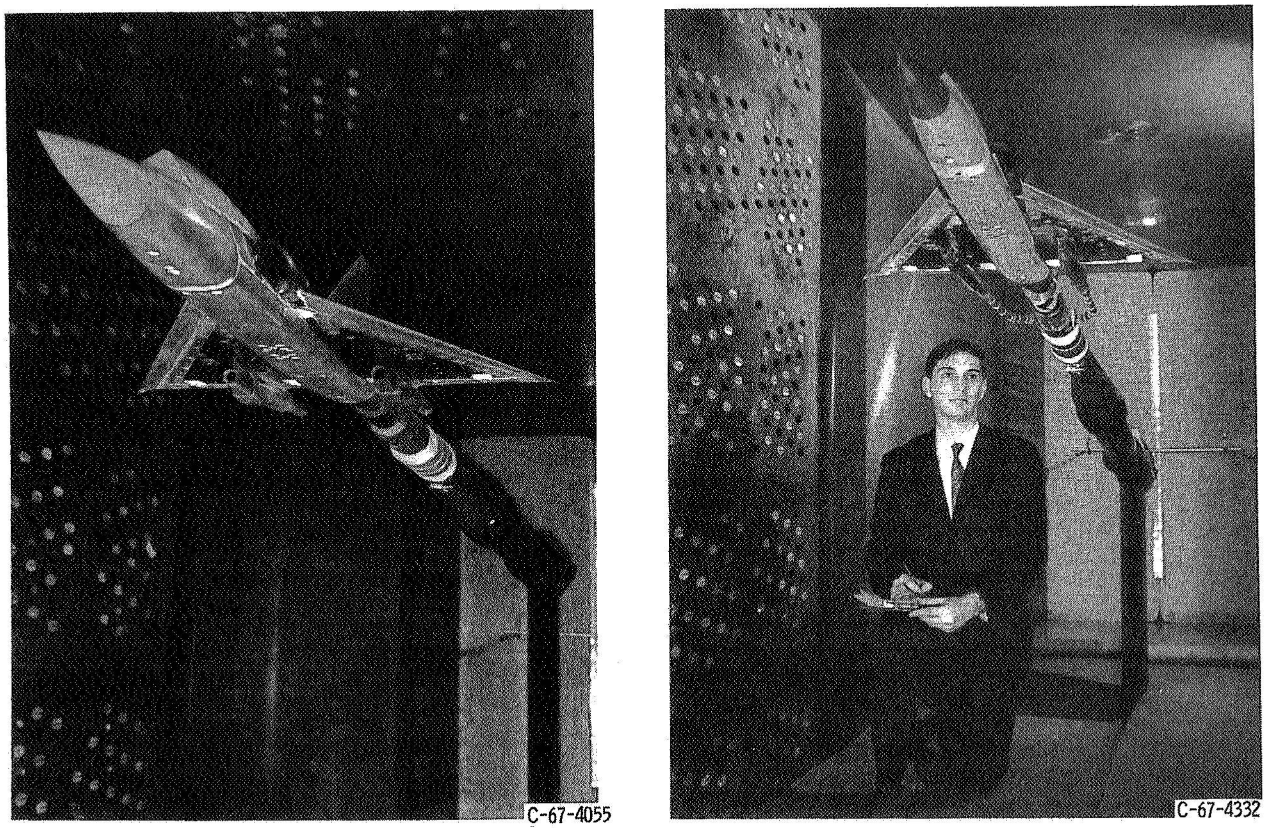

(a) Open-nacelle configuration. (b) Solid-nacelle configuration.

Figure 2. - Model installed in wind tunnel.

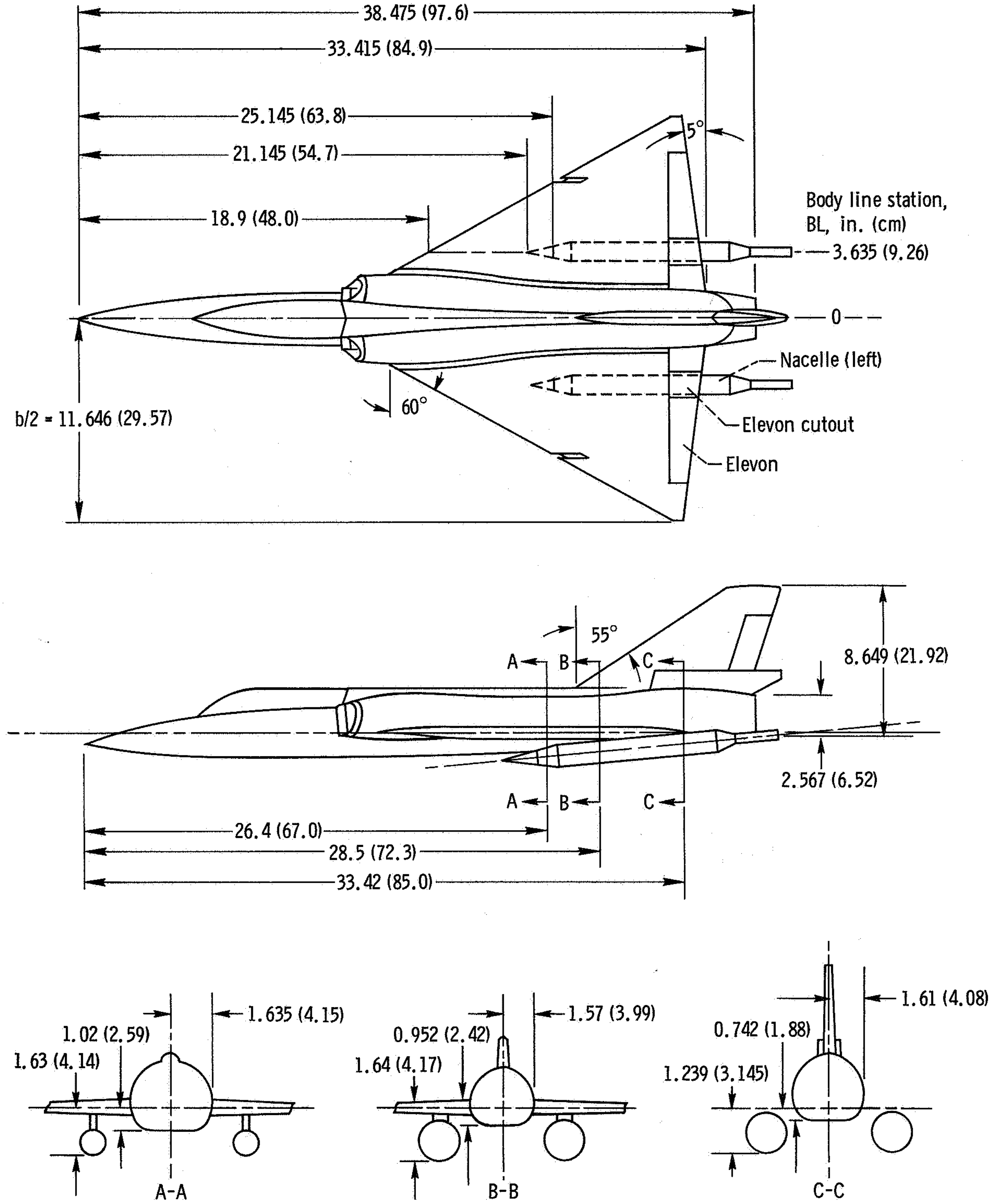

(a) Model details.

CD-10029-28

Figure 3. - Schematic drawing of model details and installation of nacelle under model wing. (Dimensions are in inches (cm).)

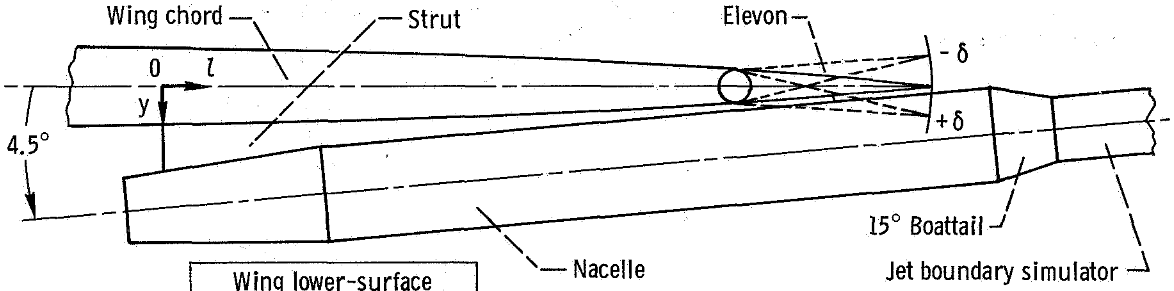

Wing lower-surface coordinates			
l		y	
in.	cm	in.	cm
0	0	0.279	0.708
1.898	4.81	.278	.706
3.72	9.46	.237	.602
5.54	14.08	.133	.338
6.458	16.4	.068	.154

(b) Nacelle installation.

CD-10029-28

Figure 3. - Concluded.

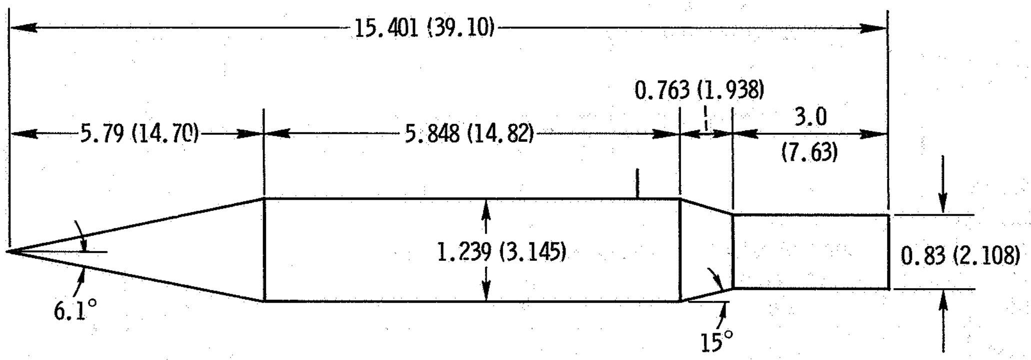

(a) Solid cylindrical nacelle.

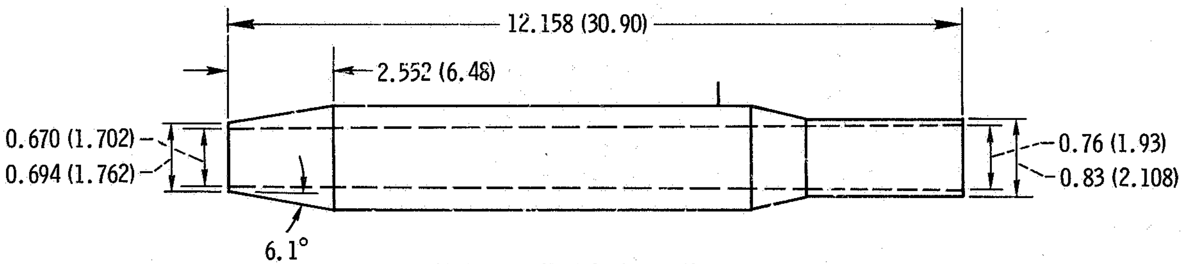

(b) Open cylindrical nacelle.

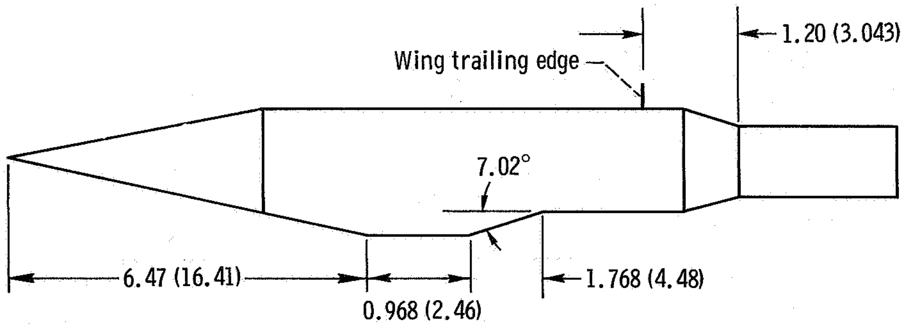

(c) Solid bulged nacelle.

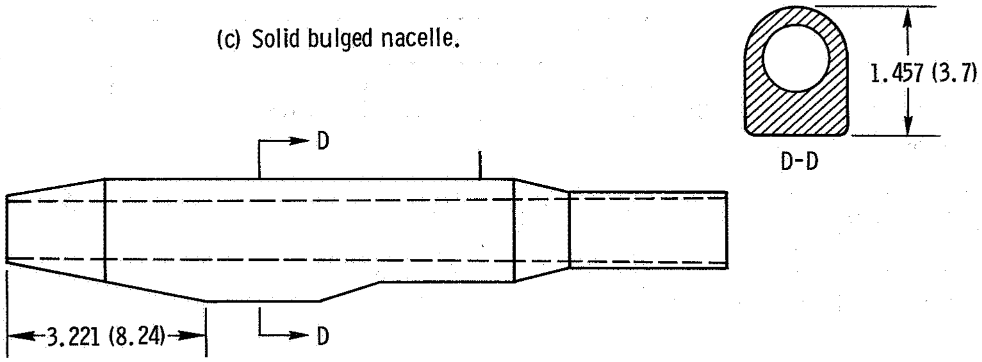

(d) Open bulged nacelle.

CD-10030-28

Figure 4. - Types of nacelles investigated. (Dimensions are in inches (cm).)

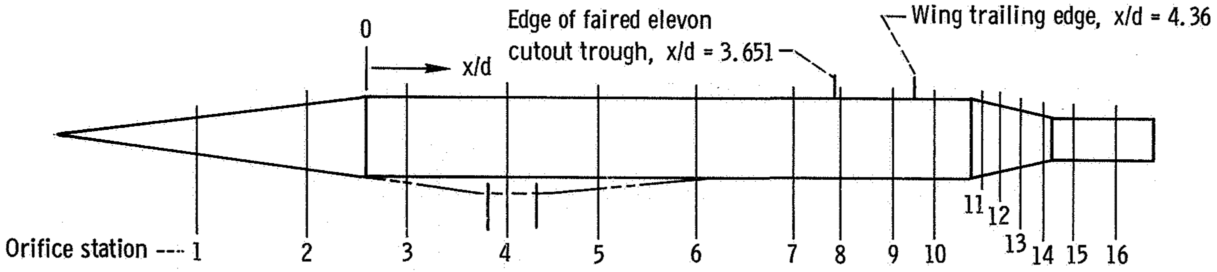

Orifice location on nacelle	Orifice station	Nondimensional position coordinate, x/d	Nacelle angular coordinate, φ, deg
Conic forebody	1	-1.416	90, 180, 270
	2	-.598	90, 180, 270
Nacelle body	3	0.218	90, 180, 270
	[a]4	[a].921	90, 180, 270
	5	1.623	90, 180, 270
	6	2.344	45, 90, 180, 270, 315
	7	3.071	45, 90, 180, 270, 315
	8	3.704	0, 45, 90, 180, 270, 315
	9	4.121	0, 45, 90, 180, 270, 315
	10	4.540	0, 45, 90, 180, 270, 315
15° Boattail	11	4.786	0, 90, 180, 270
	12	4.923	↓
	13	5.076	
	14	5.244	
Jet boundary simulator	15	5.537	0, 180
	16	5.941	0, 180

[a] For φ = 180° on bulged nacelles, orifice at station 4 (x/d = 0.921) is replaced by orifices at x/d = 0.790 and 1.12.

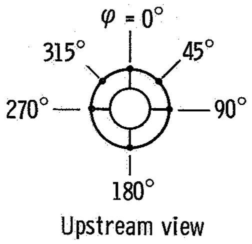

(a) Solid-nacelle configurations.

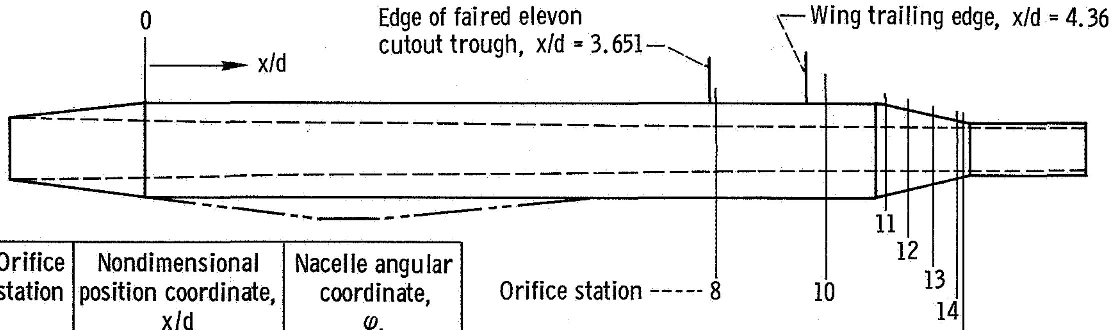

Orifice location on nacelle	Orifice station	Nondimensional position coordinate, x/d	Nacelle angular coordinate, φ, deg
Nacelle body	8	3.704	0, 90, 180, 270
	10	4.540	0, 90, 180, 270
15° Boattail	11	4.786	0, 180, 270
	12	4.923	↓
	13	5.076	
	14	5.244	
Internal[a]	15	5.30	270

[a] Installed on bulged nacelles only.

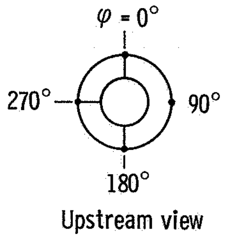

CD-10031-28

(b) Open-nacelle configurations.

Figure 5. - Nacelle pressure instrumentation.

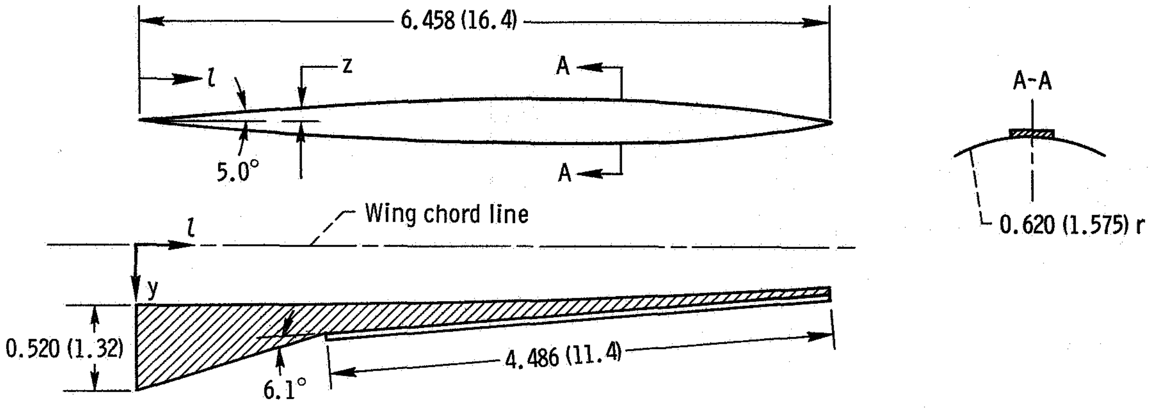

l		z		l		y	
in.	cm	in.	cm	in.	cm	in.	cm
0	0	0	0	0	0	0.279	0.708
.938	2.38	.072	.183	1.898	4.81	.278	.706
1.987	5.04	.137	.348	3.72	9.46	.237	.602
2.580	6.55	.149	.378	5.54	14.08	.133	.338
4.639	11.76	.149	.378	6.458	16.4	.068	.154
5.714	14.5	.112	.284				
6.458	0	0	0				

(a) Narrow nacelle strut fairing.

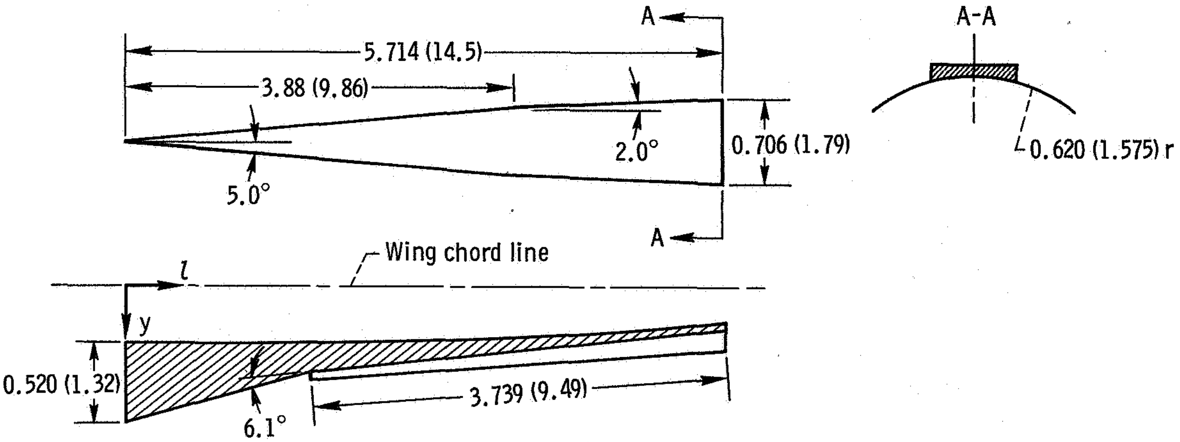

CD-10032-28

(b) Wide nacelle strut fairing.

Figure 6. - Schematic drawing of nacelle strut fairings. (Dimensions are in inches (cm).)

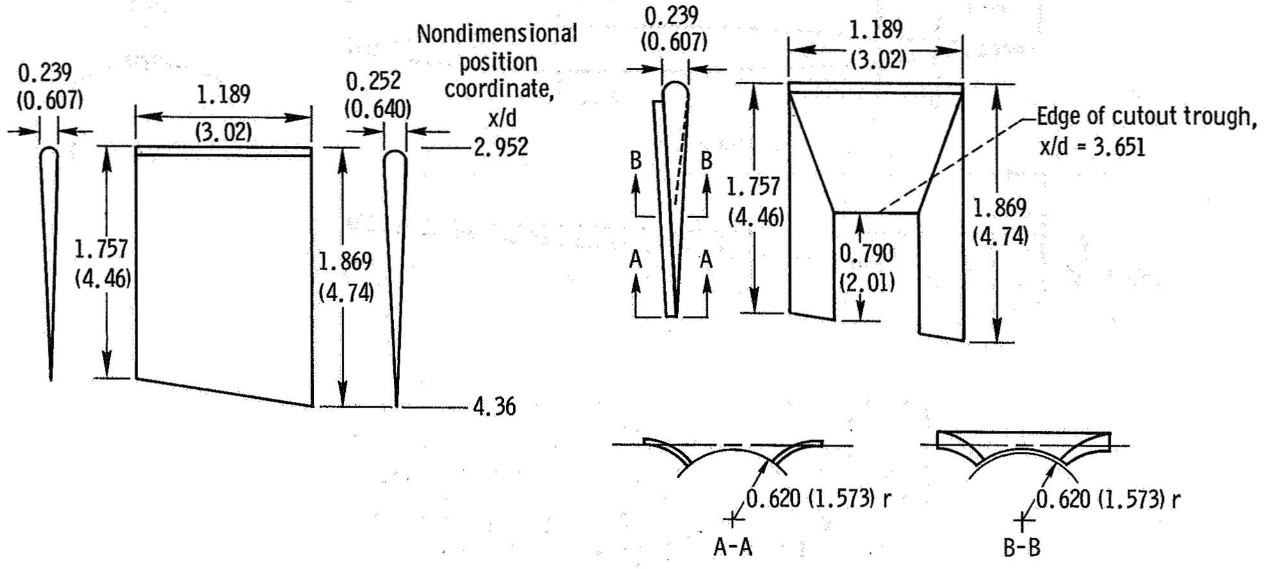

(a) Rectangular elevon cutout.

(b) Faired elevon cutout.

CD-10033-28

Figure 7. - Schematic drawing of fixed elevon cutouts. (Dimensions are in inches (cm).)

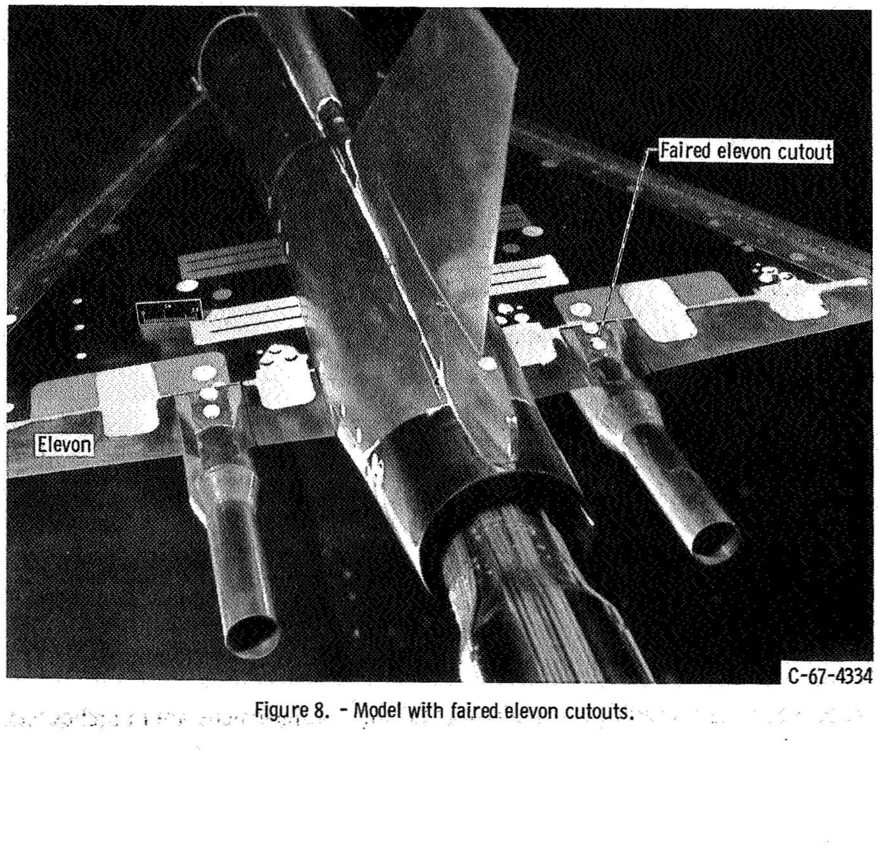

Figure 8. - Model with faired elevon cutouts.

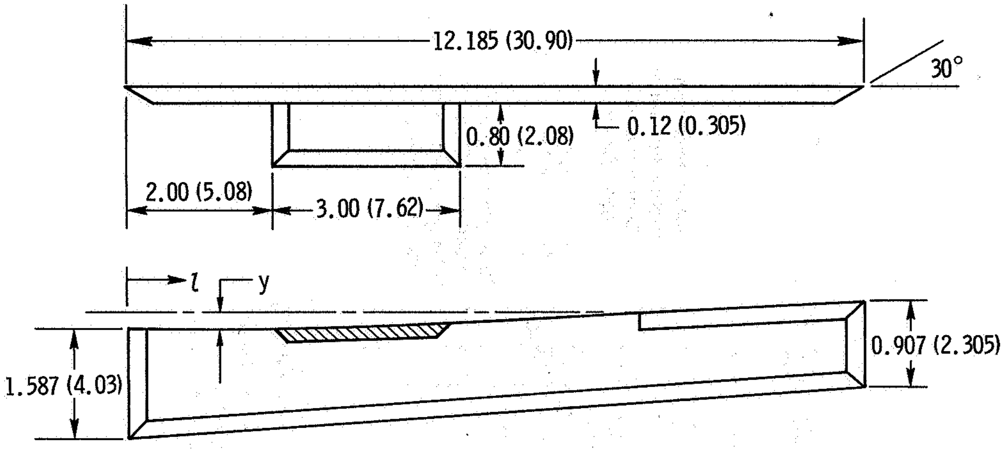

l		y	
in.	cm	in.	cm
0	0	0.279	0.708
2.434	6.18	.278	.706
4.26	10.8	.237	.602
6.07	15.4	.133	.338
7.788	19.75	0	0

(a) Reflection plate.

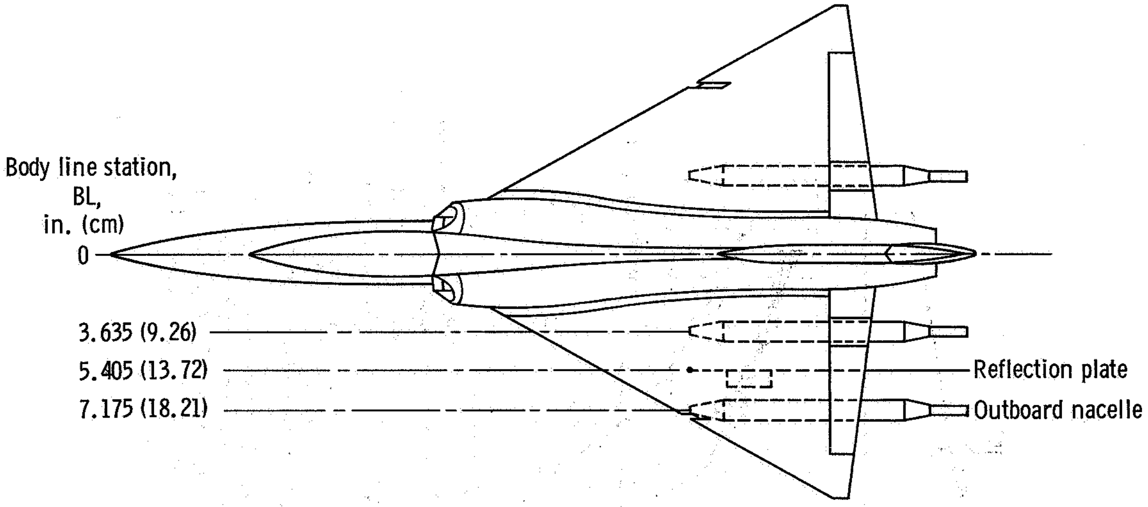

(b) Installation of reflection plate and outboard nacelle, planform view.

CD-10034-28

Figure 9. - Schematic drawing of reflection plate and installation of reflection plate and outboard nacelle on model. (Dimensions are in inches (cm).)

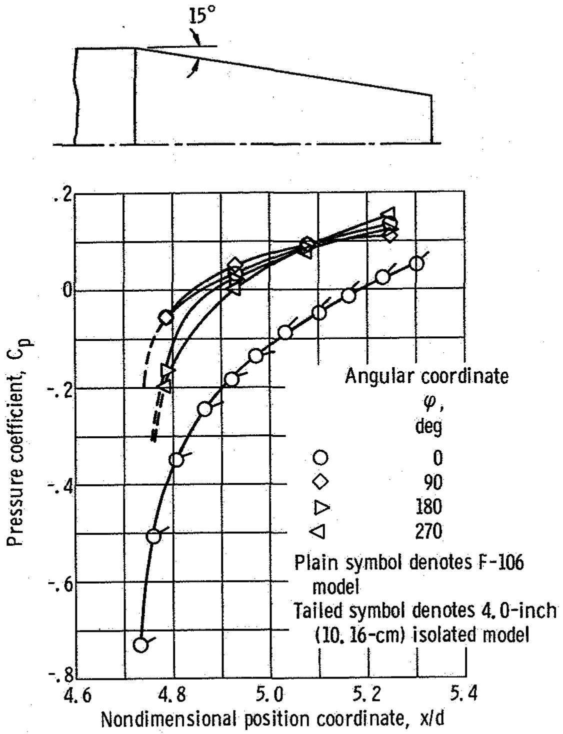

Figure 10. - Comparison of installed-nacelle boattail pressure distributions with data from 4-inch-diameter (10.16-cm-diam) isolated model; Mach 0.9 and 0° angle of attack.

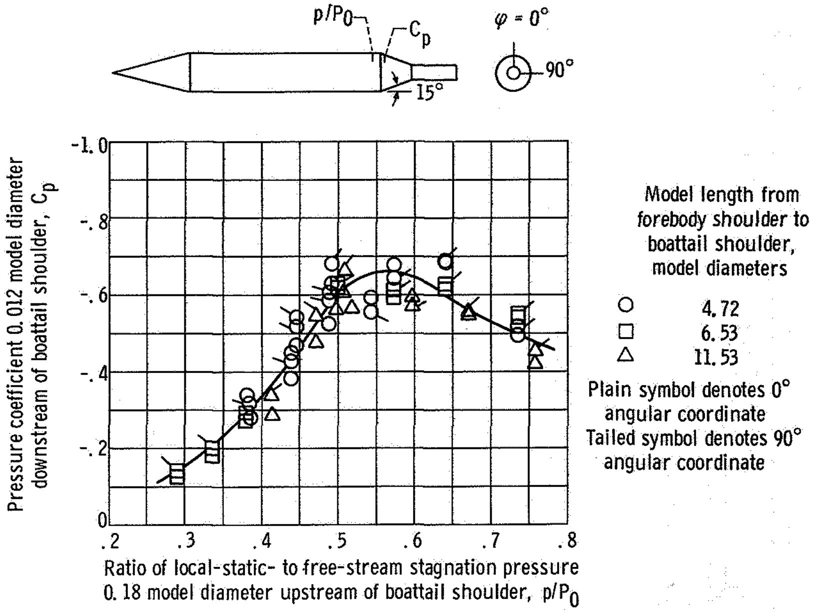

Figure 11. - Pressure coefficient 0.012 model diameter downstream of boattail shoulder from 4.0-inch-diameter (10.16-cm-diam) isolated model at 0° angle of attack.

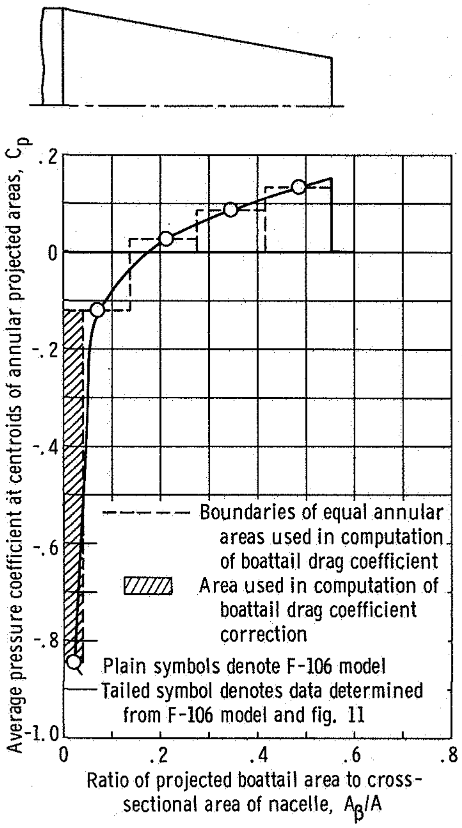

Figure 12. - Average boattail static-pressure distribution at Mach 0.9 and 0° angle of attack, demonstrating method used to obtain corrected boattail drag coefficient.

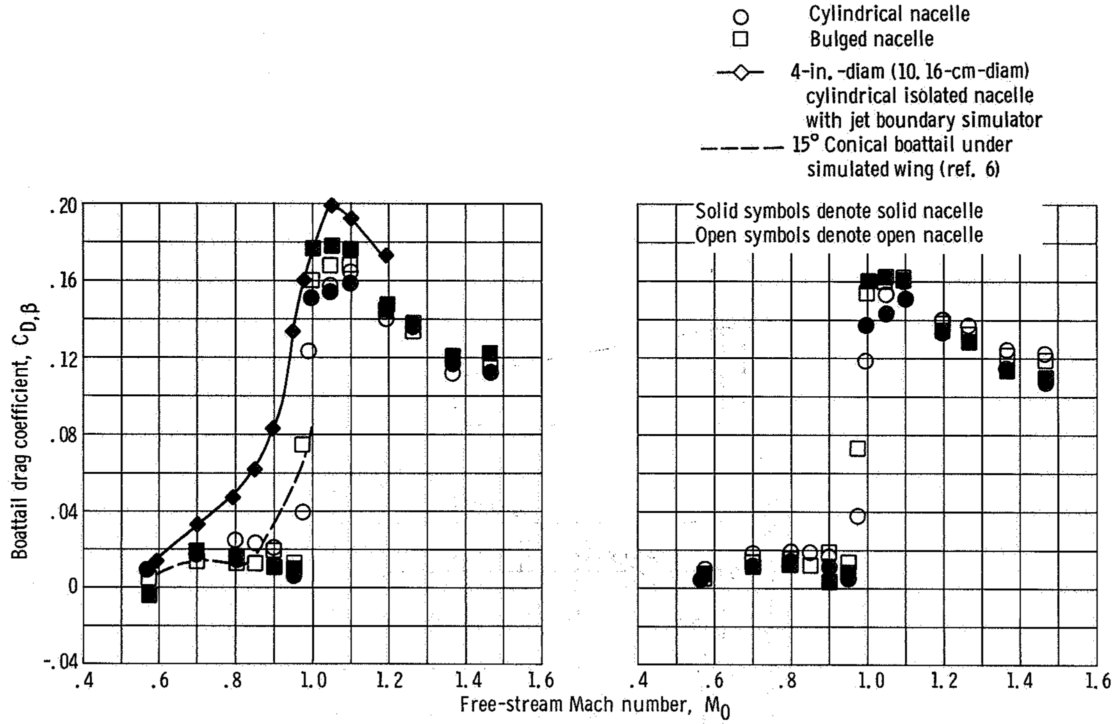

(a) Left nacelle.

(b) Right nacelle.

Figure 13. - Boattail drag coefficient for solid- and open-nose nacelles; narrow strut fairings and rectangular elevon cutouts at 0° angle of attack and 0° elevon angle.

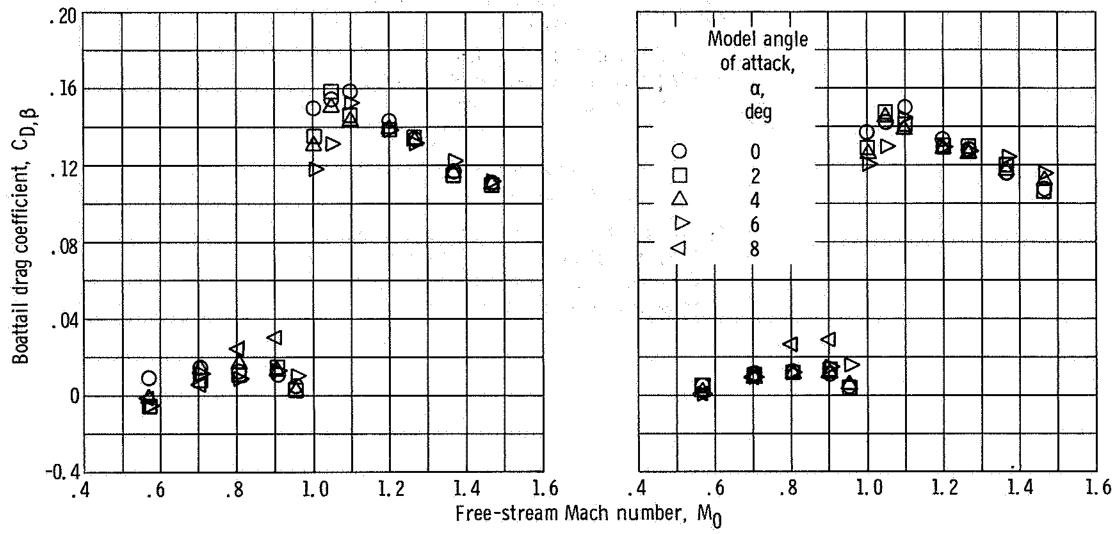

(a) Left nacelle.

(b) Right nacelle.

Figure 14. - Effect of angle of attack on boattail drag coefficient; cylindrical solid nacelles with narrow struts, rectangular elevon cutouts, and elevons at 0°.

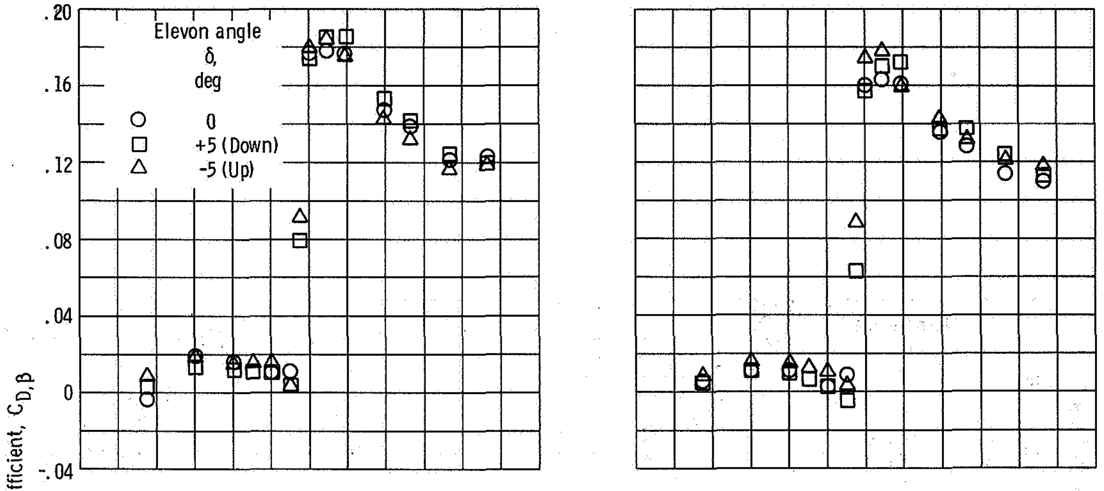

(a-1) Left nacelle.

(a-2) Right nacelle.

(a) Solid nacelles.

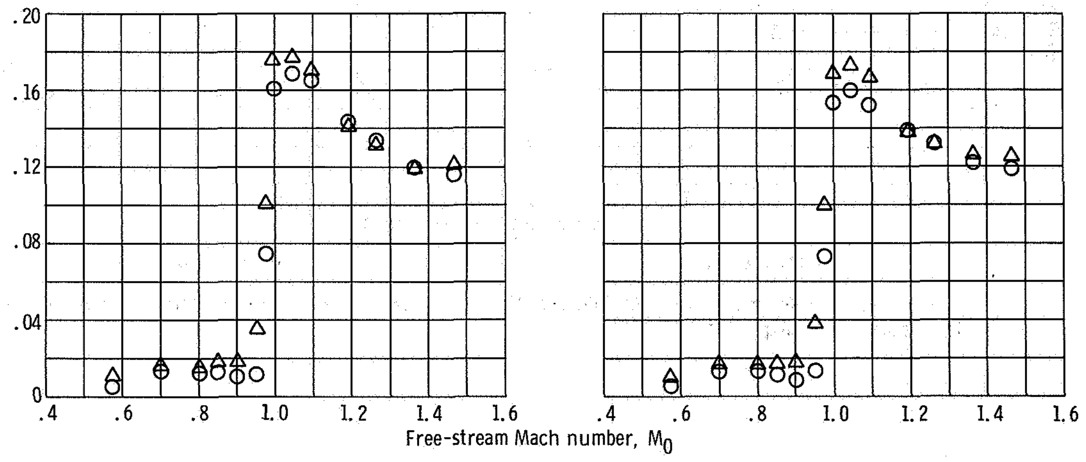

(b-1) Left nacelle.

(b-2) Right nacelle.

(b) Open nacelles.

Figure 15. - Effect of elevon angle on boattail drag coefficient; bulged nacelles with narrow struts and rectangular elevon cutouts at 0° angle of attack.

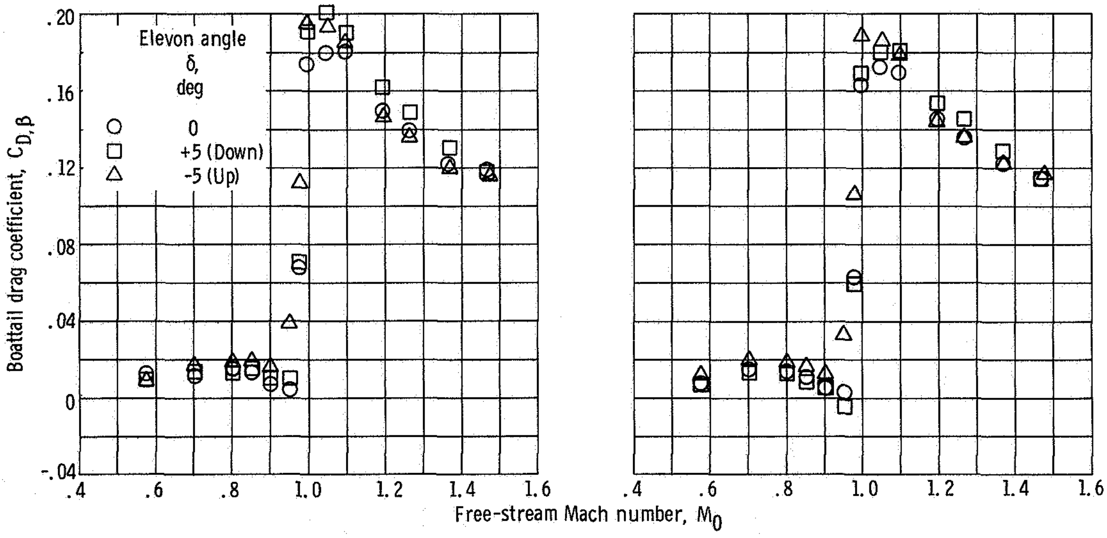

(a) Left nacelle.

(b) Right nacelle.

Figure 16. - Effect of elevon angle on boattail drag coefficient; solid bulged nacelles with wide nacelle struts and faired elevon cutouts at 0° angle of attack.

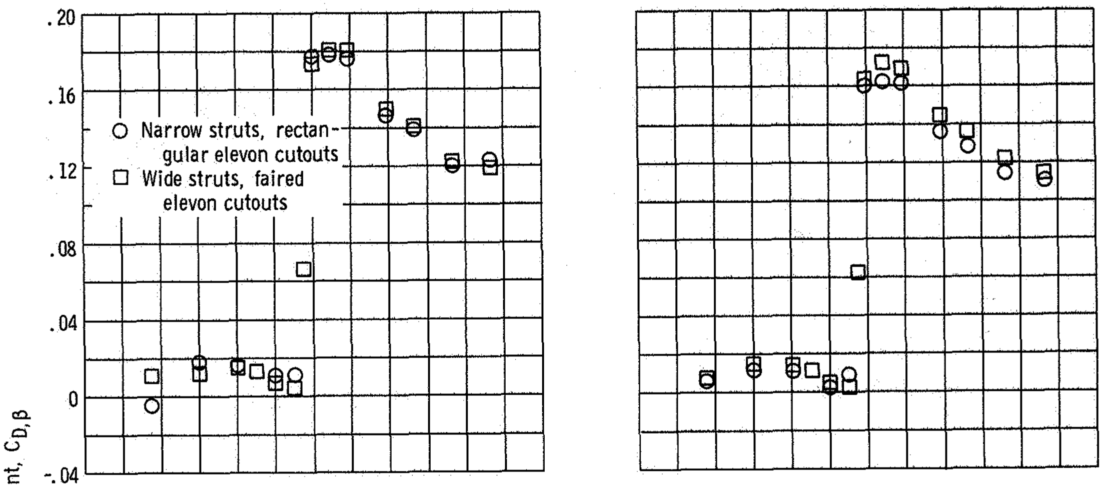

(a-1) Left nacelle.

(b-1) Right nacelle.

(a) Solid nacelles.

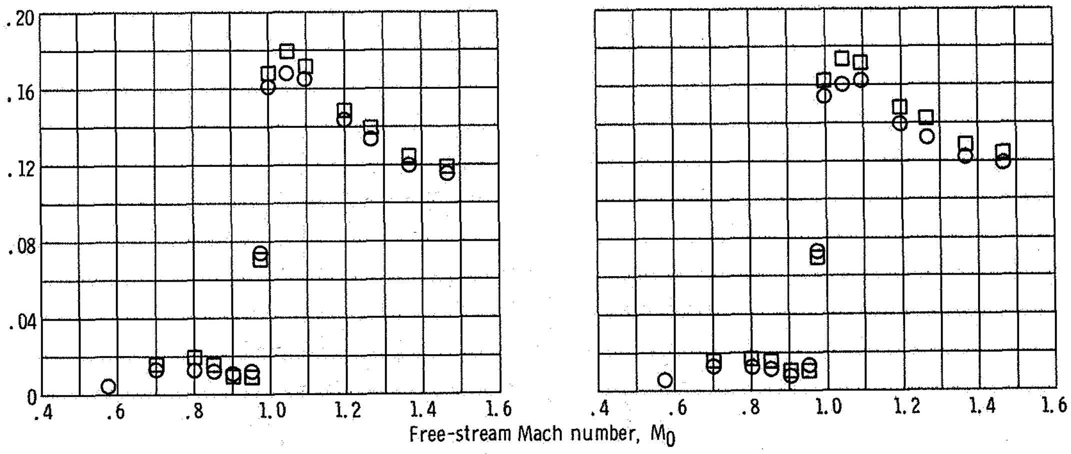

(b-1) Left nacelle.

(b-2) Right nacelle.

(b) Open nacelles.

Figure 17. - Effect of nacelle strut and elevon cutout geometry on boattail drag coefficient; bulged nacelles at 0° angle of attack and 0° elevon angle.

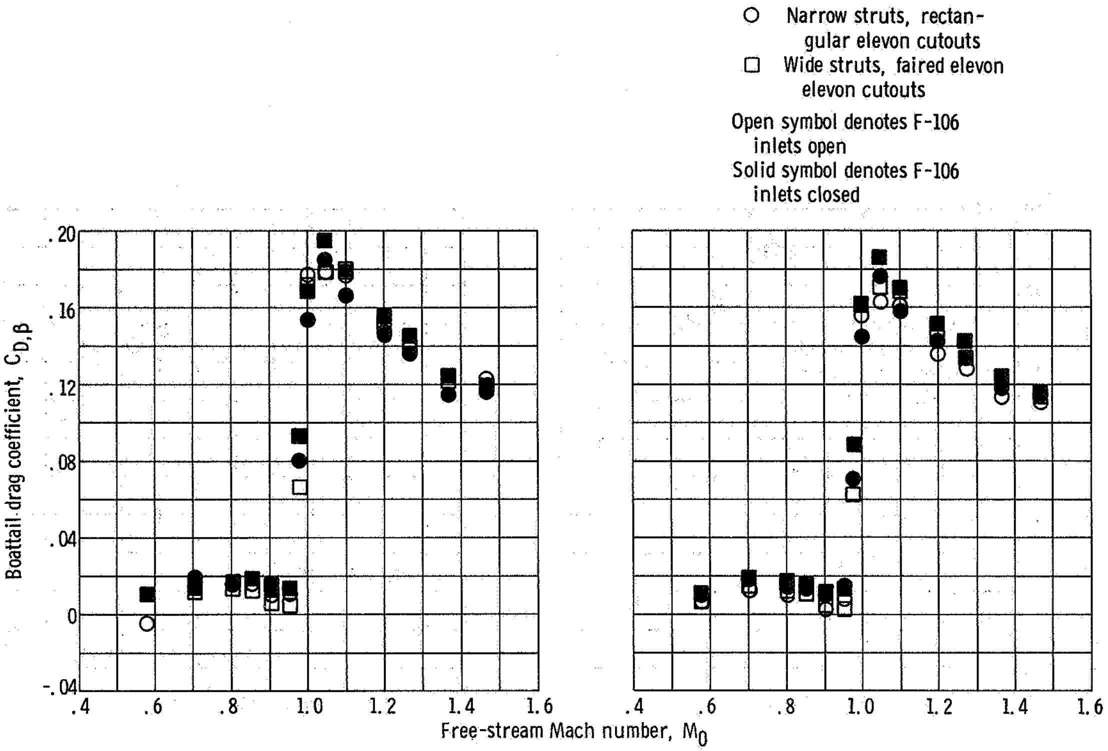

(a) Left nacelle.

(b) Right nacelle.

Figure 18. - Effect of closed F-106 inlets on boattail drag coefficient; solid bulged nacelles at 0° angle of attack and 0° elevon angle.

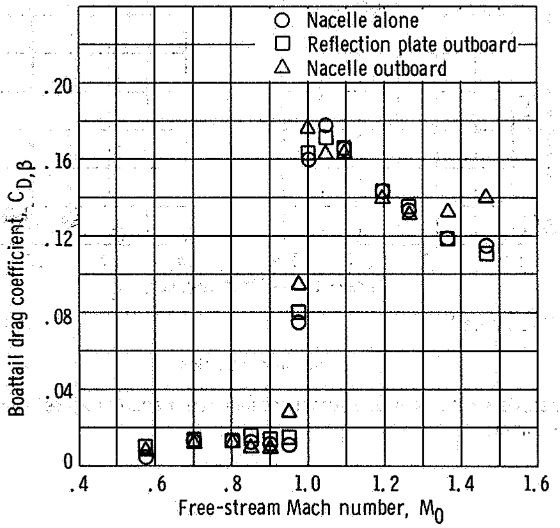

Figure 19. - Effect of reflection plate and outboard nacelle on left-inboard-nacelle boattail drag coefficient; open bulged nacelles, narrow struts, and rectangular elevon cutouts at 0° angle of attack and 0° elevon angle.

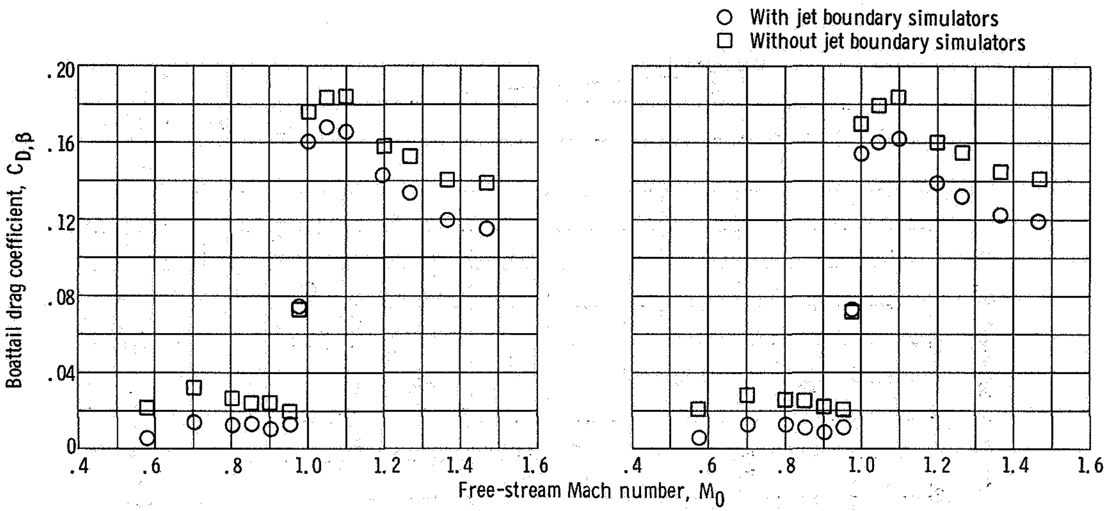

(a) Left nacelle.

(b) Right nacelle.

Figure 20. - Effect of jet boundary simulators on boattail drag coefficient; open bulged nacelles, narrow struts, and rectangular elevon cutouts at 0° angle of attack and 0° elevon angle.

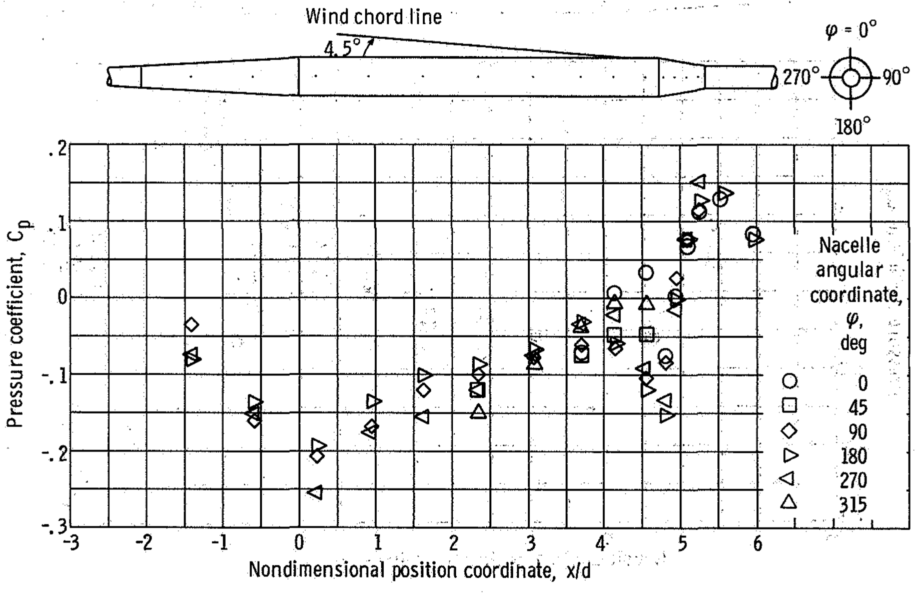

(a) Free-stream Mach number, 0.56.

Figure 21. - Pressure distribution on left cylindrical solid nacelle; narrow struts and rectangular elevon cutouts at 0° angle of attack and 0° elevon angle.

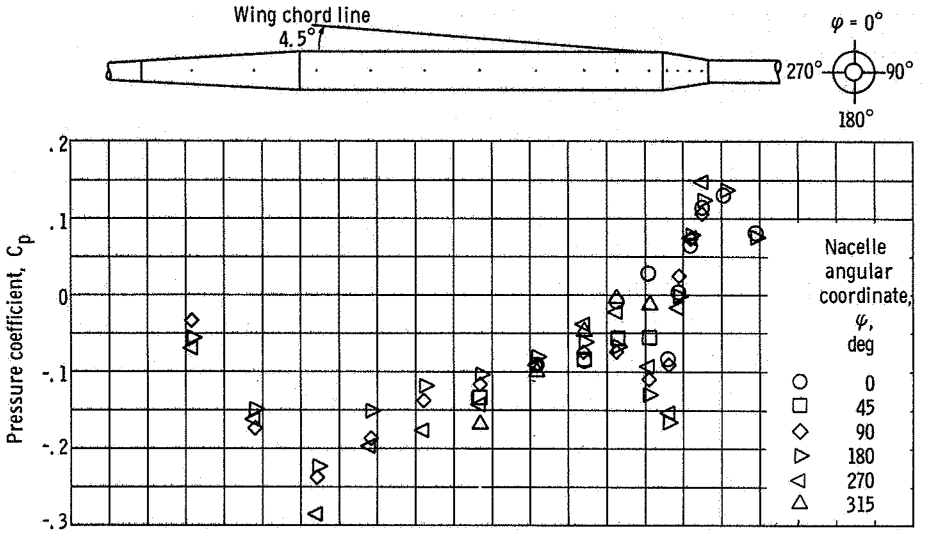

(b) Free-stream Mach number, 0.7.

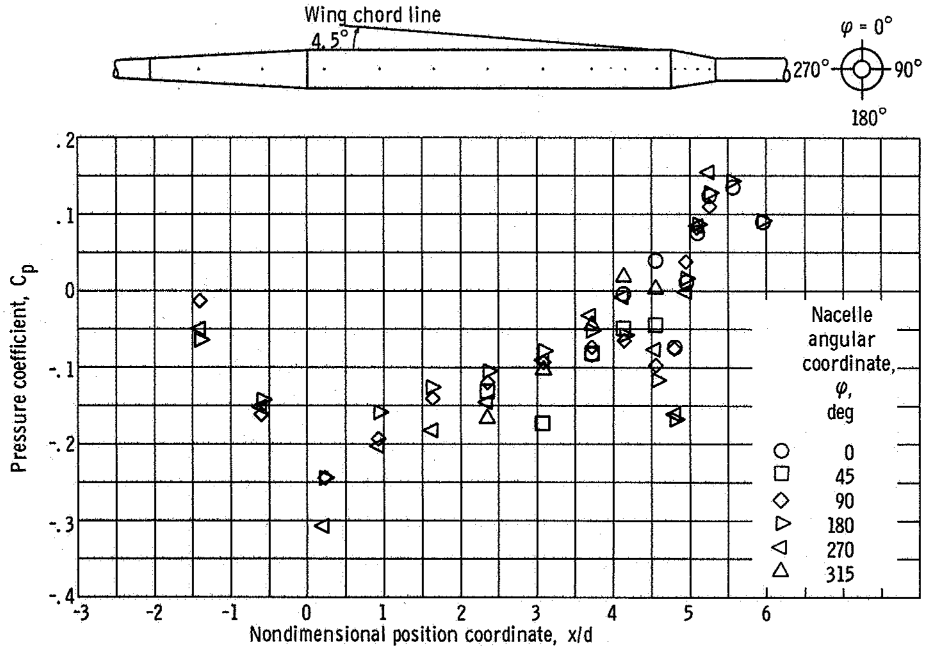

(c) Free-stream Mach number, 0.8.

Figure 21. - Continued.

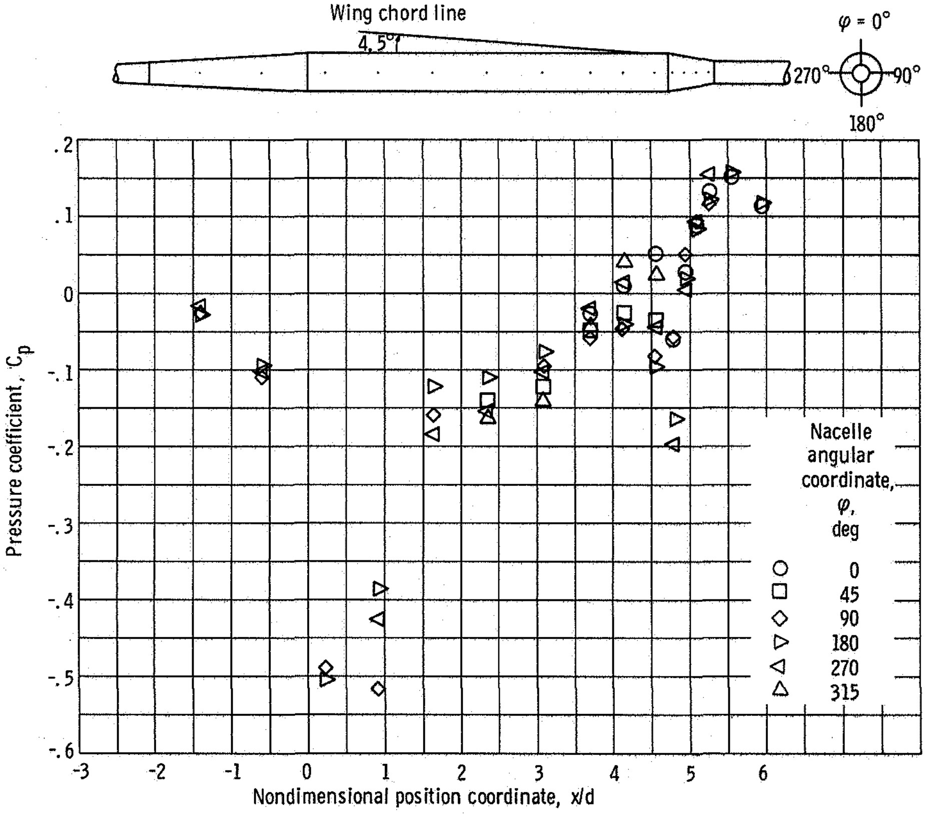

(d) Free-stream Mach number, 0.9.

Figure 21. - Continued.

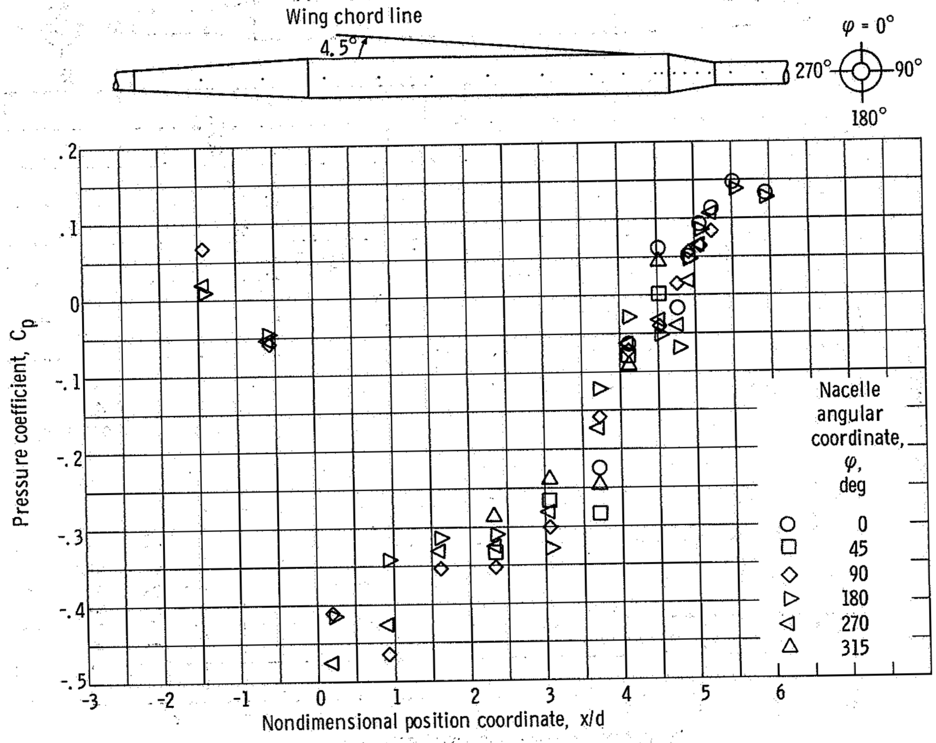

(e) Free-stream Mach number, 0.95.

Figure 21. - Continued.

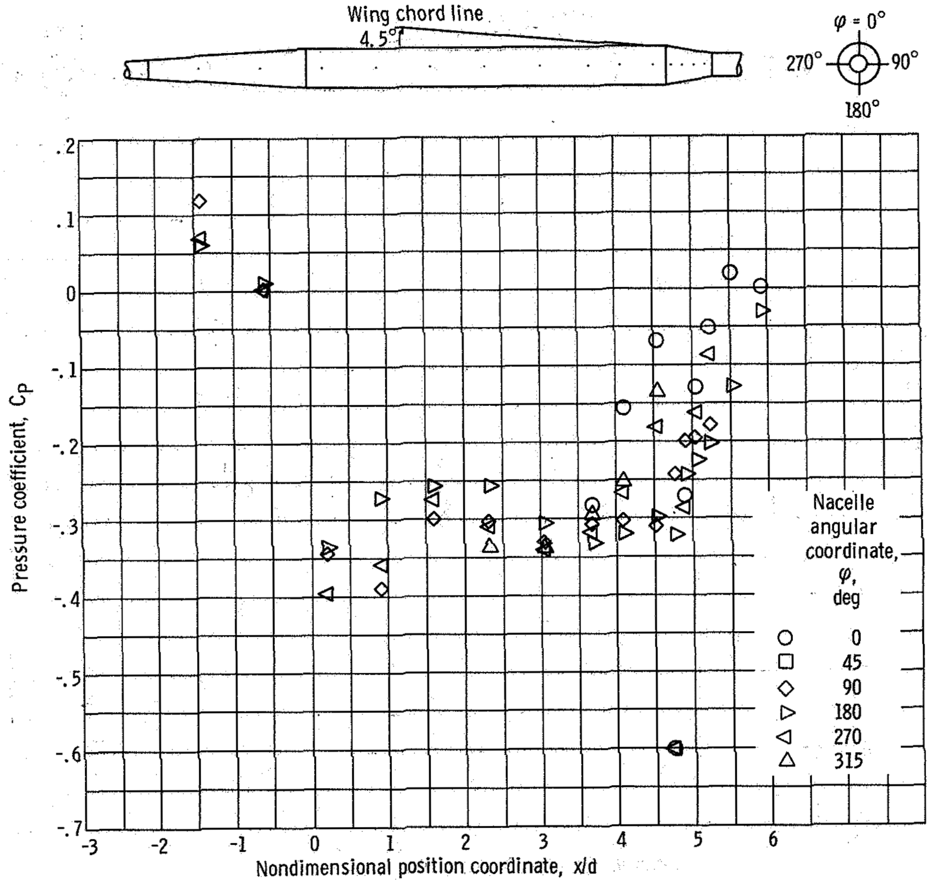

(f) Free-stream Mach number, 1.0.

Figure 21. - Continued.

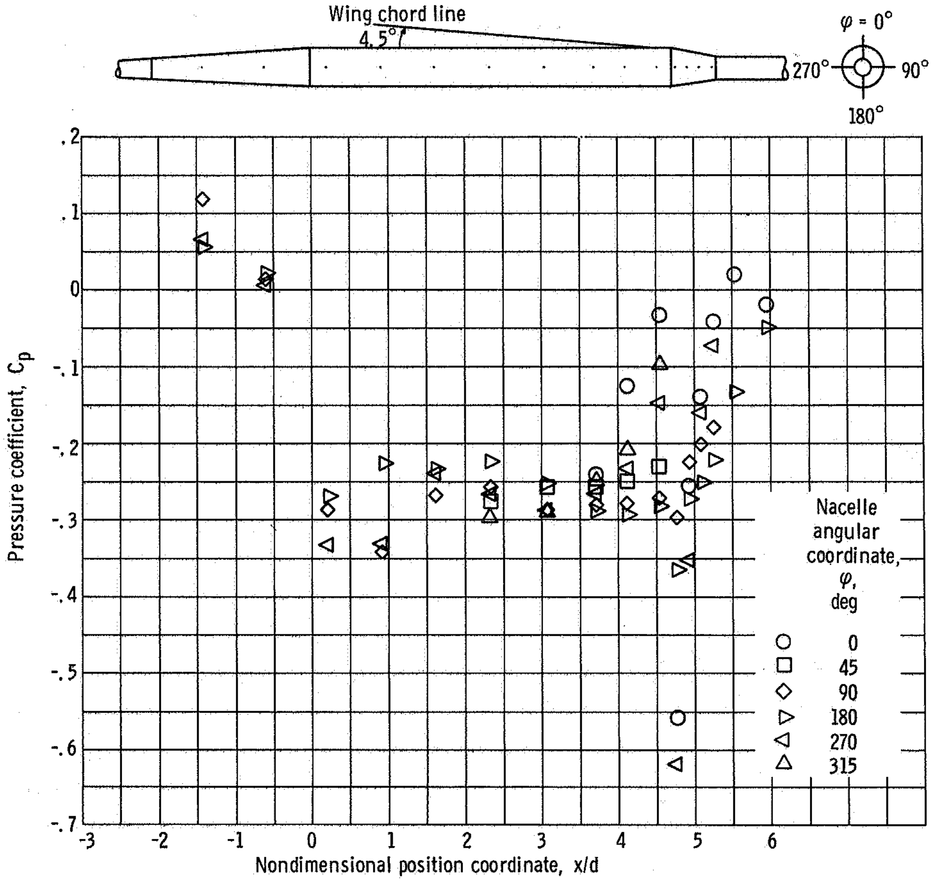

(g) Free-stream Mach number, 1.05.

Figure 21. - Continued.

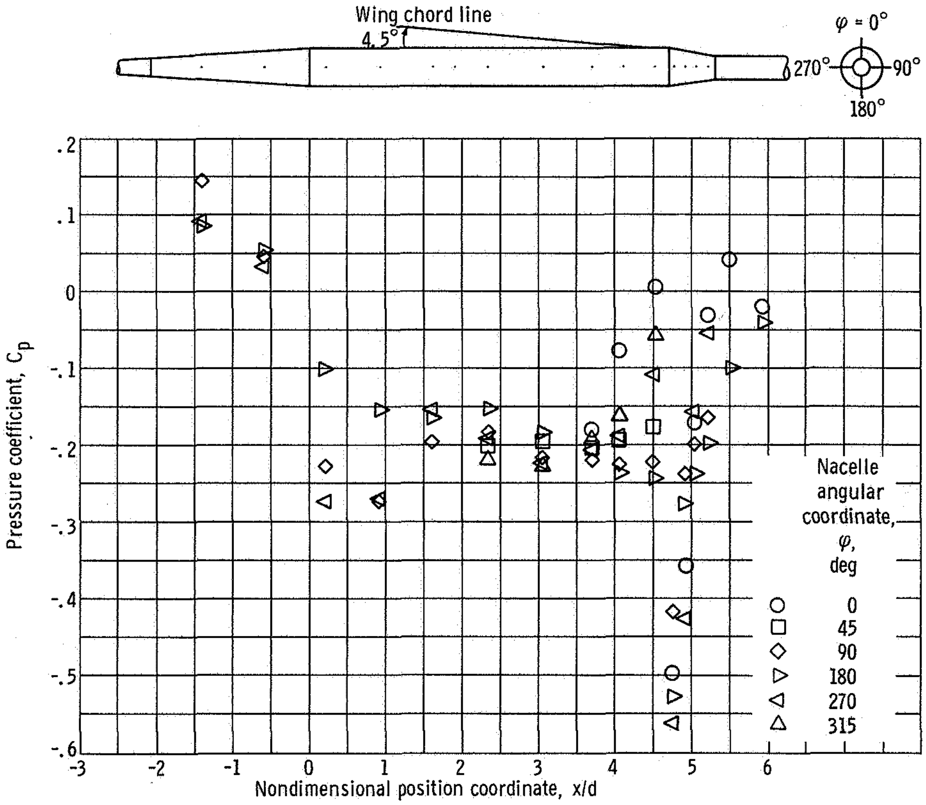

(h) Free-stream Mach number, 1.1.

Figure 21. - Continued.

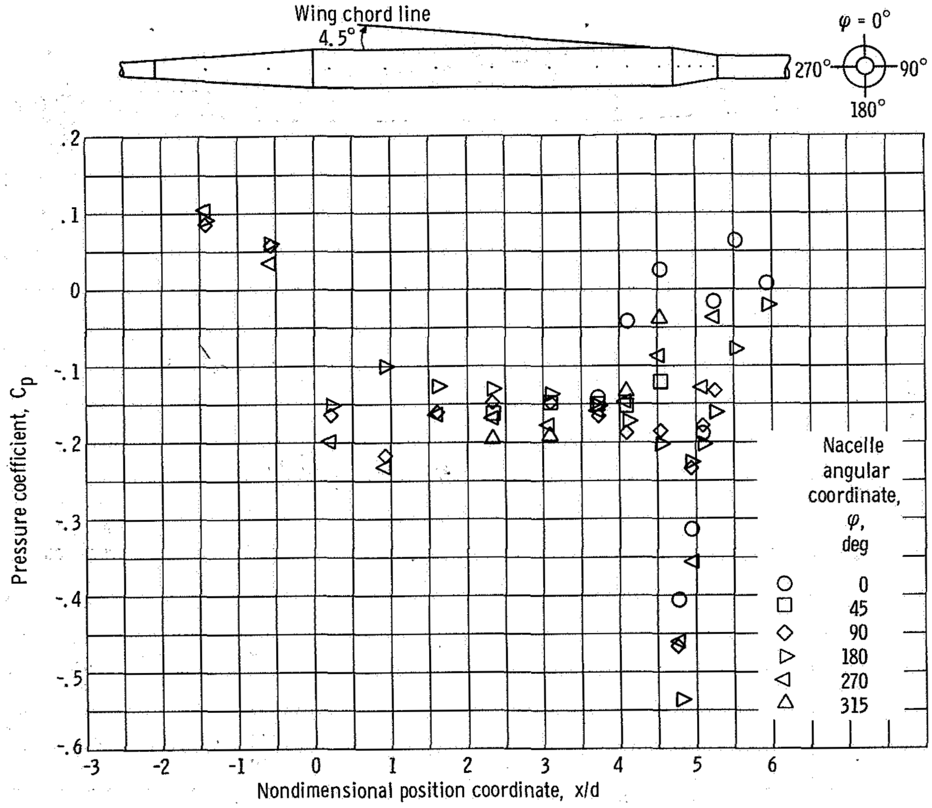

(i) Free-stream Mach number, 1.2.

Figure 21. - Continued.

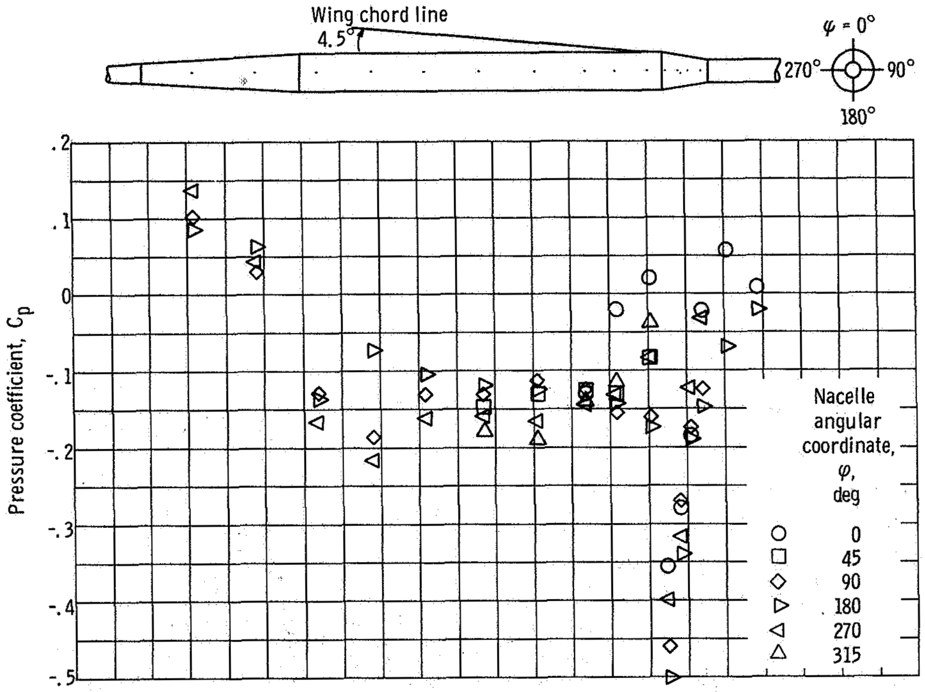

(j) Free-stream Mach number, 1.263.

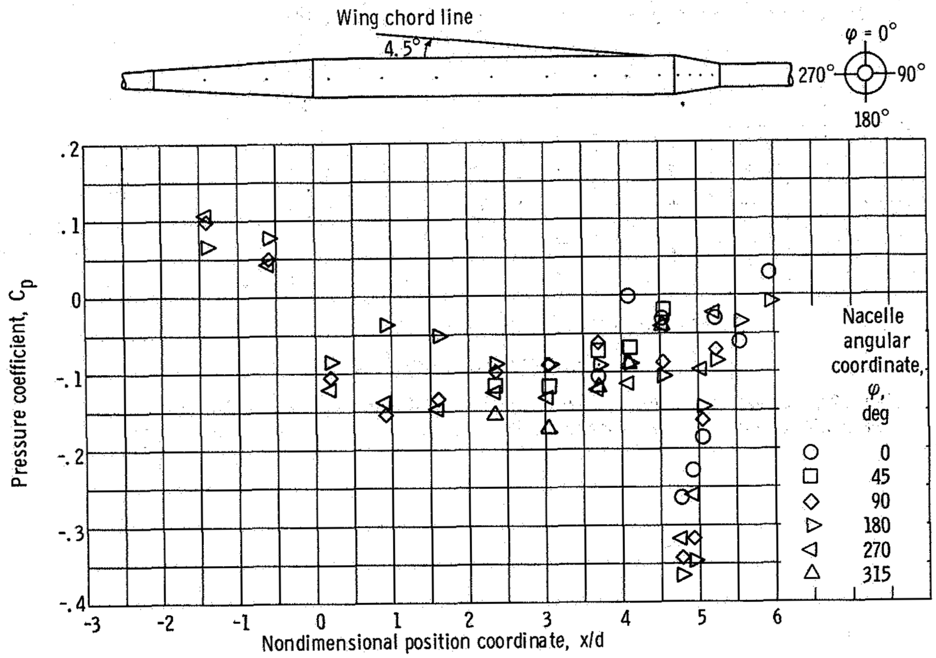

(k) Free-stream Mach number, 1.464.

Figure 21. - Concluded.

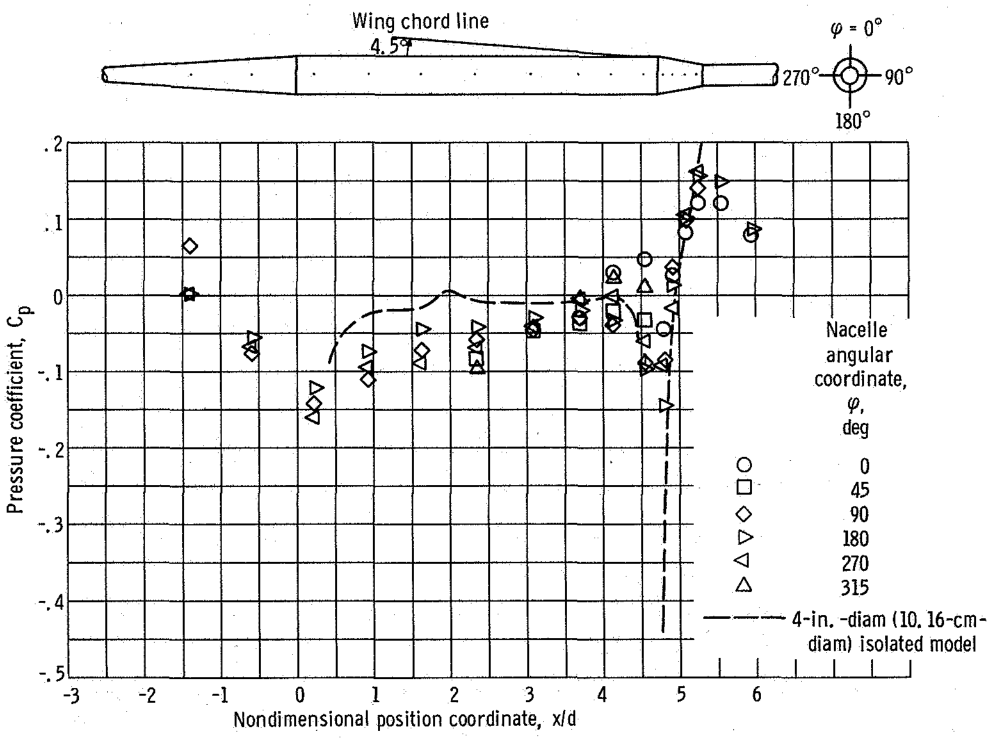

(a) Free-stream Mach number, 0.56.

Figure 22. - Comparison of pressure distribution on solid cylindrical nacelle at 4° model angle of attack with data from 4-inch-diameter (10.16-cm-diam) isolated model at 0° angle of attack.

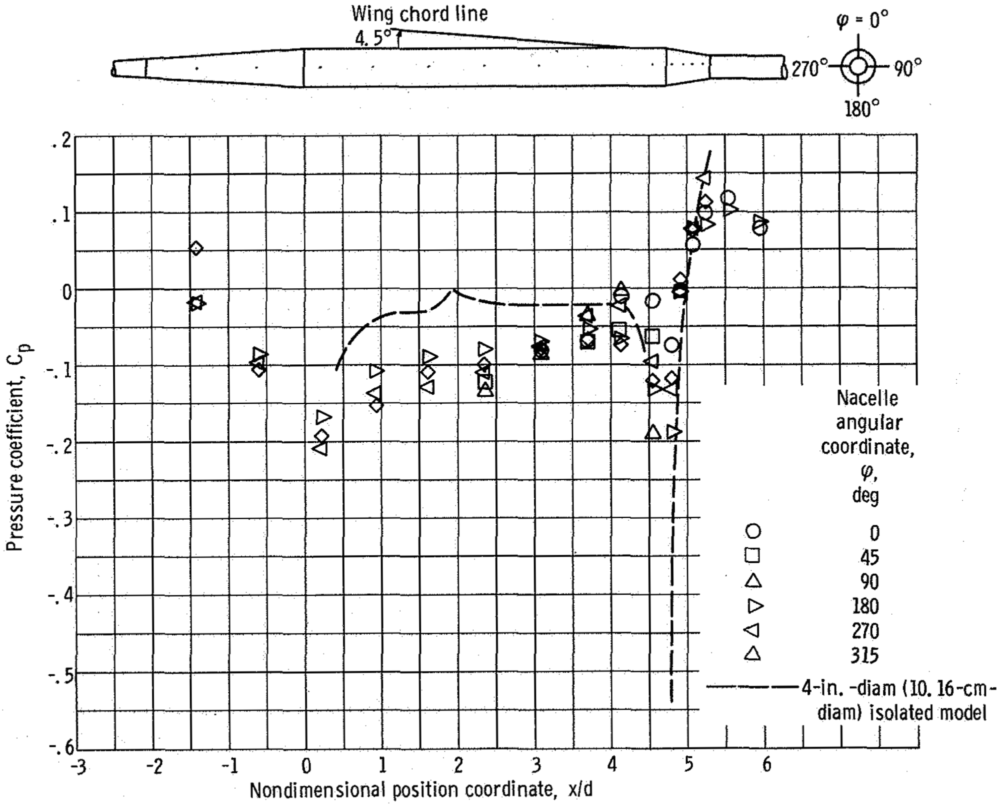

(b) Free-stream Mach number, 0.7.

Figure 22. - Continued.

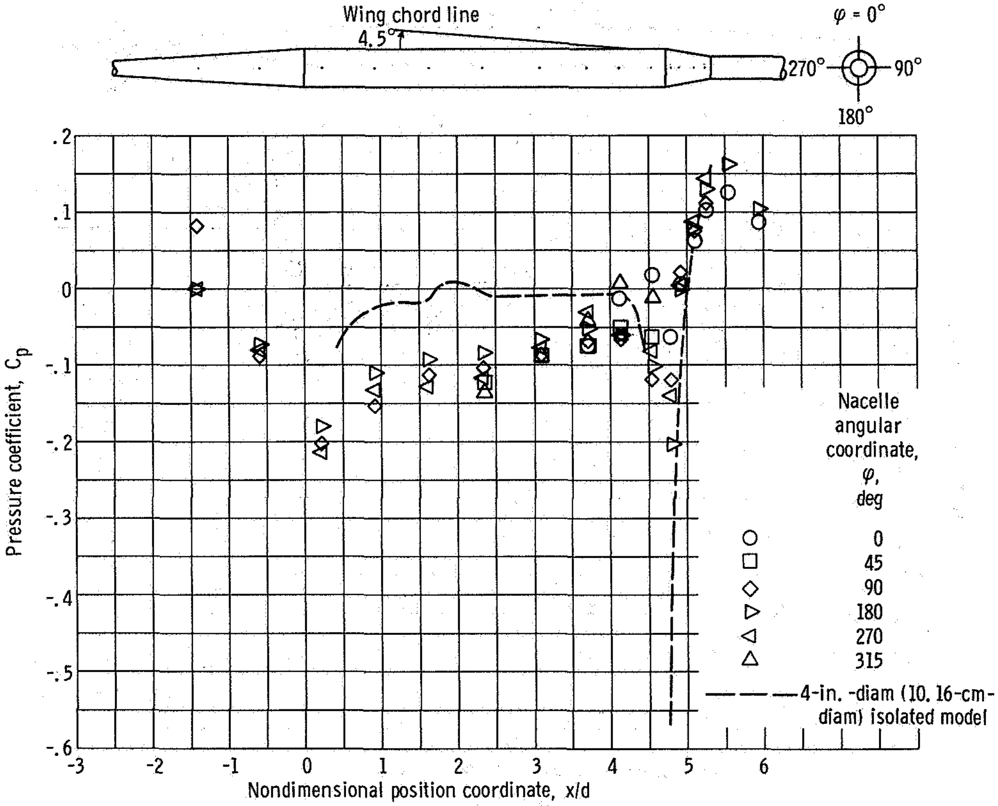

(c) Free-stream Mach number, 0.8.

Figure 22. - Continued.

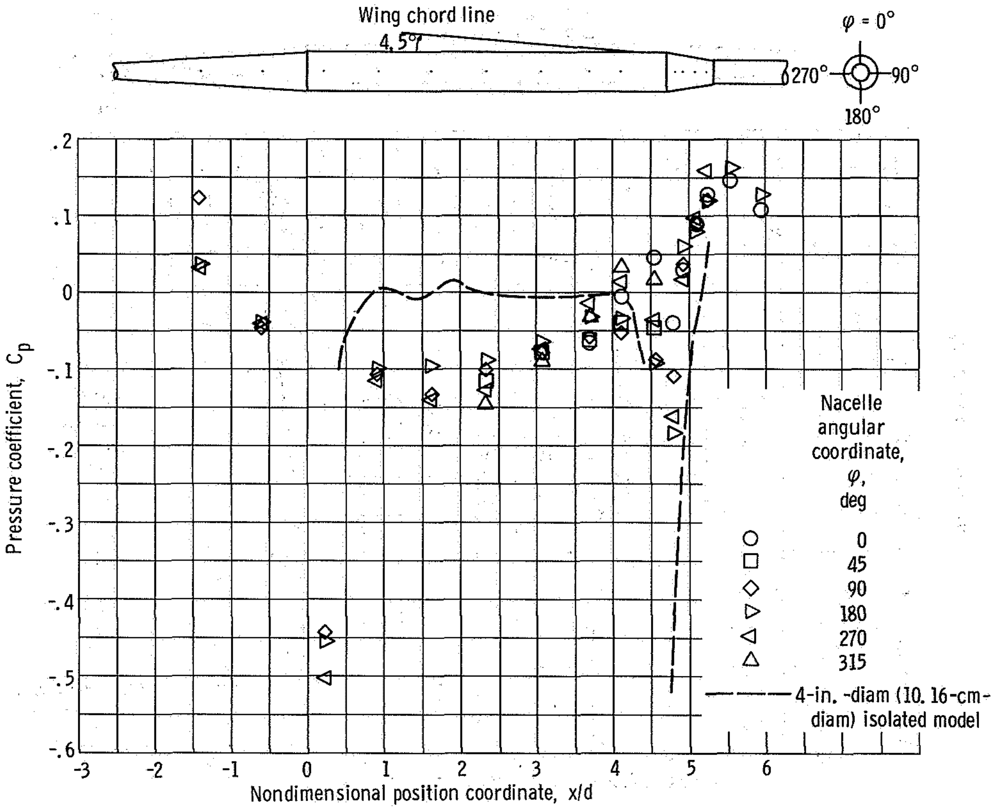

(d) Free-stream Mach number, 0.9.

Figure 22. - Continued.

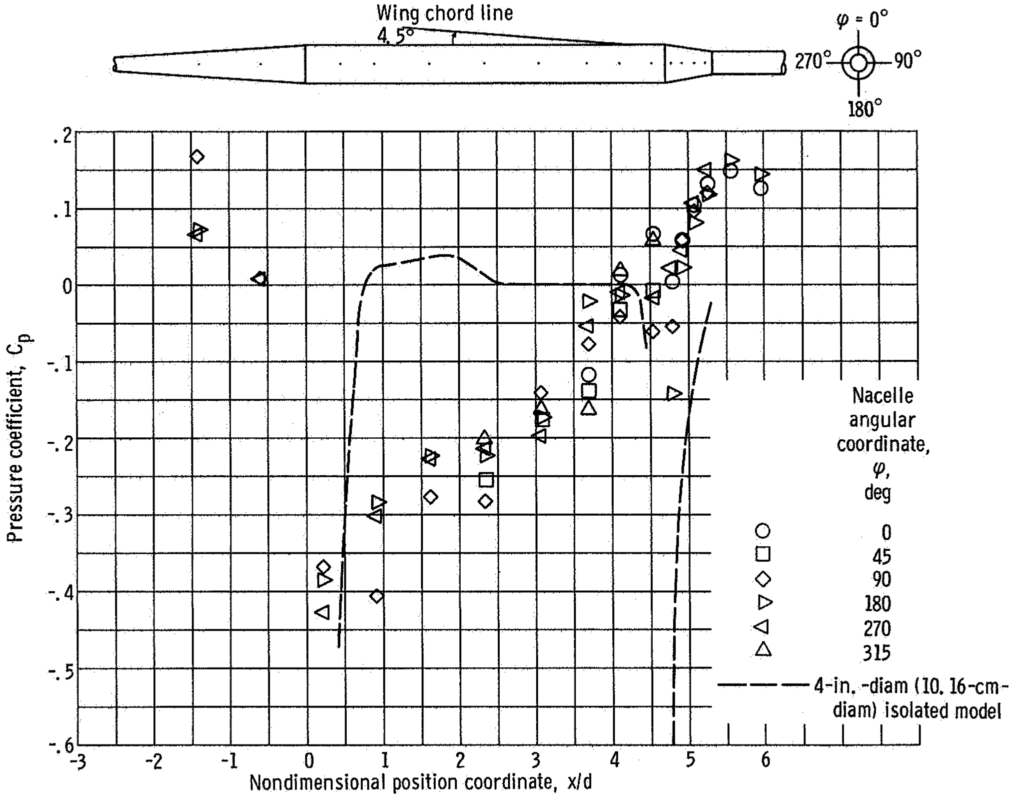

(e) Free-stream Mach number, 0.95.

Figure 22. - Continued.

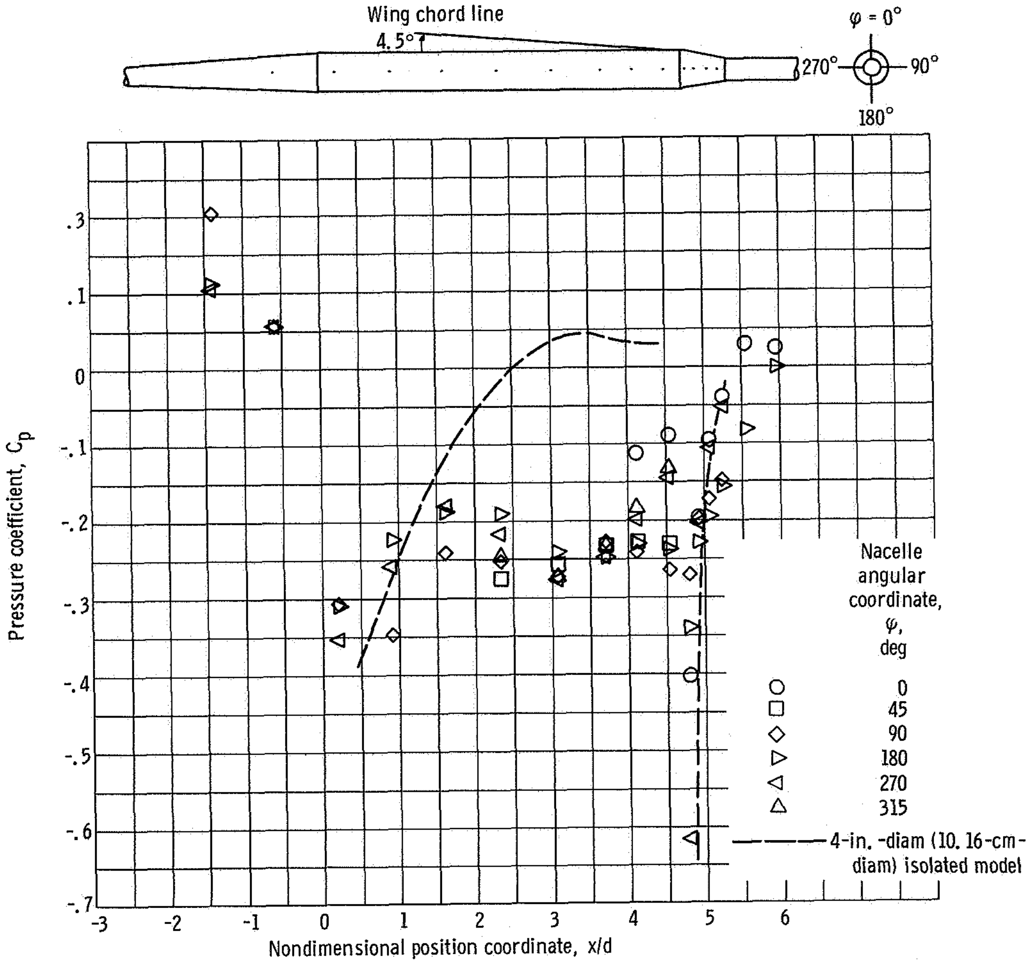

(f) Free-stream Mach number, 1.0.

Figure 22. - Continued.

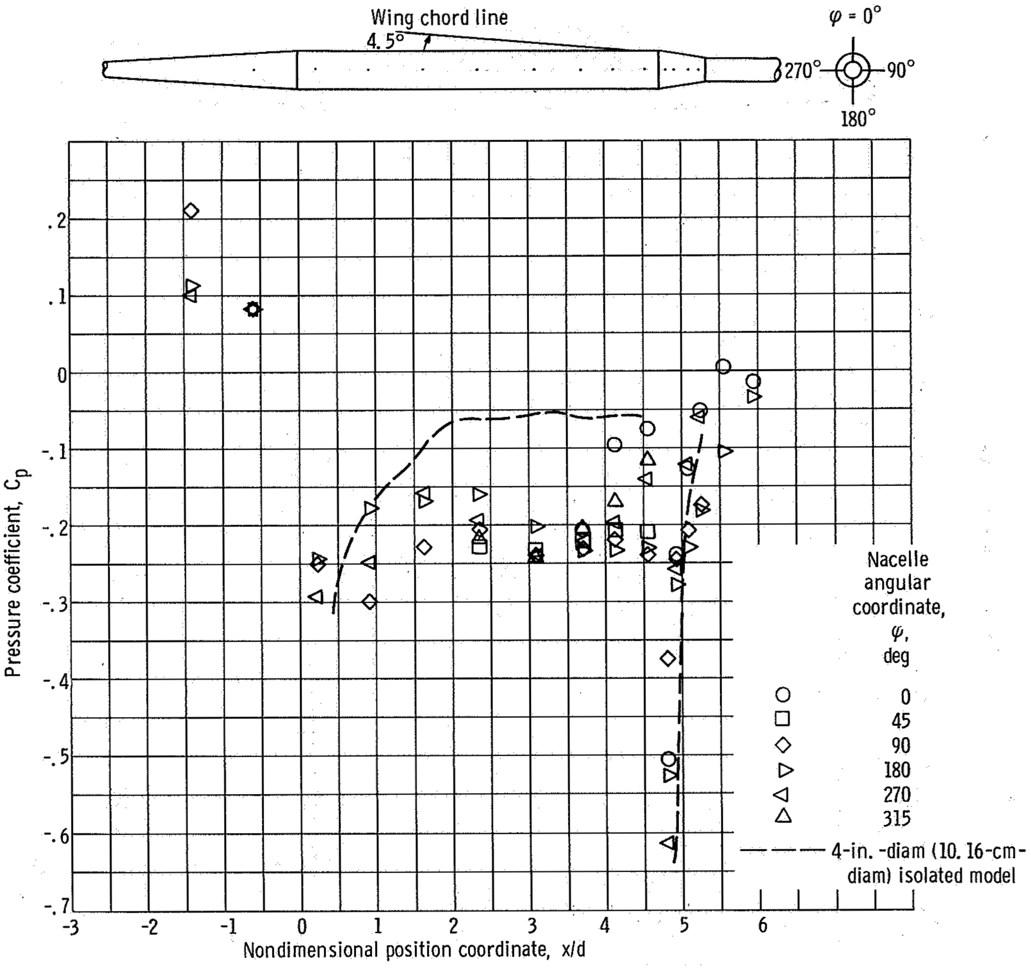

(g) Free-stream Mach number, 1.05.

Figure 22. - Continued.

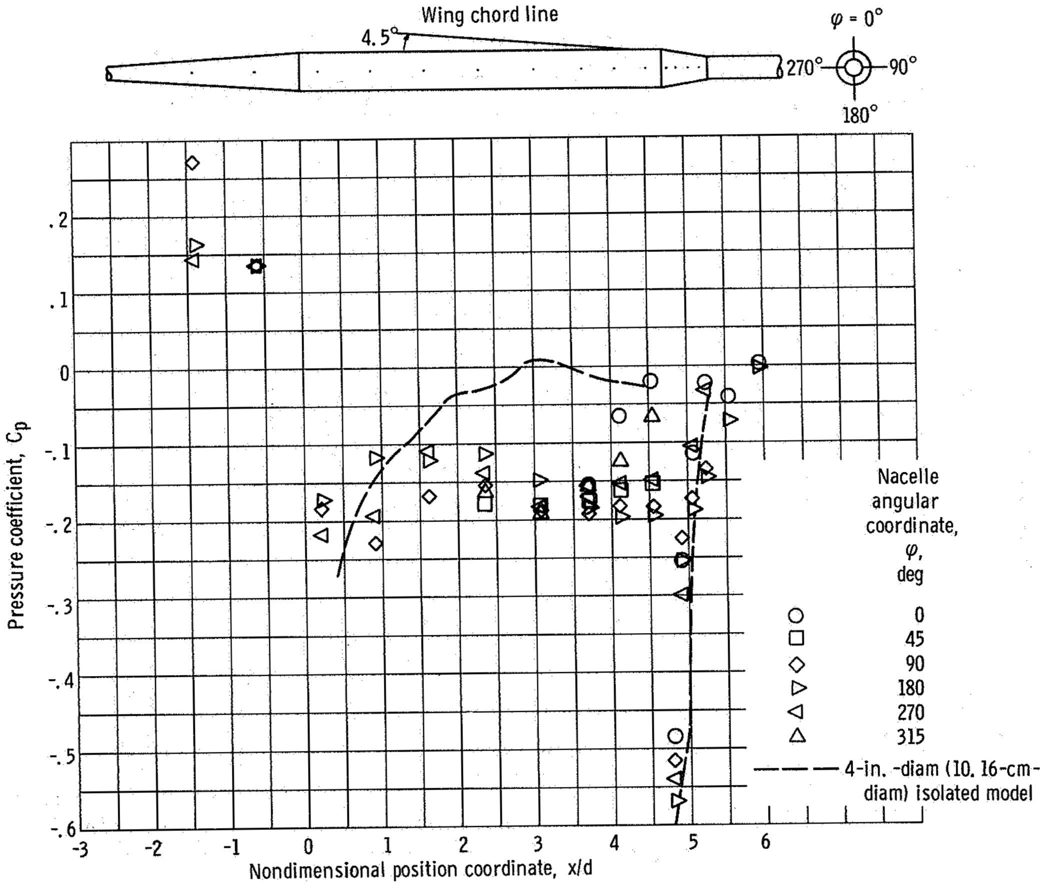

(h) Free-stream Mach number, 1.1.

Figure 22. - Continued.

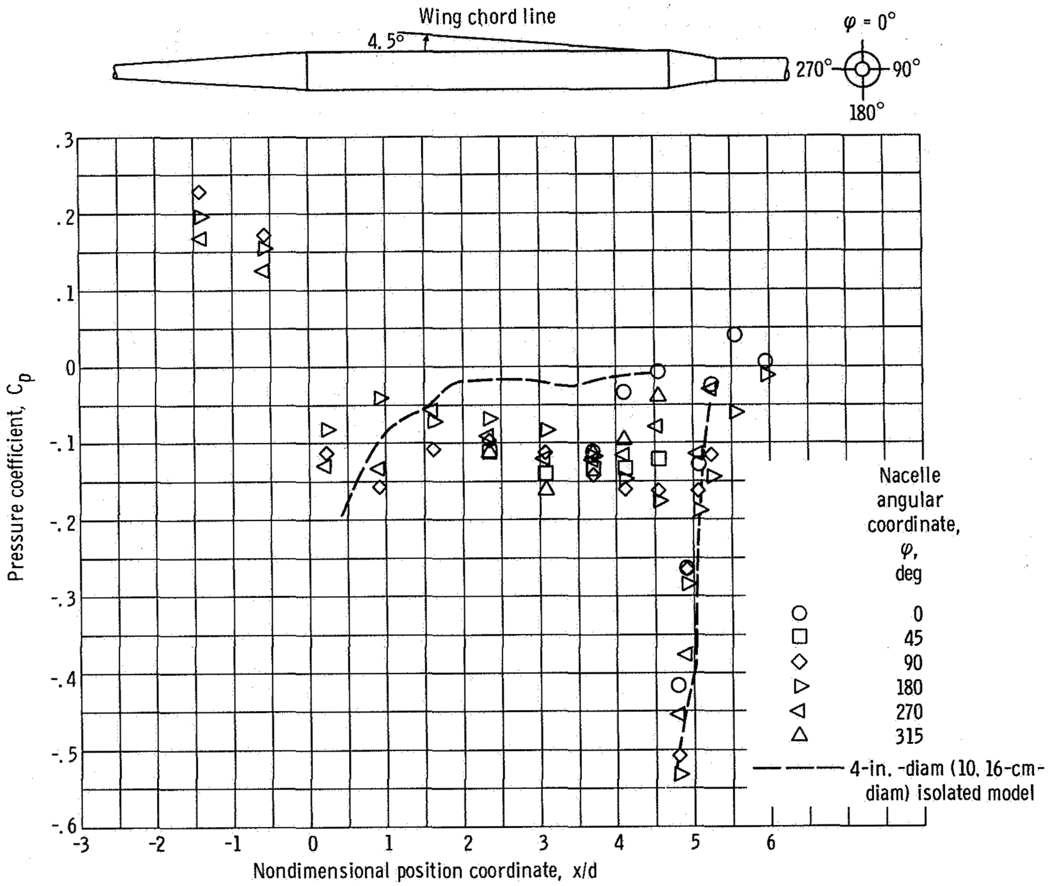

(i) Free-stream Mach number, 1.2.

Figure 22. - Concluded.

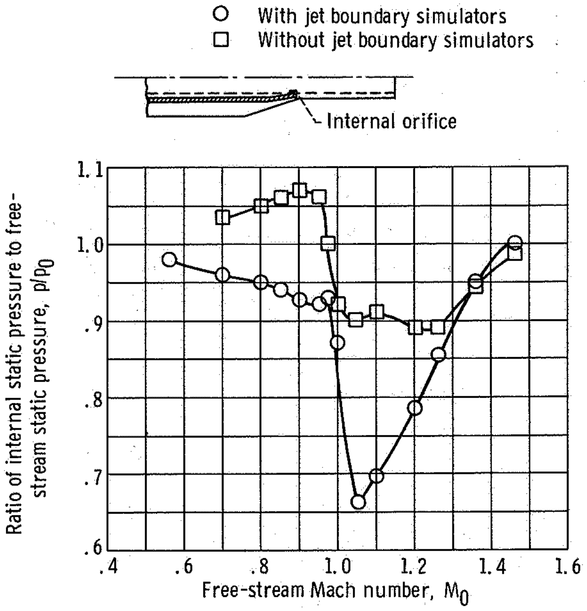

Figure 23. - Open-nacelle internal static pressure as function of free-stream Mach number.

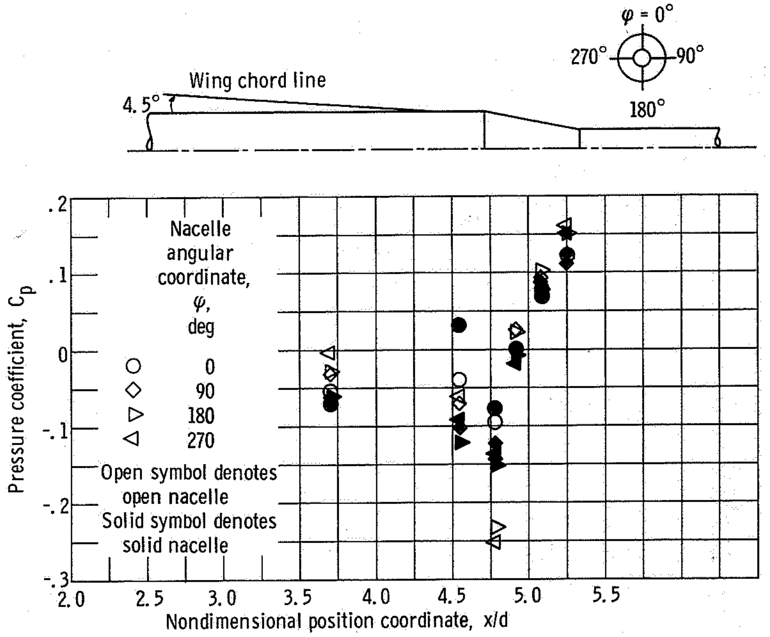

(a) Free-stream Mach number, 0.56.

Figure 24. - Comparison of solid- and open-nose nacelle pressures; cylindrical nacelles with narrow struts and rectangular elevon cutouts of 0° angle of attack and 0° elevon angle.

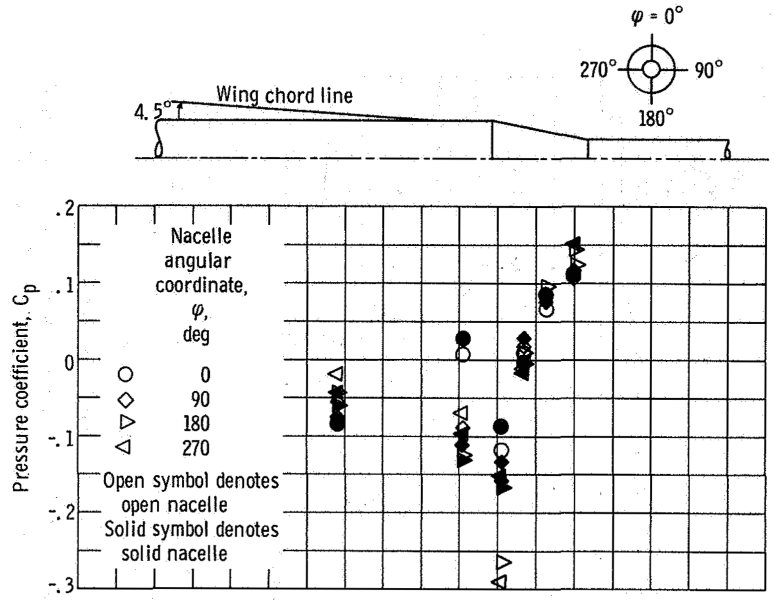

(b) Free-stream Mach number, 0.7.

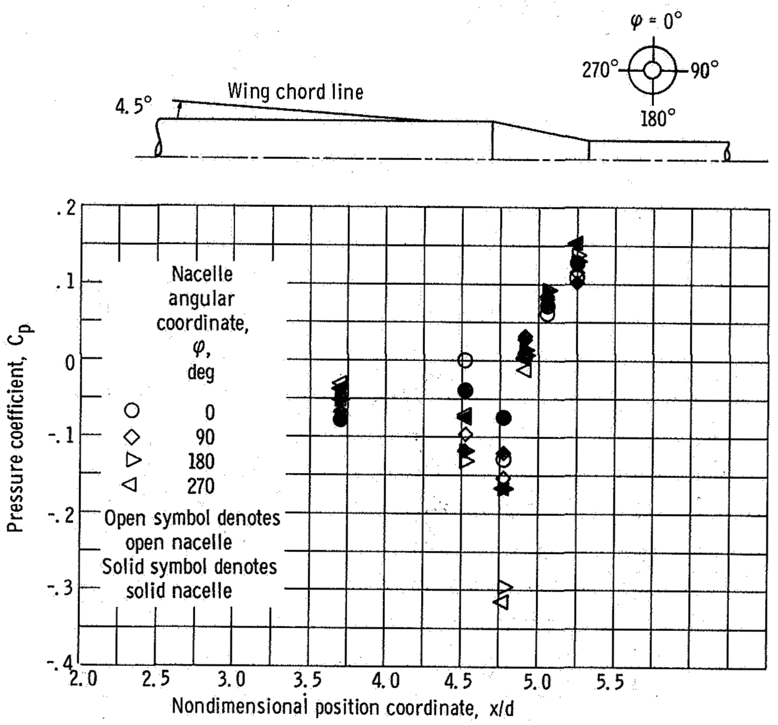

(c) Free-stream Mach number, 0.8.

Figure 24. - Continued.

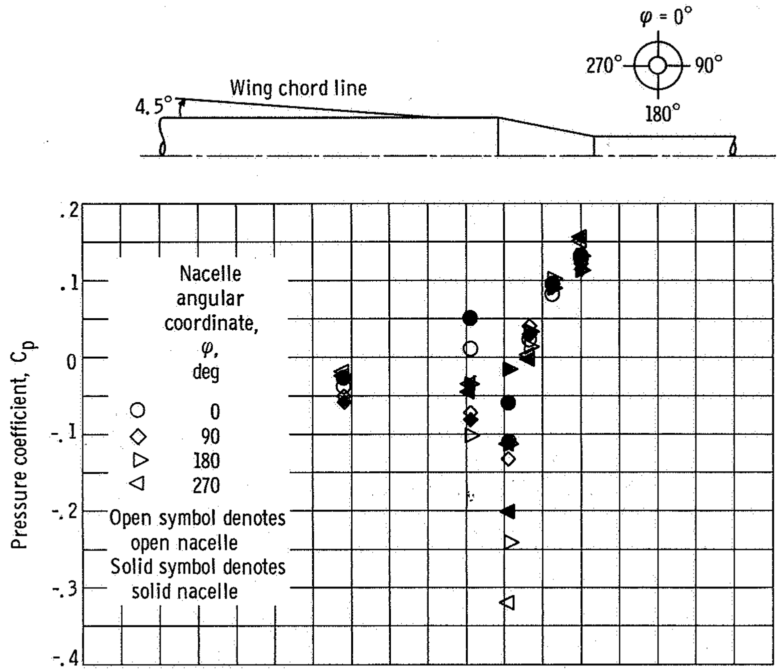

(d) Free-stream Mach number, 0.9.

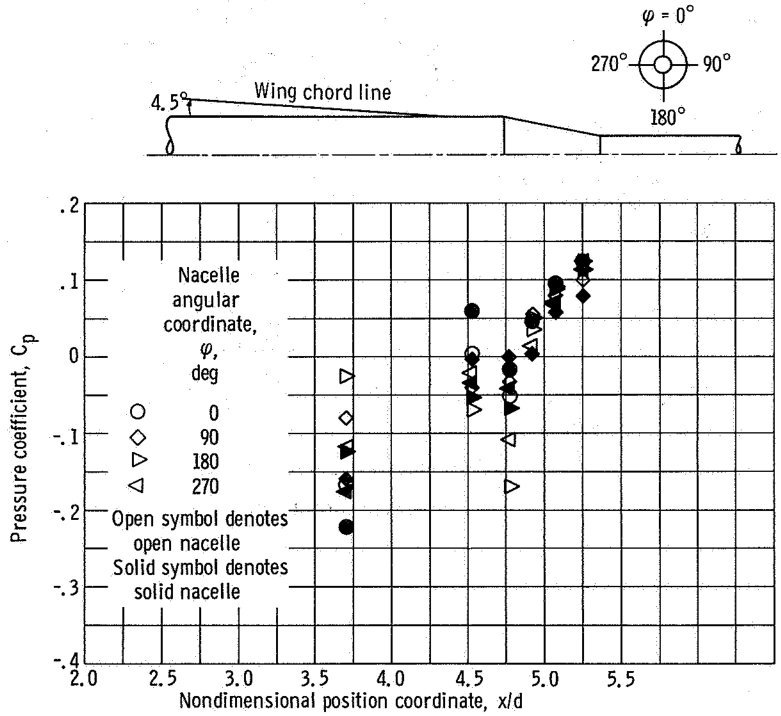

(e) Free-stream Mach number, 0.95.

Figure 24. - Continued.

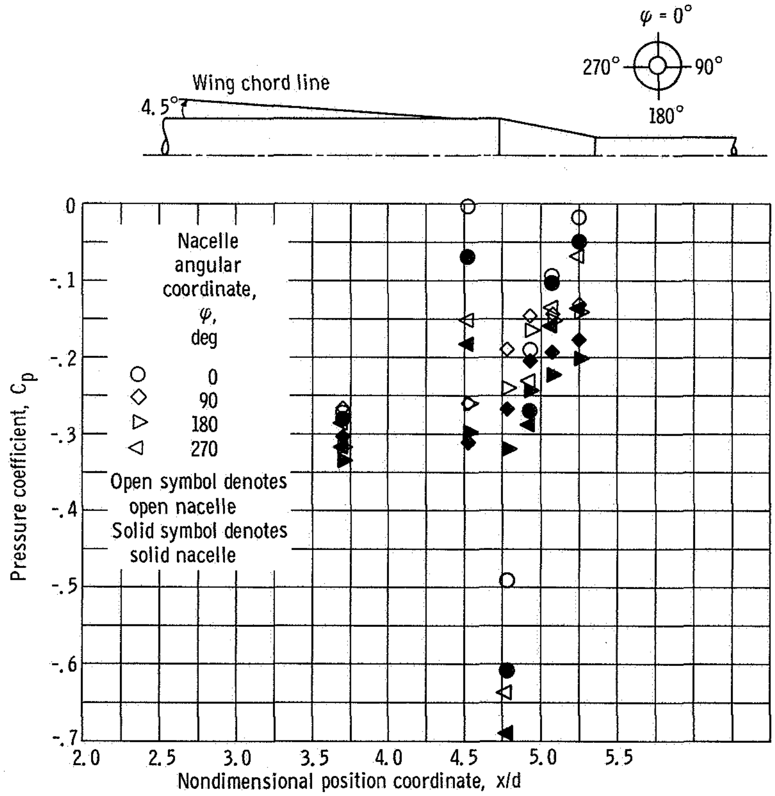

(f) Free-stream Mach number, 1.0.

Figure 24. - Continued.

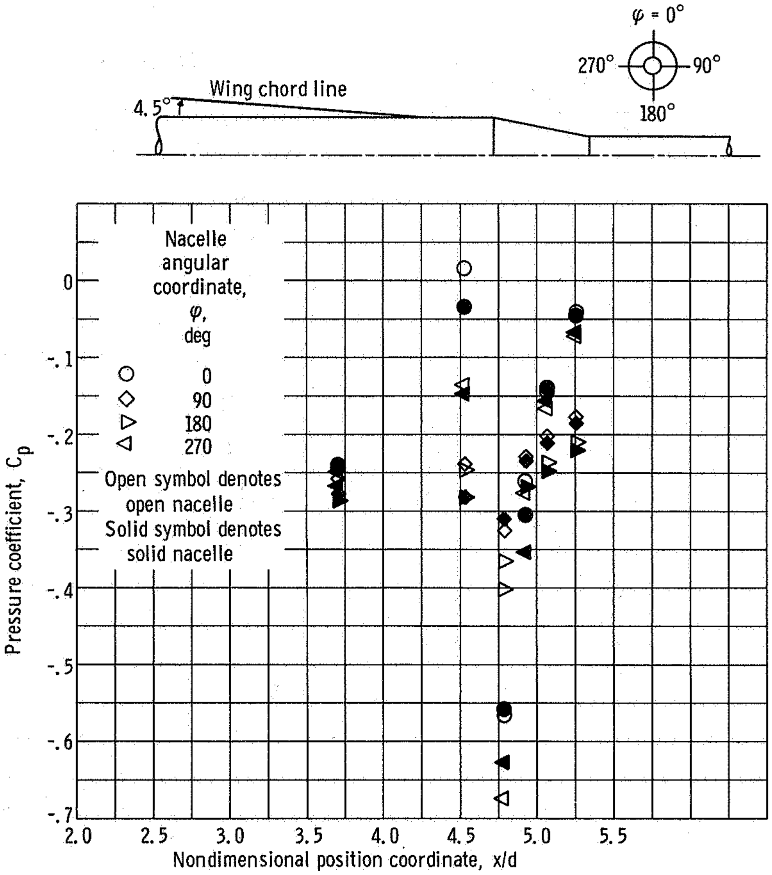

(g) Free-stream Mach number, 1.05.

Figure 24. - Continued.

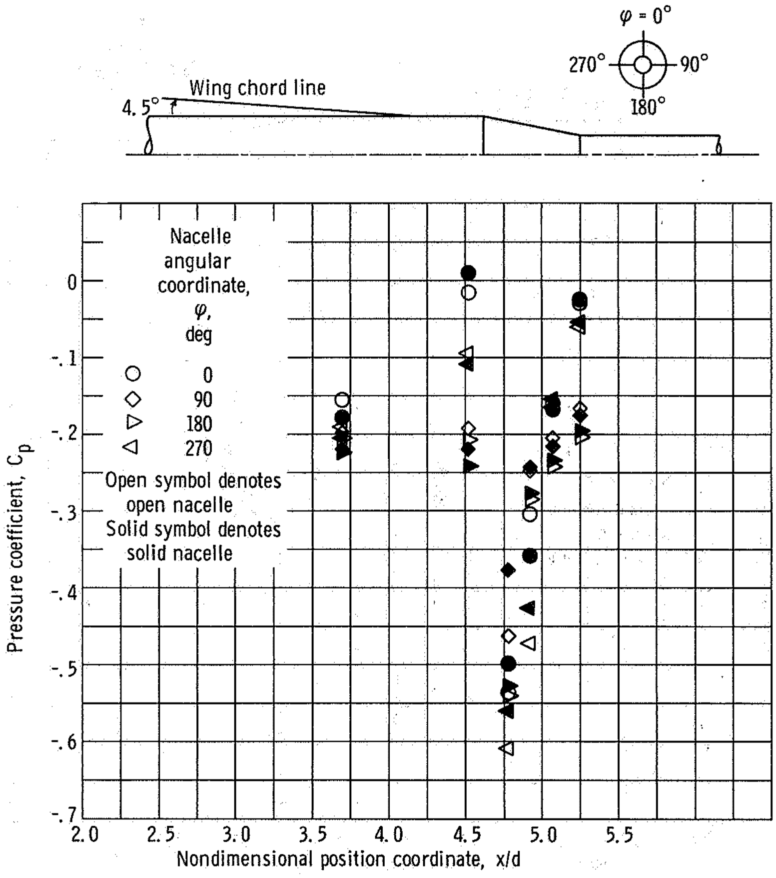

(h) Free-stream Mach number, 1.1.

Figure 24. - Continued.

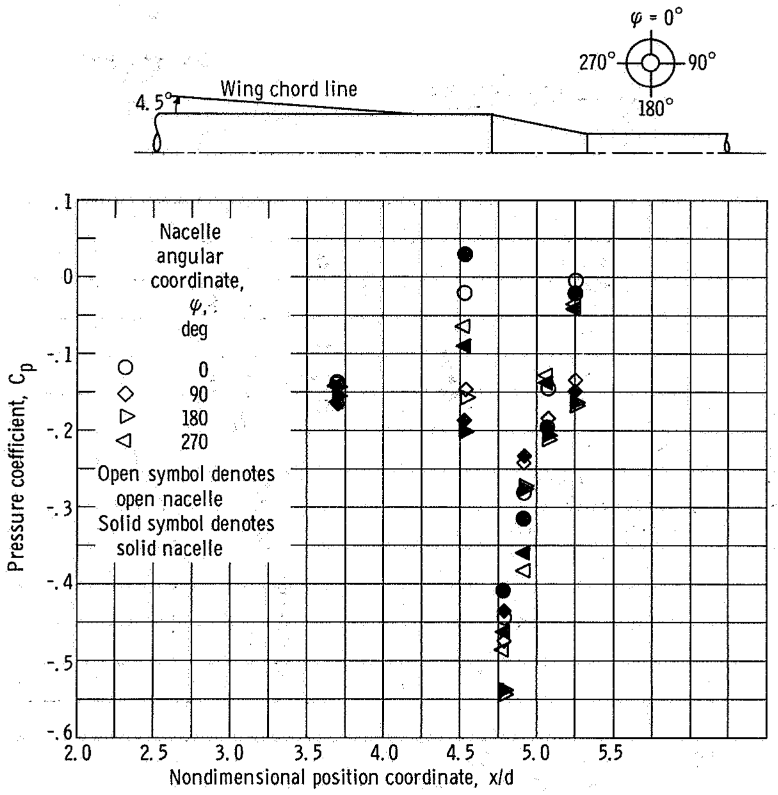

(i) Free-stream Mach number, 1.2.

Figure 24. - Continued.

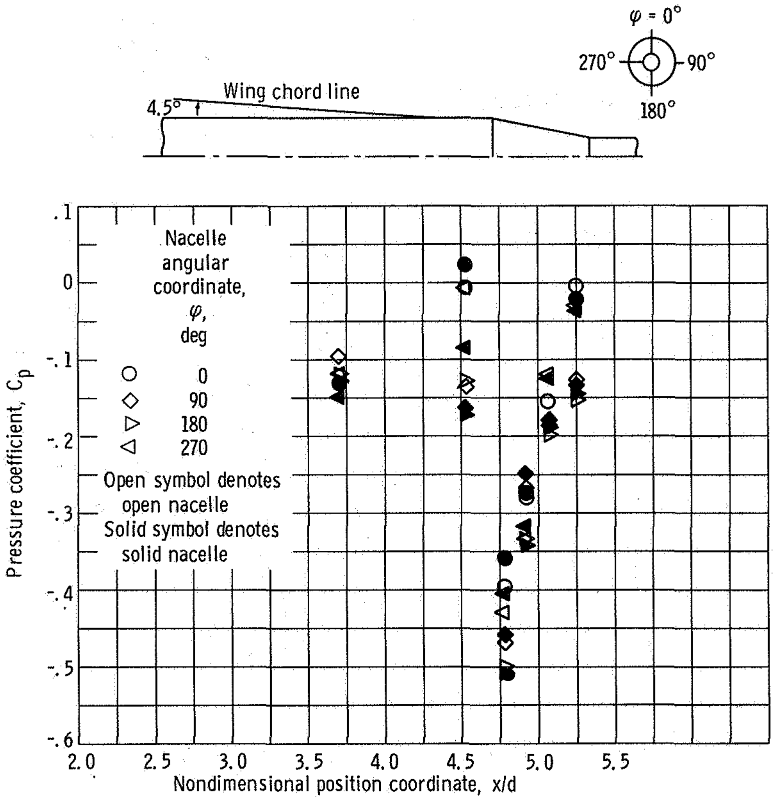

(j) Free-stream Mach number, 1.26.

Figure 24. - Continued.

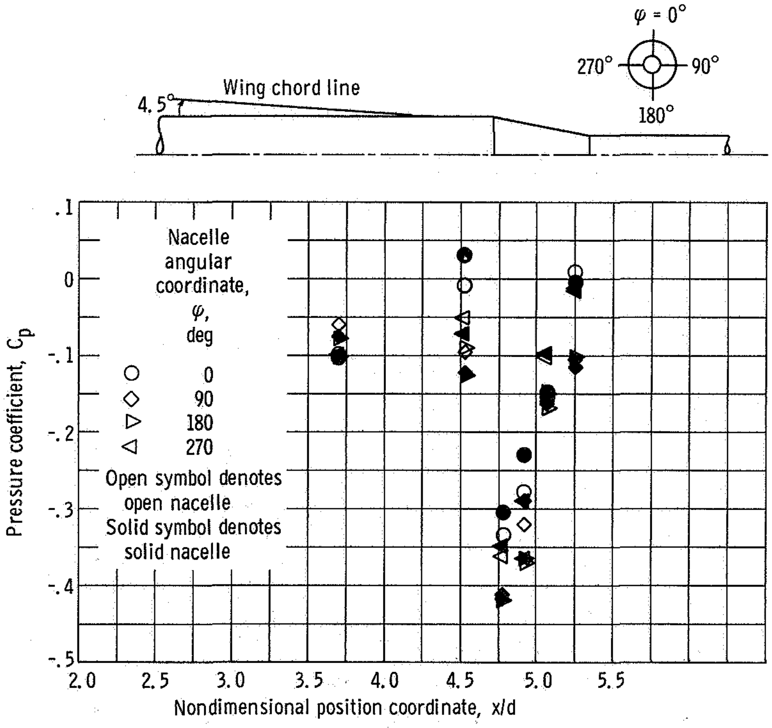

(k) Free-stream Mach number, 1.37.

Figure 24. - Continued.

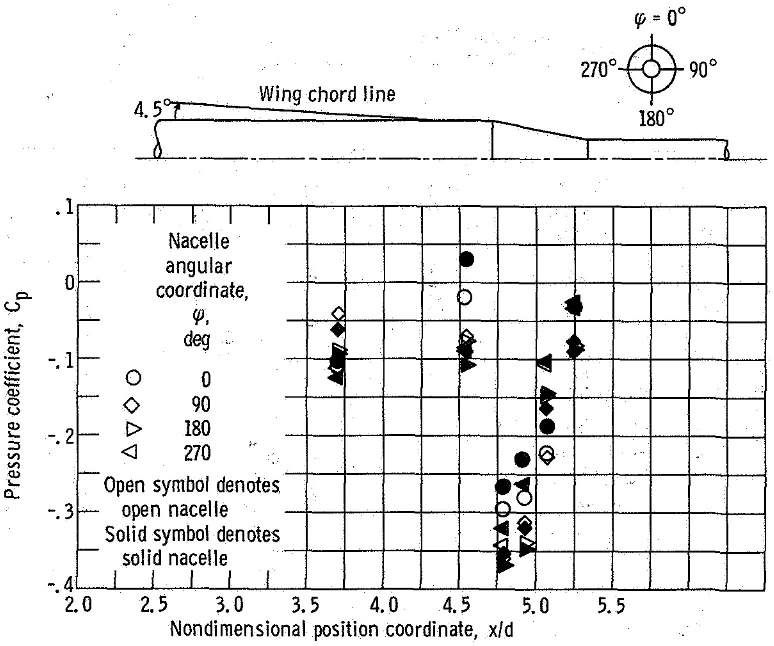

(ℓ) Free-stream Mach number, 1.46.

Figure 24. - Concluded.

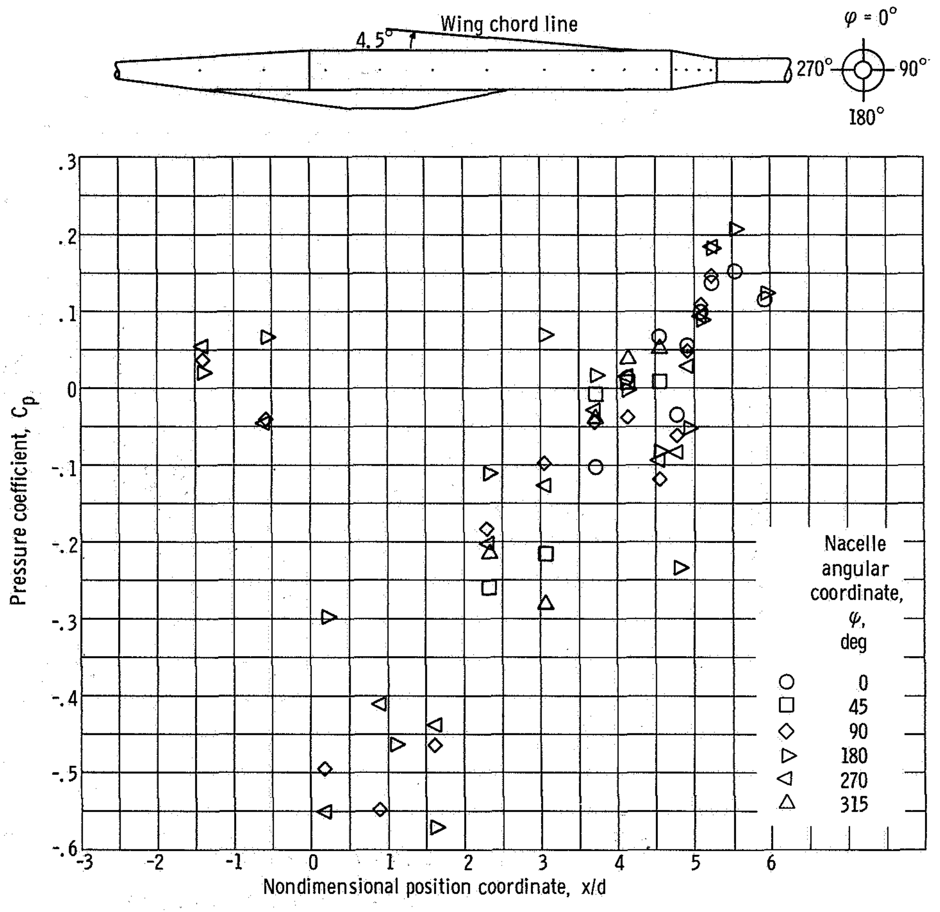

(a) Free-stream Mach number, 0.9.

Figure 25. - Pressure distribution on left solid bulged nacelle; narrow nacelle struts and rectangular elevon cutouts at 0° angle of attack and 0° elevon angle.

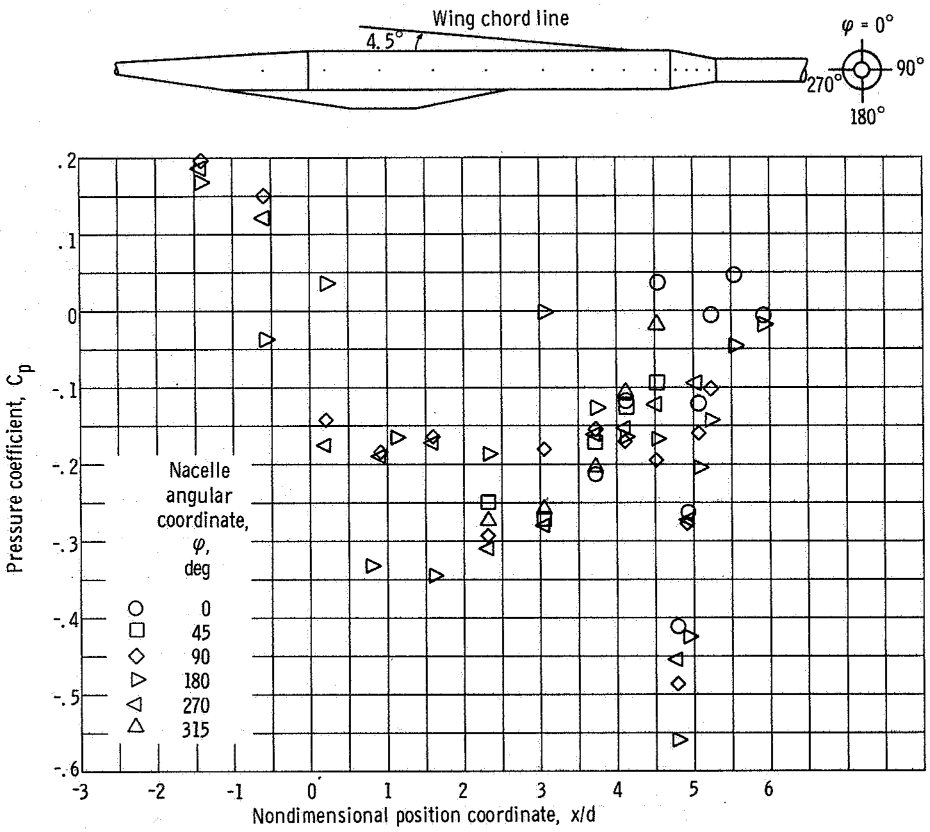

(b) Free-stream Mach number, 1.2.

Figure 25. - Concluded.

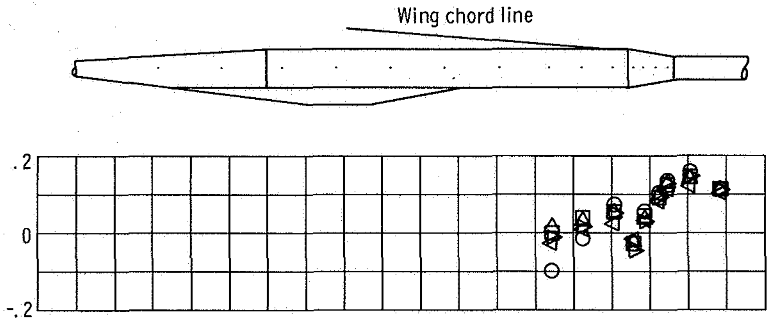

(a-1) Angular coordinate, 0°.

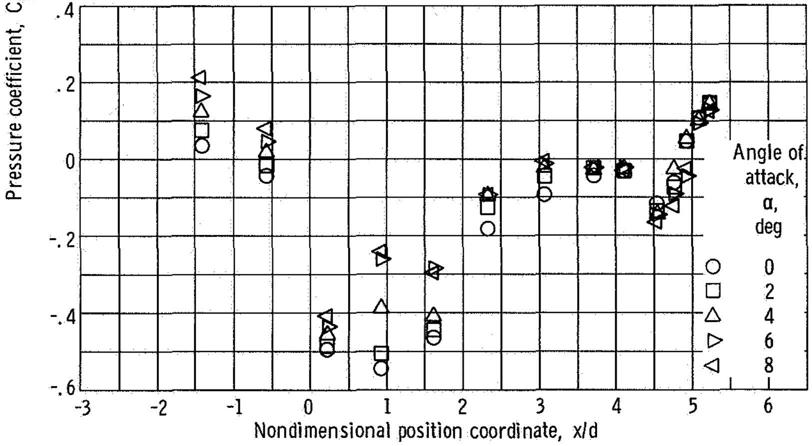

(a-2) Angular coordinate, 90°.

(a) Free-stream Mach number, 0.9.

Figure 26. - Effect of model angle of attack on solid-bulged-nacelle pressure distribution; narrow struts, rectangular elevon cutouts, and elevons at 0°.

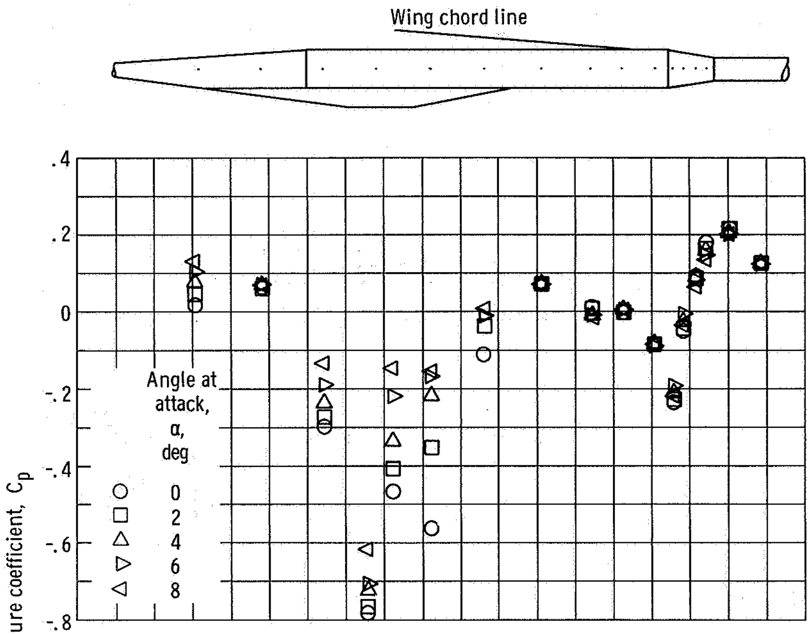

(a-3) Angular coordinate, 180°.

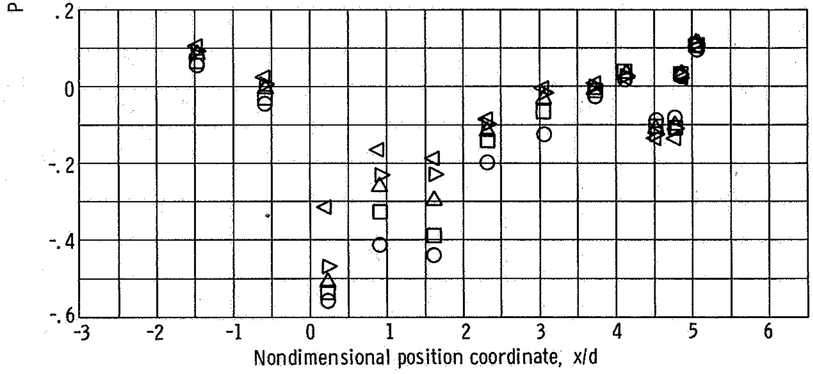

(a-4) Angular coordinate, 270°.

(a) Concluded.

Figure 26. - Continued.

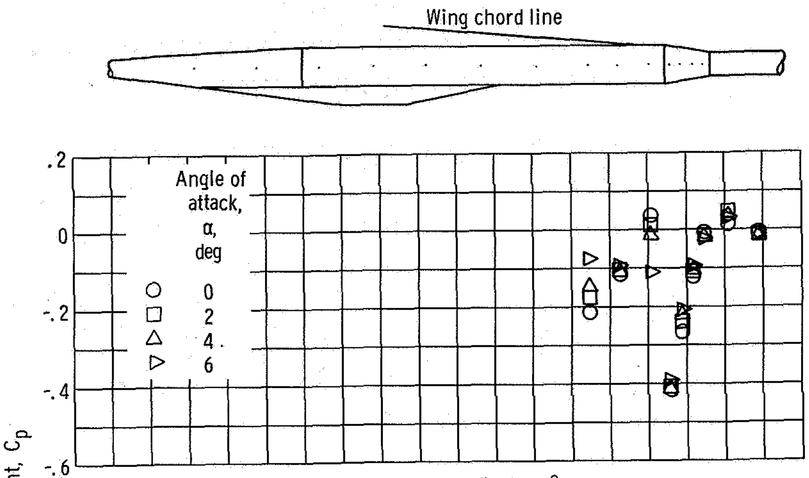

(b-1) Angular coordinate, 0°.

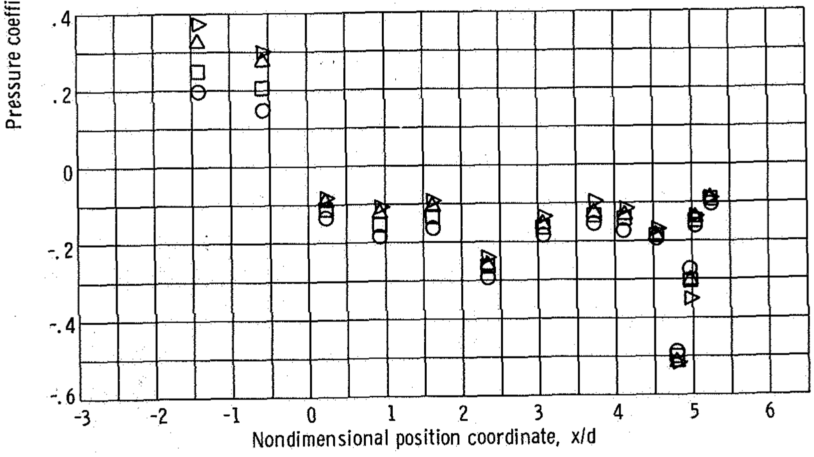

(b-2) Angular coordinate, 90°.

(b) Free-stream Mach number, 1.2.

Figure 26. - Continued.

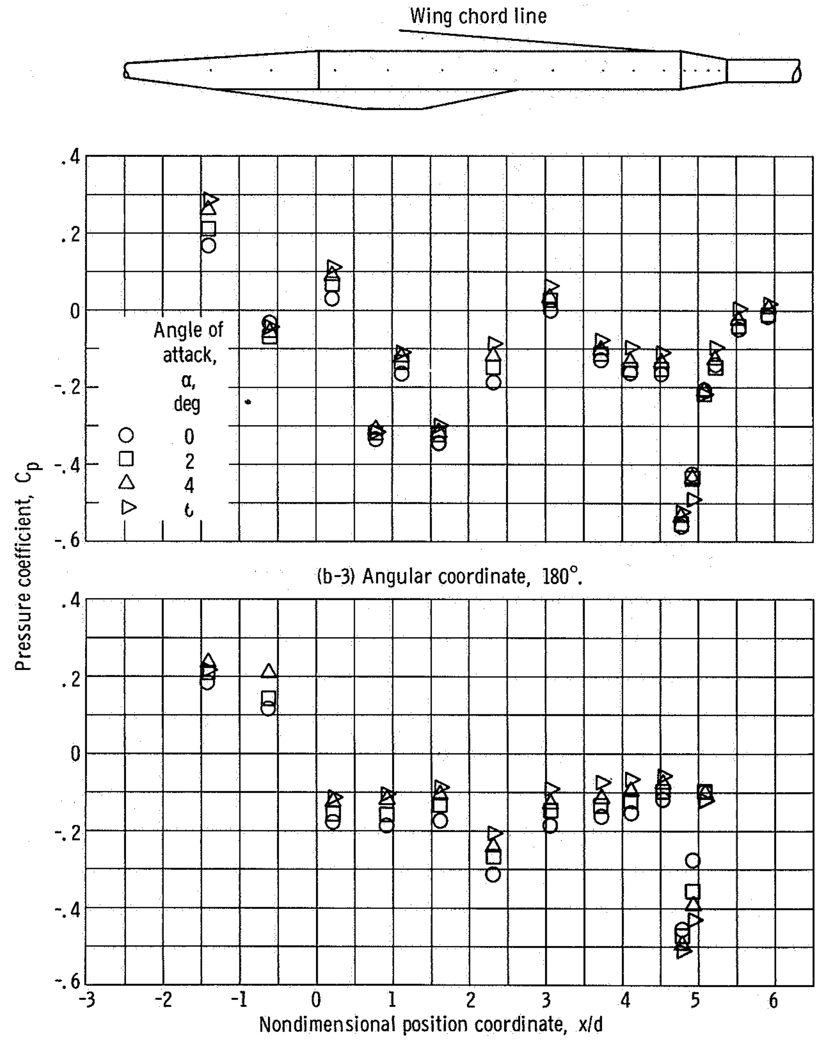

(b-3) Angular coordinate, 180°.

(b-4) Angular coordinate, 270°.

(b) Concluded.

Figure 26. - Concluded.

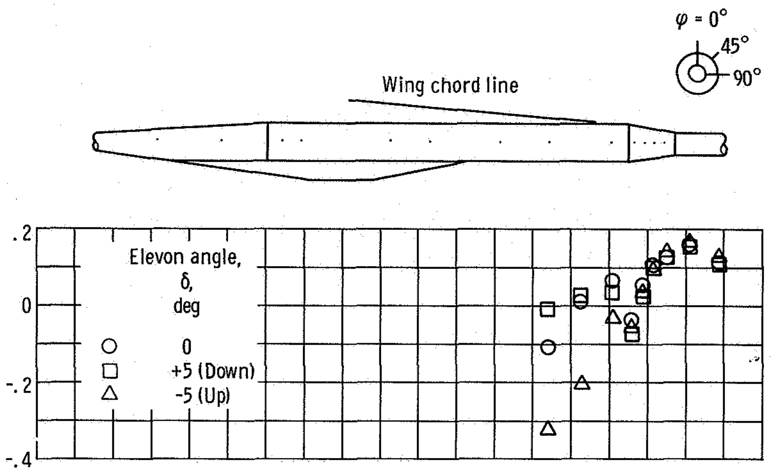

(a-1) Angular coordinate, 0°.

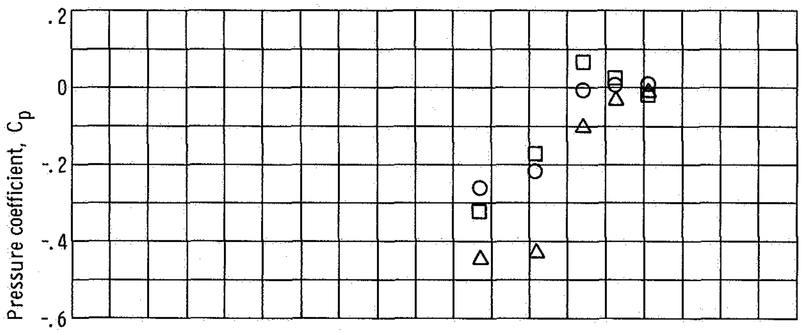

(a-2) Angular coordinate, 45°.

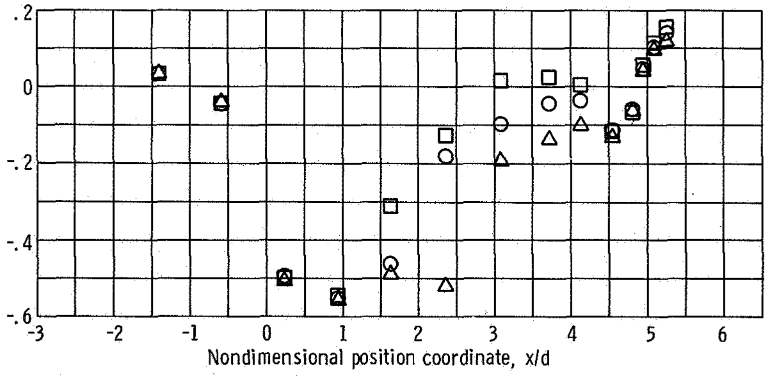

(a-3) Angular coordinate, 90°.

(a) Free-stream Mach number, 0.9.

Figure 27. - Effect of elevon angle on nacelle pressure distribution; solid bulged nacelles with narrow struts and rectangular elevon cutouts at 0° angle of attack.

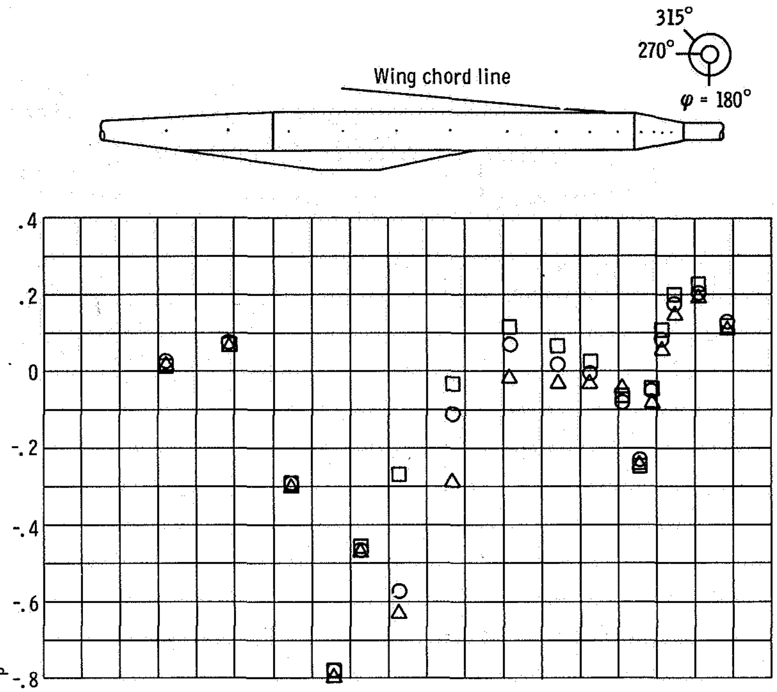

(a-4) Angular coordinate, 180°.

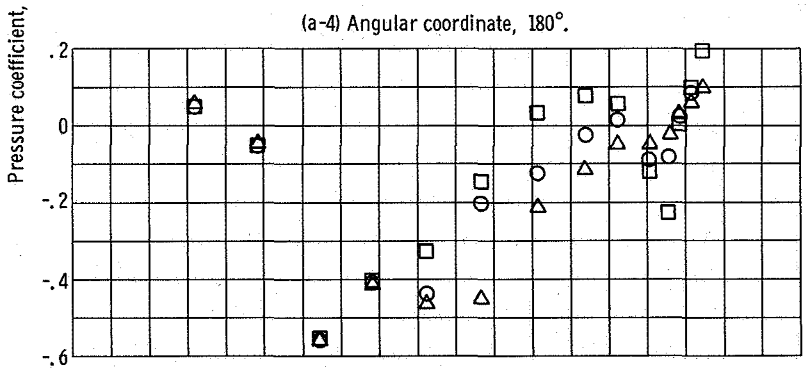

(a-5) Angular coordinate, 270°.

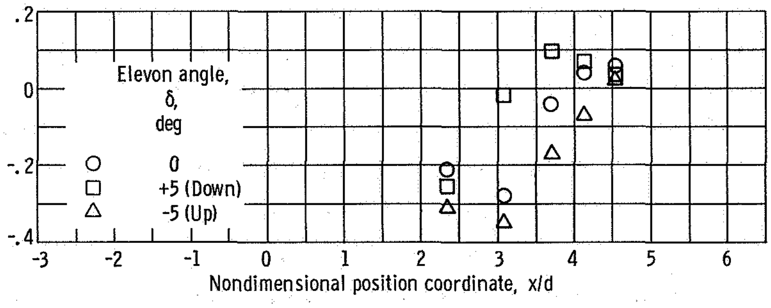

(a-6) Angular coordinate, 315°.

(a) Concluded.

Figure 27. - Continued.

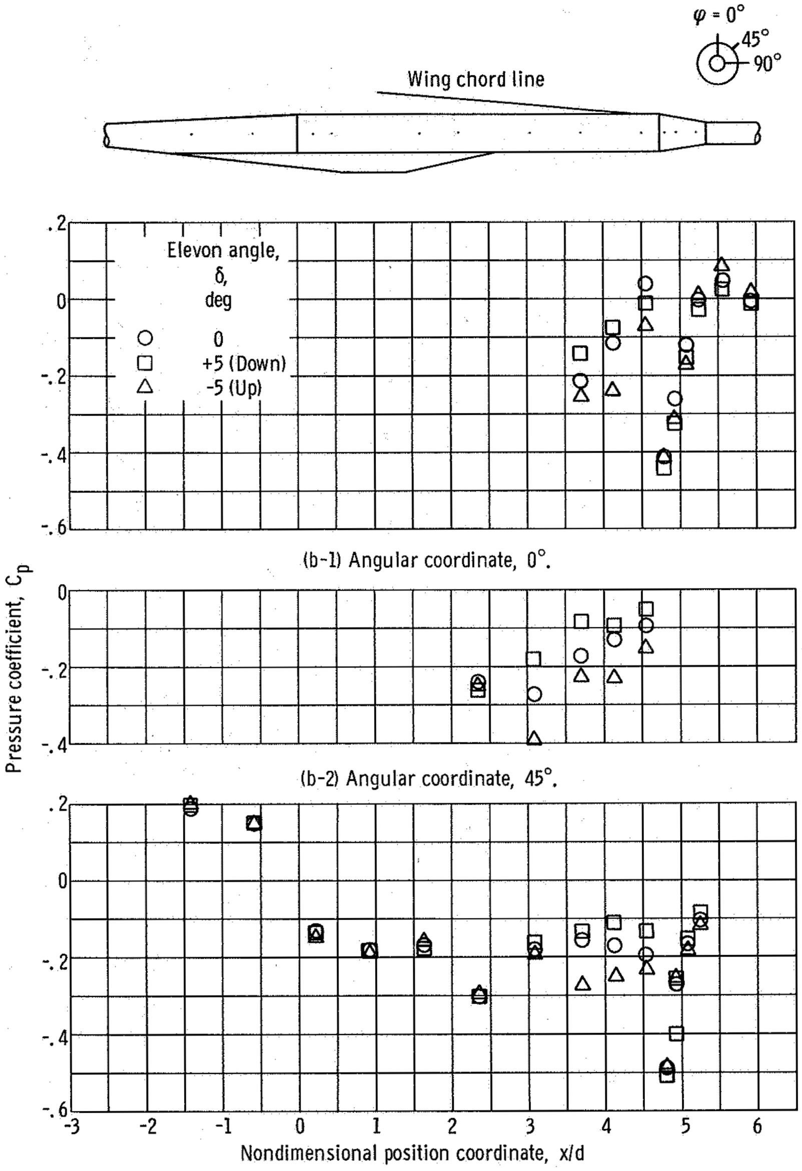

(b-1) Angular coordinate, 0°.

(b-2) Angular coordinate, 45°.

Nondimensional position coordinate, x/d

(b-3) Angular coordinate, 90°.

(b) Free-stream Mach number, 1.2.

Figure 27. - Continued.

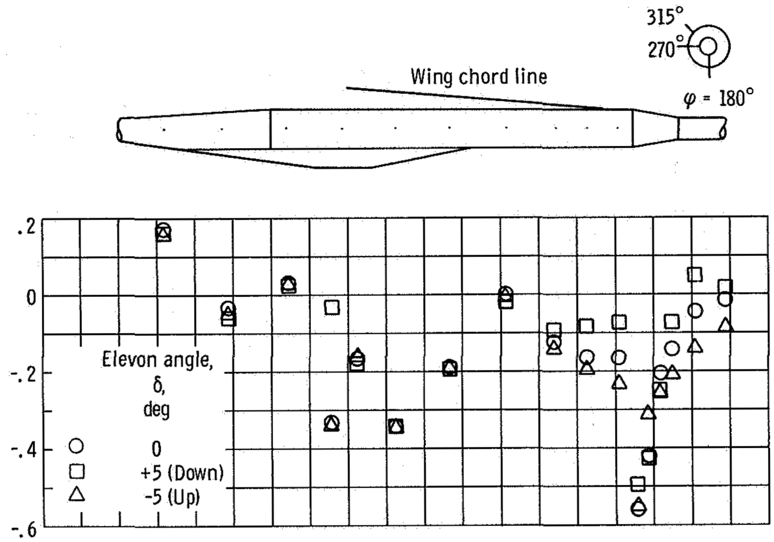

(b-4) Angular coordinate, 180°.

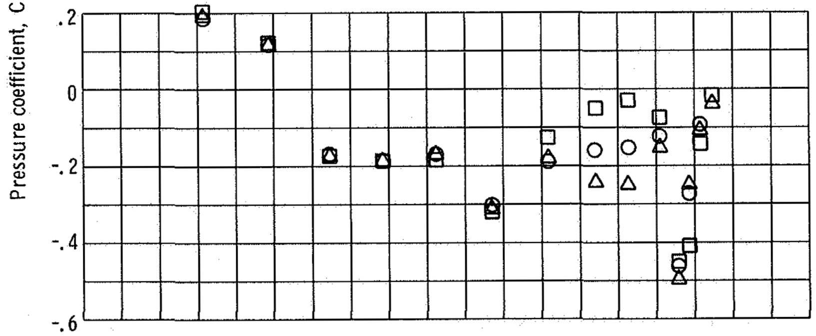

(b-5) Angular coordinate, 270°.

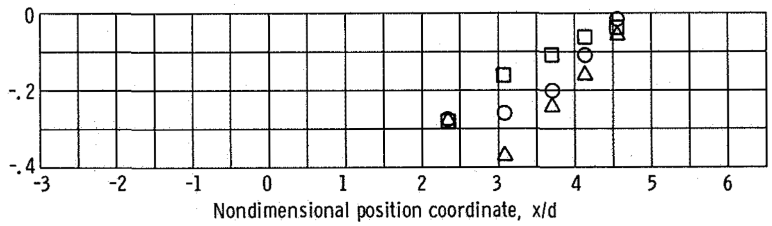

(b-6) Angular coordinate, 315°.

(b) Concluded.

Figure 27. - Concluded.

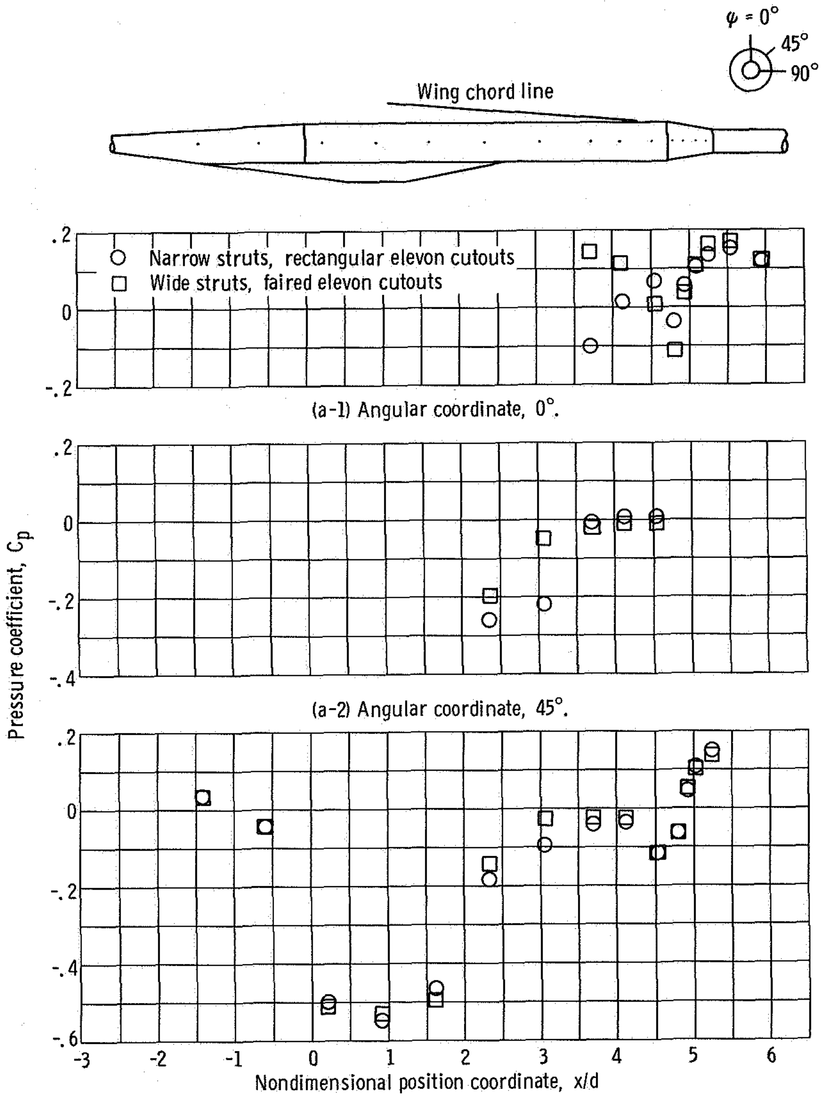

(a-1) Angular coordinate, 0°.

(a-2) Angular coordinate, 45°.

(a-3) Angular coordinate, 90°.

(a) Free-stream Mach number, 0.9.

Figure 28. - Effect of nacelle strut and elevon cutout geometry on nacelle pressure distribution; solid bulged nacelles at 0° angle of attack and 0° elevon angle.

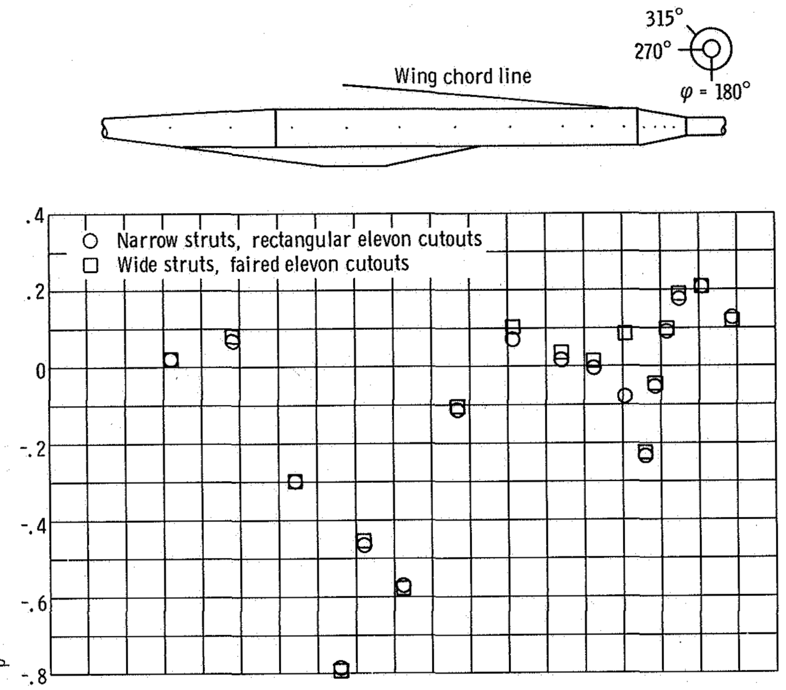

(a-4) Angular coordinate, 180°.

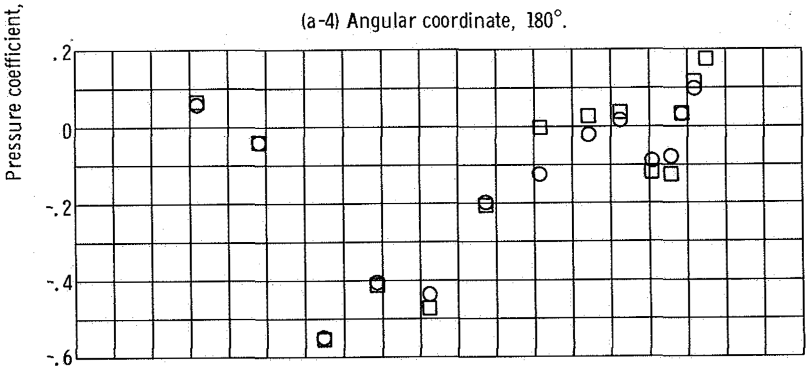

(a-5) Angular coordinate 270°.

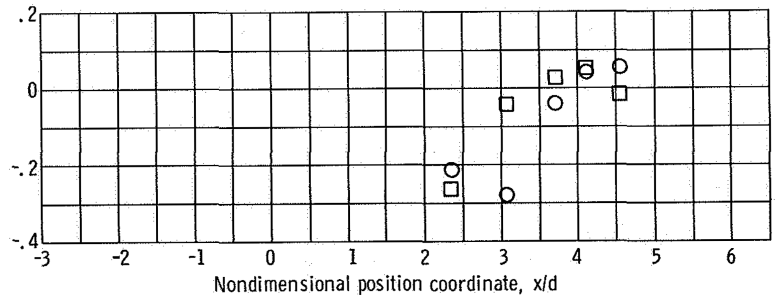

(a-6) Angular coordinate, 315°.

(a) Concluded.

Figure 28. - Continued.

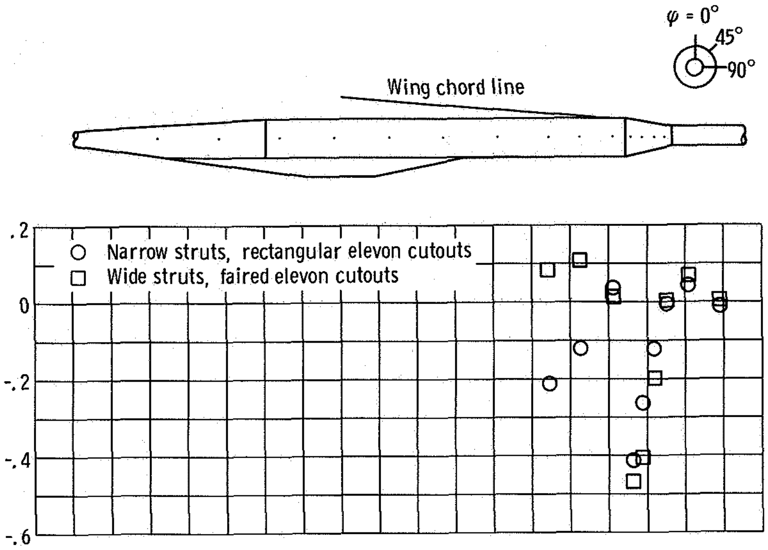

(b-1) Angular coordinate, 0°.

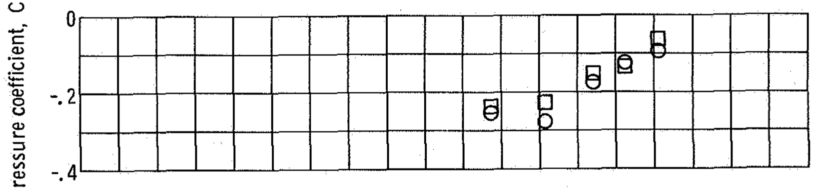

(b-2) Angular coordinate, 45°.

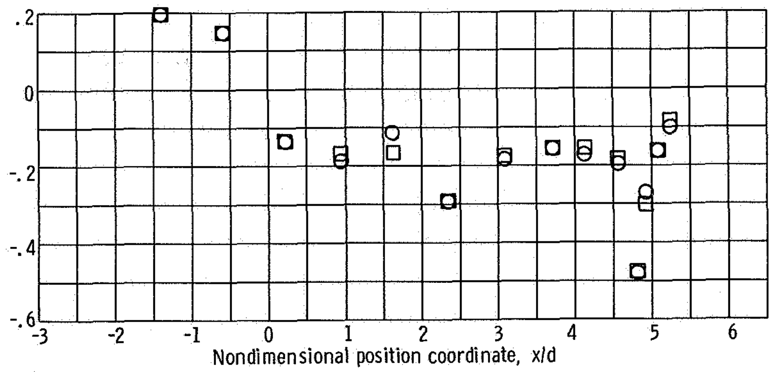

(b-3) Angular coordinate, 90°.

(b) Free-stream Mach number, 1.2.

Figure 28. - Continued.

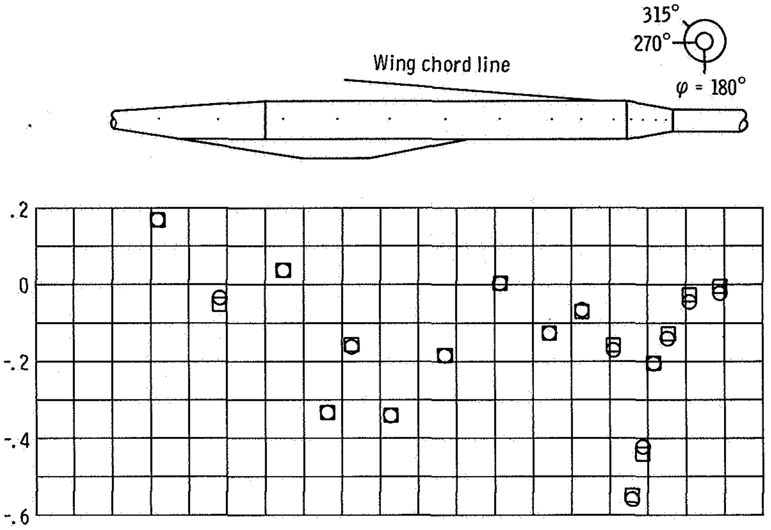

(b-4) Angular coordinate, 180°.

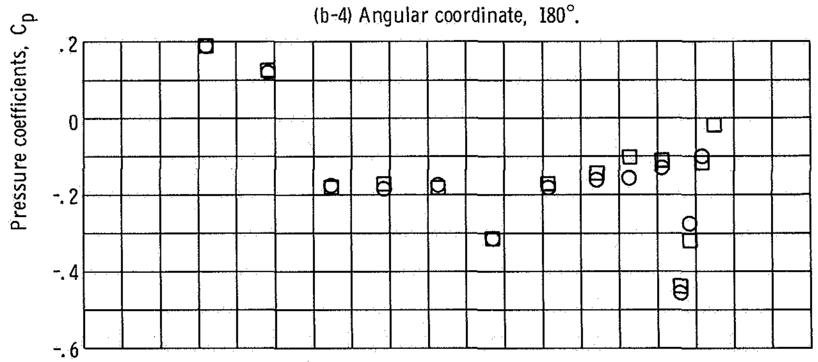

(b-5) Angular coordinate, 270°.

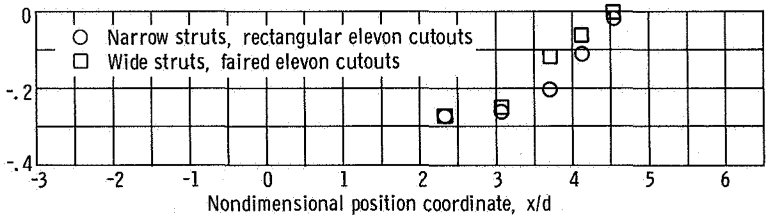

(b-6) Angular coordinate, 315°.

(b) Concluded.

Figure 28. - Concluded.

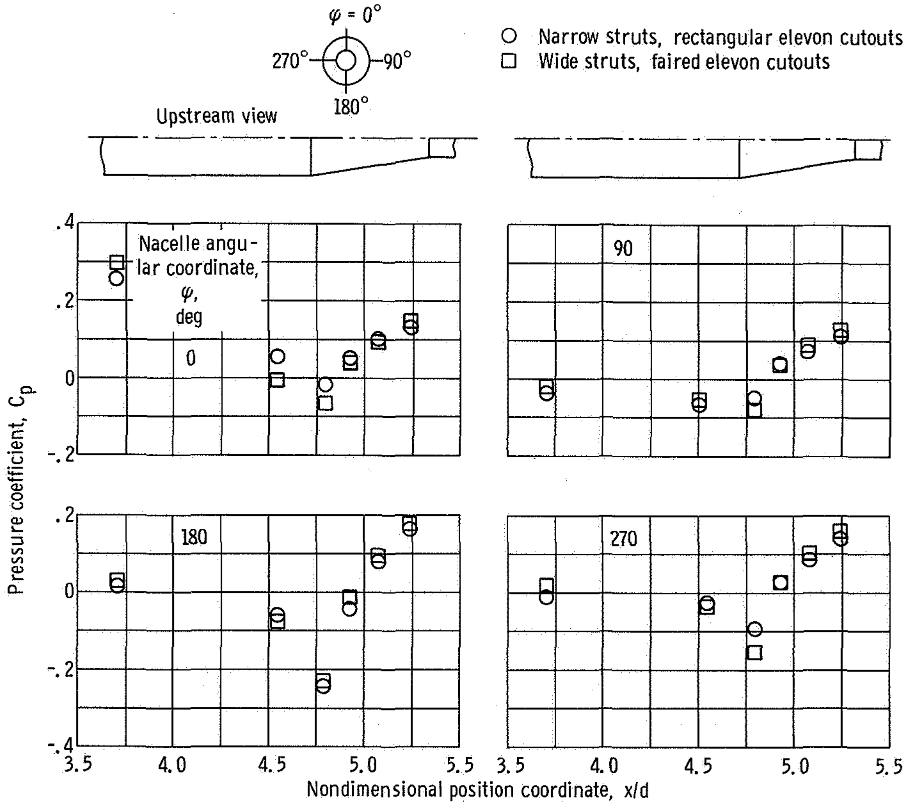

(a) Free-stream Mach number, 0.9.

Figure 29. - Effect of nacelle strut and elevon cutout geometry on nacelle pressures; open bulged nacelles at 0° angle of attack and 0° elevon angle.

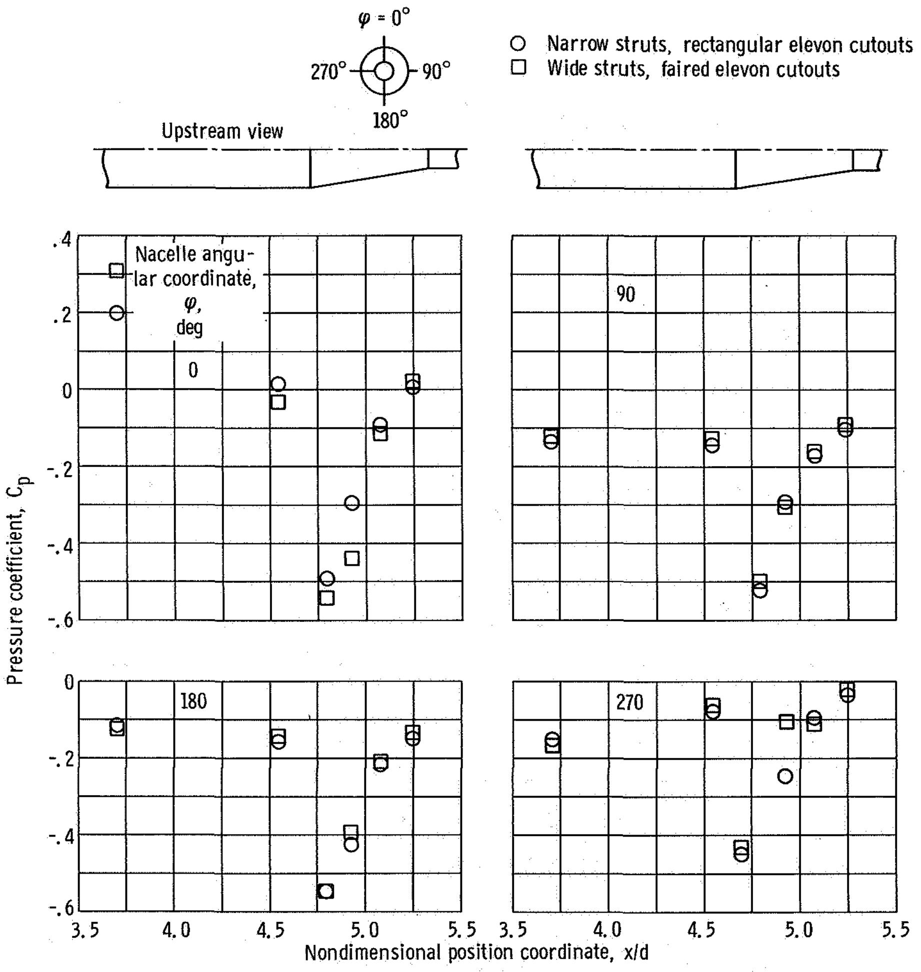

(b) Free-stream Mach number, 1.2.

Figure 29. - Concluded.

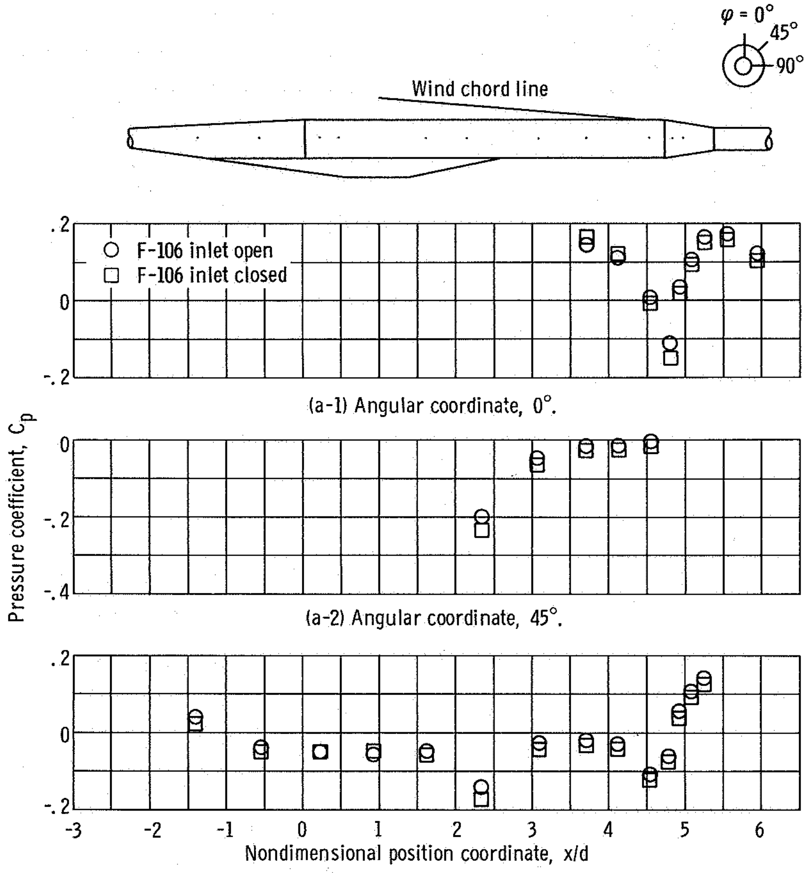

(a-1) Angular coordinate, 0°.

(a-2) Angular coordinate, 45°.

(a-3) Angular coordinate, 90°.

(a) Free-stream Mach number, 0.9.

Figure 30. - Effect of closed F-106 inlets on nacelle pressure distribution; solid bulged nacelles with wide struts and faired elevon cutouts at 0° angle of attack and 0° elevon angle.

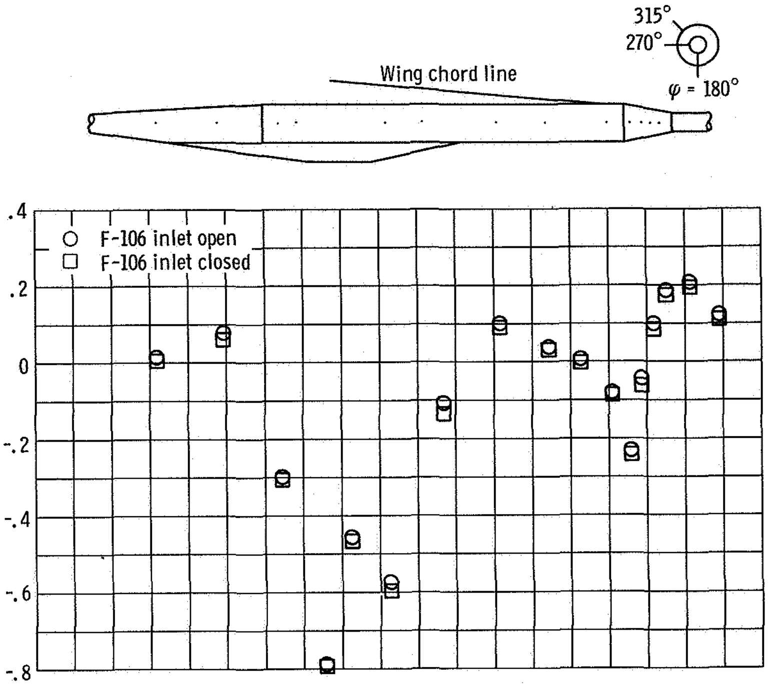

(a-4) Angular coordinate, 180°.

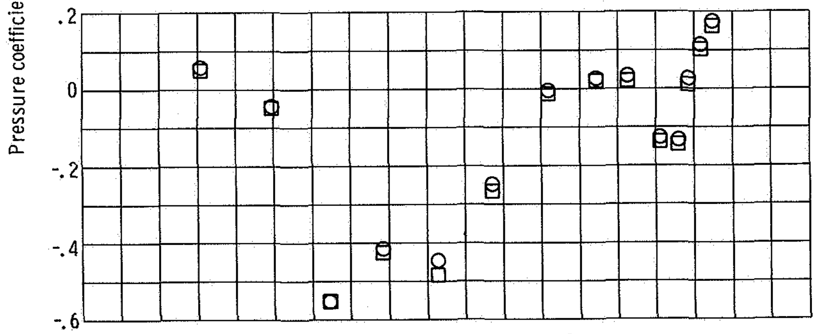

(a-5) Angular coordinate, 270°.

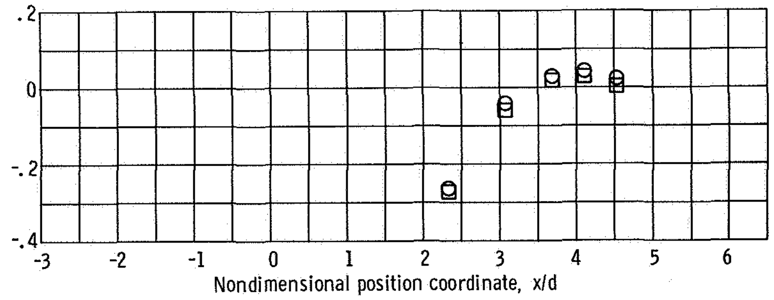

(a-6) Angular coordinate, 315°.

(a) Concluded.

Figure 30. - Continued.

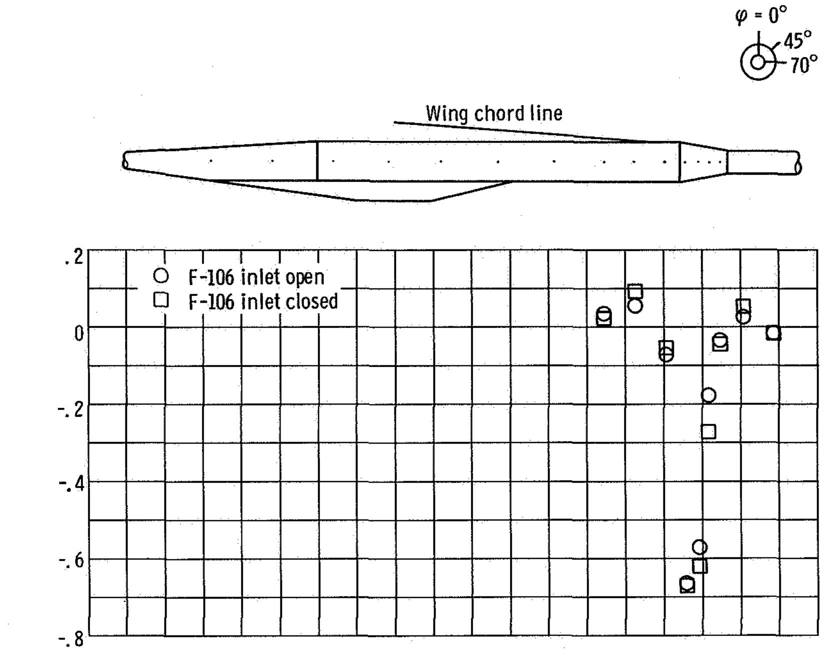

(b-1) Angular coordinate, 0°.

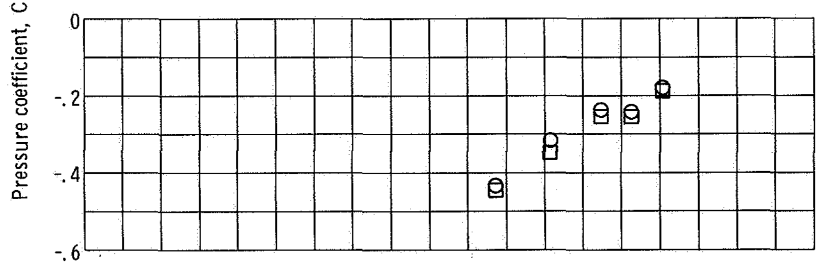

(b-2) Angular coordinate, 45°.

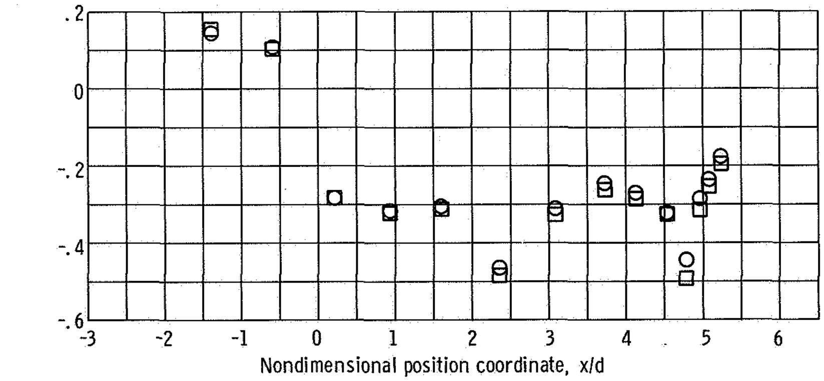

(b-3) Angular coordinate, 90°.

(b) Free-stream Mach number, 1.05.

Figure 30. - Continued.

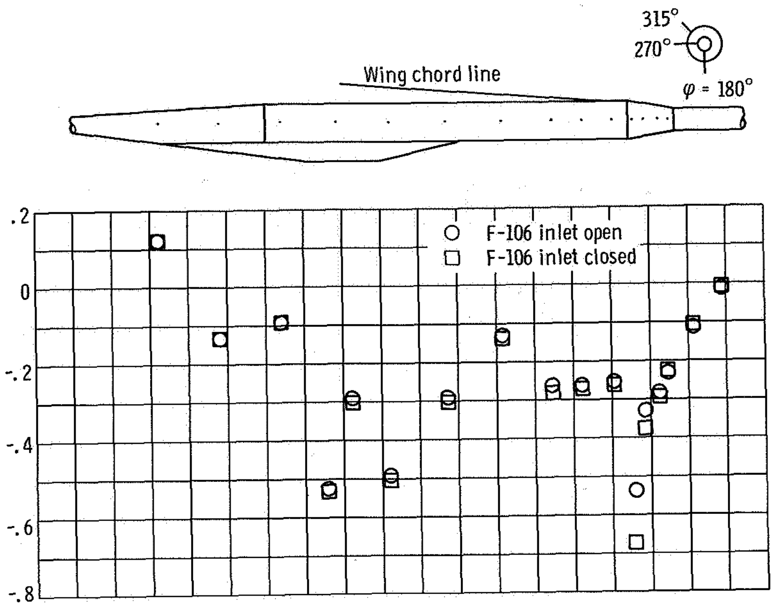

(b-4) Angular coordinate, 180°.

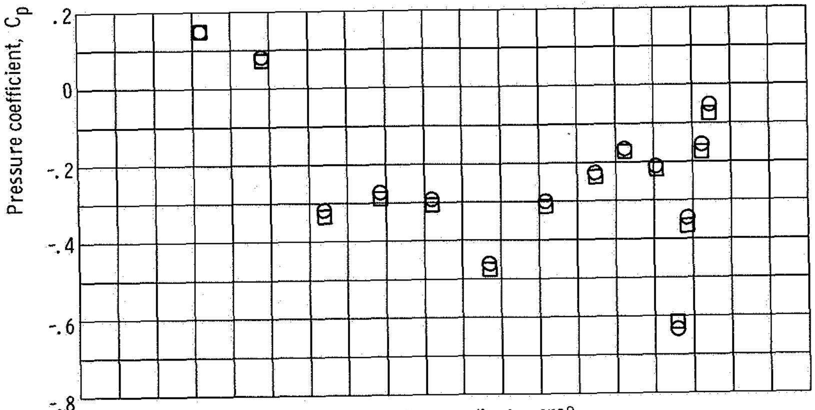

(b-5) Angular coordinate, 270°.

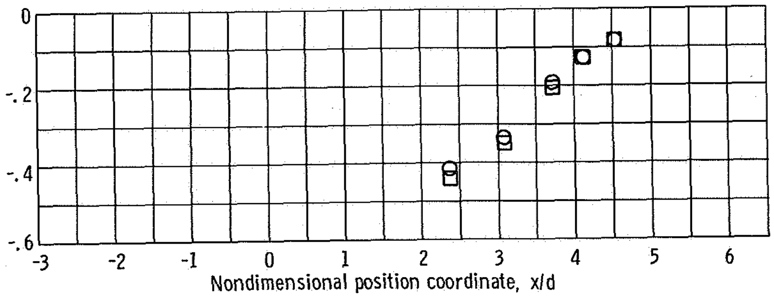

(b-6) Angular coordinate, 315°.

(b) Concluded.

Figure 30. - Concluded.

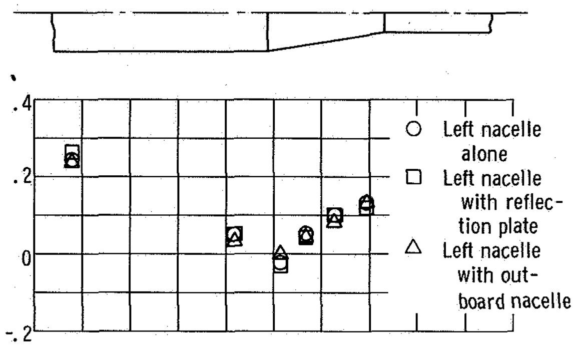

(a-1) Angular coordinate, 0°.

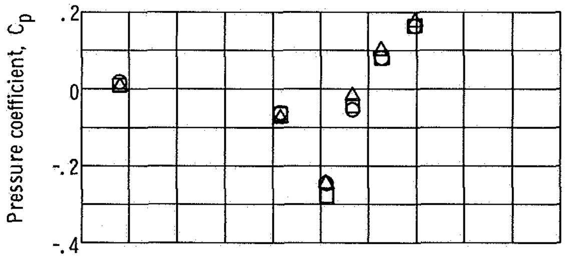

(a-2) Angular coordinate, 180°.

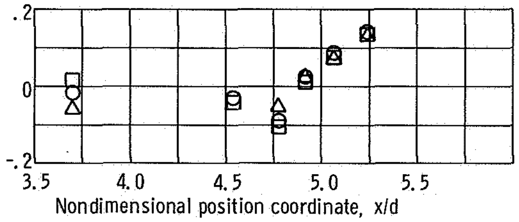

(a-3) Angular coordinate, 270°.

(a) Free-stream Mach number, 0.9.

Figure 31. - Effect of reflection plate and outboard nacelle on inboard nacelle pressures; open bulged nacelles with narrow struts and rectangular elevon cutouts at 0° angle of attack and 0° elevon angle.

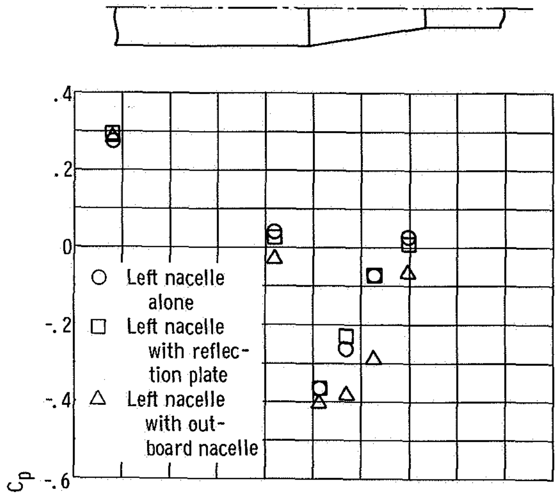

(b-1) Angular coordinate, 0°.

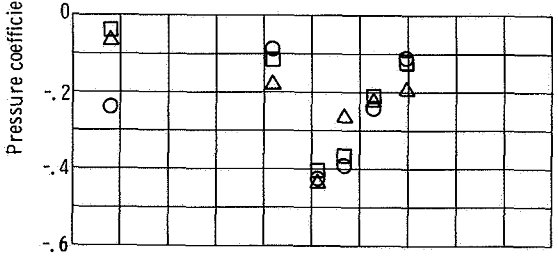

(b-2) Angular coordinate, 180°.

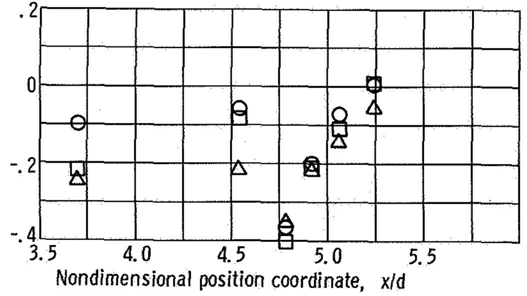

(b-3) Angular coordinate, 270°.

(b) Free-stream Mach number, 1.36.

Figure 31. - Concluded.

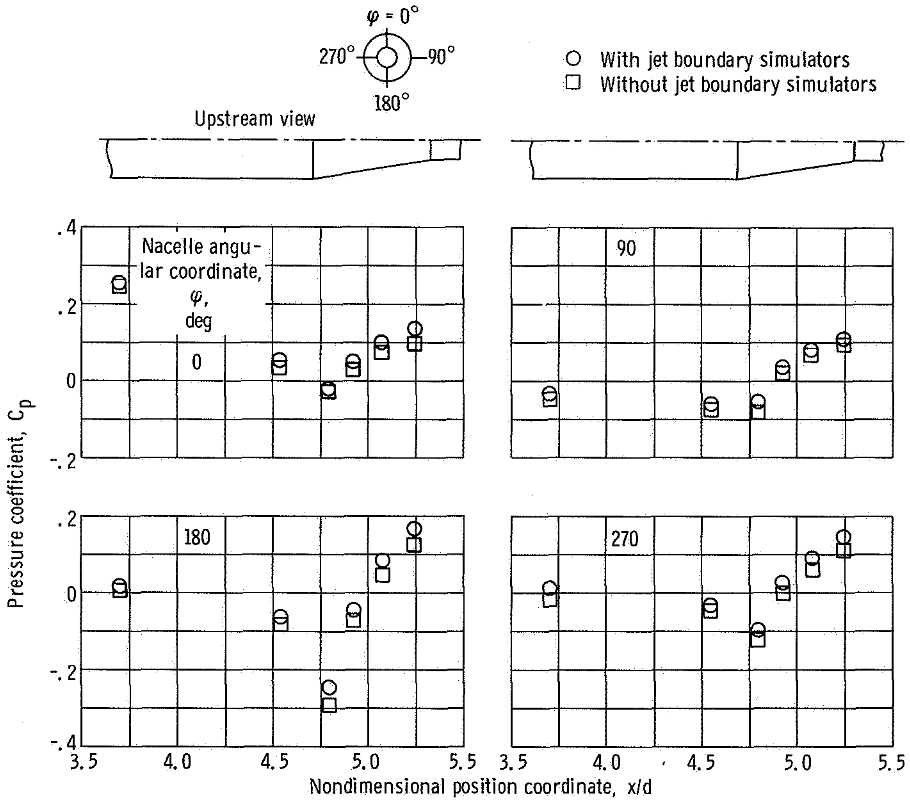

(a) Free-stream Mach number, 0.9.

Figure 32. - Comparison of open-nose bulged-nacelle pressures with and without jet boundary simulators; narrow struts and rectangular elevon cutouts at 0° angle of attack and 0° elevon angle.

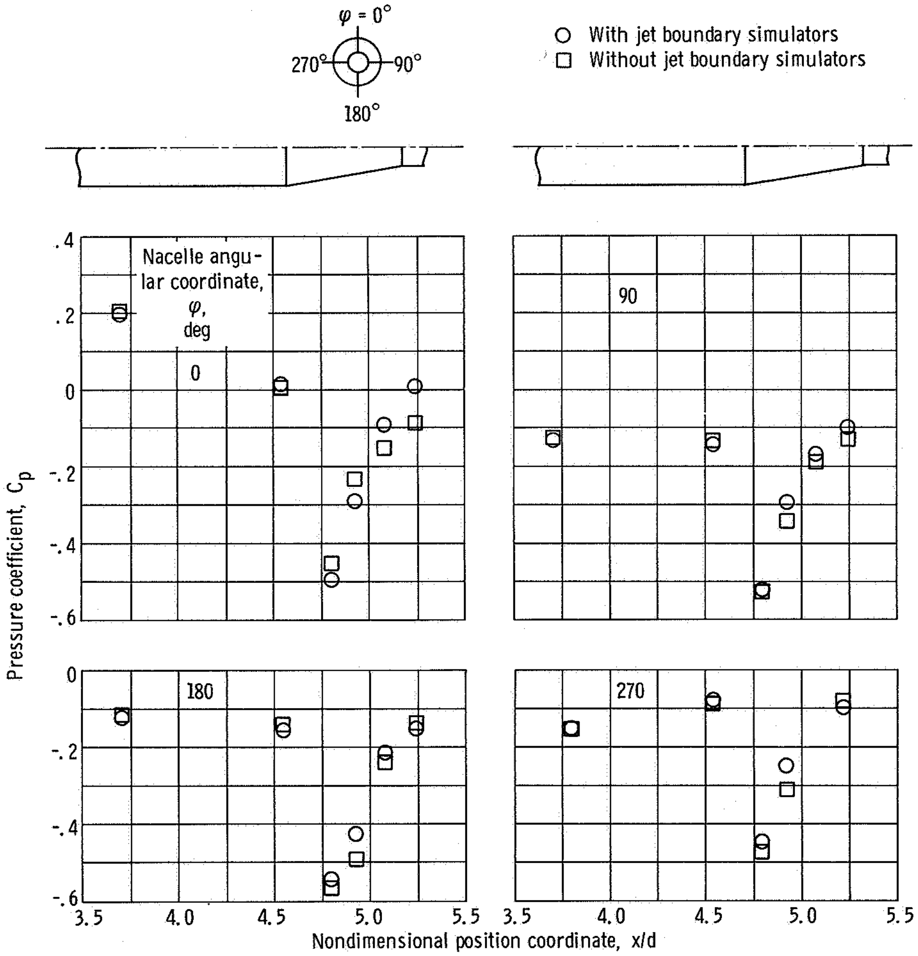

(b) Free-stream Mach number, 1.2.

Figure 32. - Concluded.

NASA-Langley, 1968 —— 10 E-4555

> *"The aeronautical and space activities of the United States shall be conducted so as to contribute . . . to the expansion of human knowledge of phenomena in the atmosphere and space. The Administration shall provide for the widest practicable and appropriate dissemination of information concerning its activities and the results thereof."*
>
> —NATIONAL AERONAUTICS AND SPACE ACT OF 1958

NASA SCIENTIFIC AND TECHNICAL PUBLICATIONS

TECHNICAL REPORTS: Scientific and technical information considered important, complete, and a lasting contribution to existing knowledge.

TECHNICAL NOTES: Information less broad in scope but nevertheless of importance as a contribution to existing knowledge.

TECHNICAL MEMORANDUMS: Information receiving limited distribution because of preliminary data, security classification, or other reasons.

CONTRACTOR REPORTS: Scientific and technical information generated under a NASA contract or grant and considered an important contribution to existing knowledge.

TECHNICAL TRANSLATIONS: Information published in a foreign language considered to merit NASA distribution in English.

SPECIAL PUBLICATIONS: Information derived from or of value to NASA activities. Publications include conference proceedings, monographs, data compilations, handbooks, sourcebooks, and special bibliographies.

TECHNOLOGY UTILIZATION PUBLICATIONS: Information on technology used by NASA that may be of particular interest in commercial and other non-aerospace applications. Publications include Tech Briefs, Technology Utilization Reports and Notes, and Technology Surveys.

Details on the availability of these publications may be obtained from:

SCIENTIFIC AND TECHNICAL INFORMATION DIVISION
NATIONAL AERONAUTICS AND SPACE ADMINISTRATION
Washington, D.C. 20546